

October 2013

# Radar Receiver Calibration Toolkit

Ryan Orlando Cantalupo  
*Worcester Polytechnic Institute*

Samuel Fritz Petersen  
*Worcester Polytechnic Institute*

Follow this and additional works at: <https://digitalcommons.wpi.edu/mqp-all>

---

## Repository Citation

Cantalupo, R. O., & Petersen, S. F. (2013). *Radar Receiver Calibration Toolkit*. Retrieved from <https://digitalcommons.wpi.edu/mqp-all/3662>

This Unrestricted is brought to you for free and open access by the Major Qualifying Projects at Digital WPI. It has been accepted for inclusion in Major Qualifying Projects (All Years) by an authorized administrator of Digital WPI. For more information, please contact [digitalwpi@wpi.edu](mailto:digitalwpi@wpi.edu).



# Radar Receiver Calibration Toolkit

GUI Application for Computing Radar Health Metrics

MIT Lincoln Laboratory, Group 108

Major Qualifying Project

Submitted by:

Samuel Petersen  
Ryan Cantalupo

Submitted to:

Project Advisors:

Professor Edward A. Clancy

Project Supervisors:

Lisa Basile, MIT Lincoln Laboratory  
Sarah Curry, MIT Lincoln Laboratory  
William Cantrell, MIT Lincoln Laboratory  
Joe Theriault, MIT Lincoln Laboratory

October 25, 2013

This work is sponsored by the Department of the Air Force under Air Force Contract #FA8721-10-C-0007. Opinions, interpretations, conclusions, and recommendations are those of the authors and not necessarily endorsed by the United States Government.

DISTRIBUTION STATEMENT A: Approved for public release. Distribution is unlimited.

## **Abstract**

This project provides motivation and a solution for improved radar receiver gain calibration practices for MIT Lincoln Laboratory Group 108 (Tactical Defense Systems). Currently, radar operators manually calculate a receiver's gain from measurements taken on a signal analyzer while injecting known sinusoidal signals into the receiver. The results of this process are not assessed until after the test mission is over. Given the time and expense of flight tests, it is beneficial to both Group 108 and their United States Air Force sponsors to streamline and standardize the calibration process, ensuring accuracy of data during field missions. Our work supports this effort by simulating gain variation of a radar receiver as a function of frequency and temperature, and developing a graphical user interface (GUI) application for automated computation and display of receiver gain calibration results.

The simulation, based on the specifications of a real S-band radar receiver that was available to us, showed an average gain reduction of 0.56 dB (12.1%) for increasing frequency over the passband. An average in-band gain decrease of 5.26 dB (70.21%) was predicted across the temperature range -40 °C to +85 °C. Our model was accurate to within 1 dB of test measurements made on our receiver. The significant gain variation in the simulation demonstrates the importance of receiver calibration and motivates the need for improving it.

The receiver calibration toolkit, the main deliverable of the project, allows the operator to quickly calibrate a receiver without additional instrumentation such as a signal analyzer. The tool calculates output signal power based on digital recordings, acquired using the same recording method as mission data, and immediately displays the results of the calibration. We verified the calibration toolkit's performance by comparing the results from calibrating our test receiver using the toolkit and using the manual method. The toolkit's power level calculations are accurate within 0.2 dB, resulting in an accurate calculation of nominal gain. The radar receiver calibration toolkit meets the needs of Group 108 and will be used in future flight tests.

## **Statement of Authorship**

This project has been completed in partial fulfillment of the requirements for the degree of Bachelors of Science in the field of Electrical and Computer Engineering.

### **Samuel Petersen**

Primary Author: Abstract, Executive Summary, Introduction, Background, Radar Receiver Calibration Tool, Discussion, Conclusion

Testing: Hardware Test Measurements, Calibration Tool Performance Data, Time Test, LO Power Test, MATLAB Implementation Performance

Assembled S-Band hardware test receiver

Designed and developed receiver gain calibration software GUI application in C++ using Qt API

Developed MATLAB bandpass filtering algorithm for detecting signals below the receiver noise

### **Ryan Cantalupo**

Primary Author: Abstract, Introduction, Background, Radar Receiver Simulation, Discussion

Testing: Custom RF bandpass filter gain measurements for varying frequency and temperature, Hardware Test Measurements

Developed hardware receiver model and ran simulations in MATLAB and Simulink

## **Acknowledgements**

We would like to thank our Lincoln Laboratory mentors Lisa Basile, William Cantrell, Sarah Curry, and Joseph Theriault, as well as our WPI advisor Professor Edward Clancy, for their support throughout the project. Their guidance was instrumental in the success of this project.

## Executive Summary

Radars are a critical component in defense systems, producing data that can be processed for information such as target speed, range and radar cross section which are vital in determining potential threats. In particular, the radar cross section of a target can provide information regarding the target's identity and establishes the maximum range at which a target is detectable; therefore it is of great interest in studying air vehicle survivability and vulnerability to weapons systems. The target's radar cross section (denoted as  $\sigma$ ) can be determined using the radar range equation if all the other variables are known.

$$P_r = P_t \frac{G_t G_r \sigma \lambda^2}{(4\pi)^3 R^4}$$

$P_t$  = Power to transmit antenna  
 $P_r$  = Power from receive antenna  
 $G_t$  = Transmit antenna gain  
 $G_r$  = Receive antenna gain  
 $\lambda$  = Wavelength  
 $\sigma$  = Radar cross section (RCS)  
 $R$  = Range

A key variable to determine in this equation is received power. Since the received signal is amplified by a receiver before it is measured, the receiver gain must be known to a high degree of accuracy to determine received power. Receiver gain is the ratio of receiver output power to receiver input power, and the process of precisely determining this value is called receiver gain calibration.

This project analyzes the issue of radar receiver gain calibration and addresses the need for an intuitive, versatile calibration toolkit by creating a graphical user interface (GUI) application. The application can be used by Lincoln Laboratory radar operators in the field or by analysts working with mission data after the fact. The automated tool streamlines the process of calibration and provides other useful radar health indications.

Due to the imperfections of the electrical components that comprise a radar receiver, the overall gain can vary for changing operating conditions such as temperature and received signal frequency. The first goal of the project was to create a model of a radar receiver in Simulink to simulate gain variation as a function of temperature and frequency. The model implemented

the characteristics of the components of a real S-band radar receiver that was available for testing. For temperature data, the model utilizes values provided by the vendors of the physical hardware components. The datasheets listed gain values at specific frequencies for operation at -40 °C, +25 °C, and +85 °C.

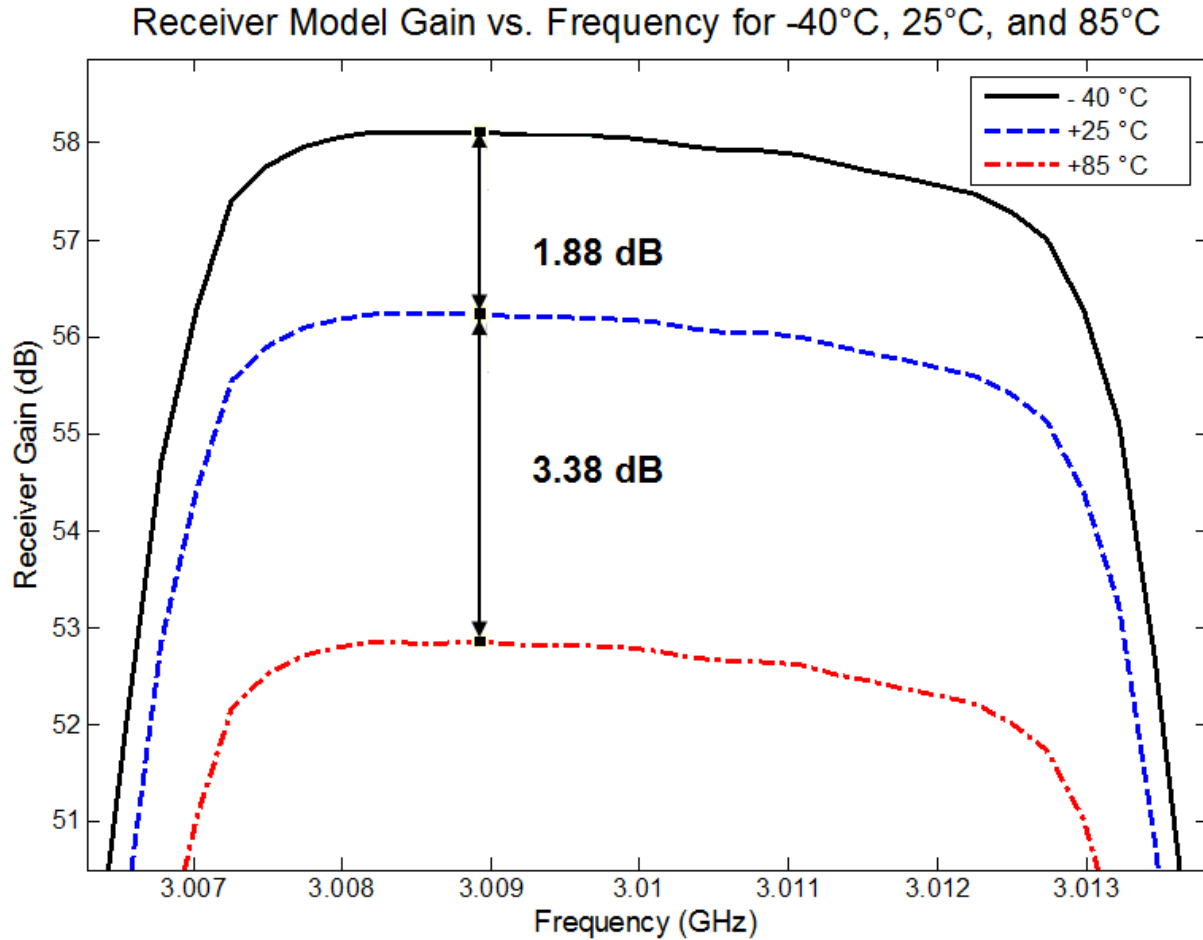


Figure 1: Plot of simulated receiver gain performance over the tunable bandwidth at -40 °C, +25 °C, and +85 °C operating temperatures.

The simulation results displayed in Figure 1 show that temperature differences have a significant impact on gain; the gain varies by 5.26 dB over the range of operational temperatures listed in the receiver components' specifications. This difference is equivalent to a 70.21% decrease in signal gain. A general decrease of approximately 0.56 dB (a 12.1% decrease) occurs for increasing frequency from 3.008214 GHz to 3.012024 GHz at a given

temperature. At the edges of the passband, approximately 3.007 GHz and 3.013 GHz, gain decreases between 1.65 to 1.78 dB (32.62% decrease on average) from the average gain within 3.008214 GHz to 3.012024 GHz. In addition to the model, we tested the gain variation of the physical S-band receiver with the low noise amplifier (LNA) operating at three different temperatures: 0 °C, +25 °C, and +50 °C. In these tests, the receiver gain varied 0.91 dB by over the LNA temperature range from 0 to +50 °C. Further testing showed that the gain also varies by +/- 0.3 dB depending on how long the receiver has been powered on, due to internal heating. Simulation and testing verifies the fact that receiver gain is lowered significantly by increased operating temperature. Since Group 108 fields radars in different climates ranging from below 0 °C to above +50 °C, this gain variation needs to be accounted for through calibration.

With this information, it is clear that frequent calibration of a receiver in the field is a prudent practice to ensure accurate mission data. The receiver calibration process involves bypassing the antenna by injecting known test signals directly into the RF input of the receiver, and measuring the receiver output power. The gain is the ratio of the output power to input power, usually expressed in decibels (dB). Multiple gain measurements are made at various input power levels, often stepped in increments of 5 or 10 dB from below the noise floor up to the compression region of the receiver, enabling the entire dynamic range of the receiver to be analyzed. In a manual calibration scenario, power measurements are acquired using a spectrum analyzer or other instrumentation. The input and output power levels are manually written in a log by the radar operator, and the calibration factor—the gain of the receiver in the linear region—is computed after the mission. The time-consuming and tedious nature of the manual calibration process can be mitigated by an automated tool.

The calibration toolkit developed in this project expedites and simplifies the calibration process. The operator still steps the input power through the dynamic range of the receiver, but instead of using a spectrum analyzer to make power measurements at each power, each signal is briefly recorded using the real-time server with a high-speed analog-to-digital converter. Radar mission data is recorded in the same way, so there is no additional setup



needed. The file format for the recordings is Radar Open System Architecture II (ROSA II), a Lincoln Laboratory standard for radar recordings. Operating with a standardized file format enables the tool to be useable for many different radar systems. With a set of recordings corresponding to the range of input power levels in the calibration, the operator or analyst can run the calibration toolkit application, enter the necessary parameters, and view the calibration results in seconds.

The radar receiver calibration toolkit is a graphical user interface (GUI) application written in C++ using the Qt GUI framework. The two main screens are shown below in Figure 2.

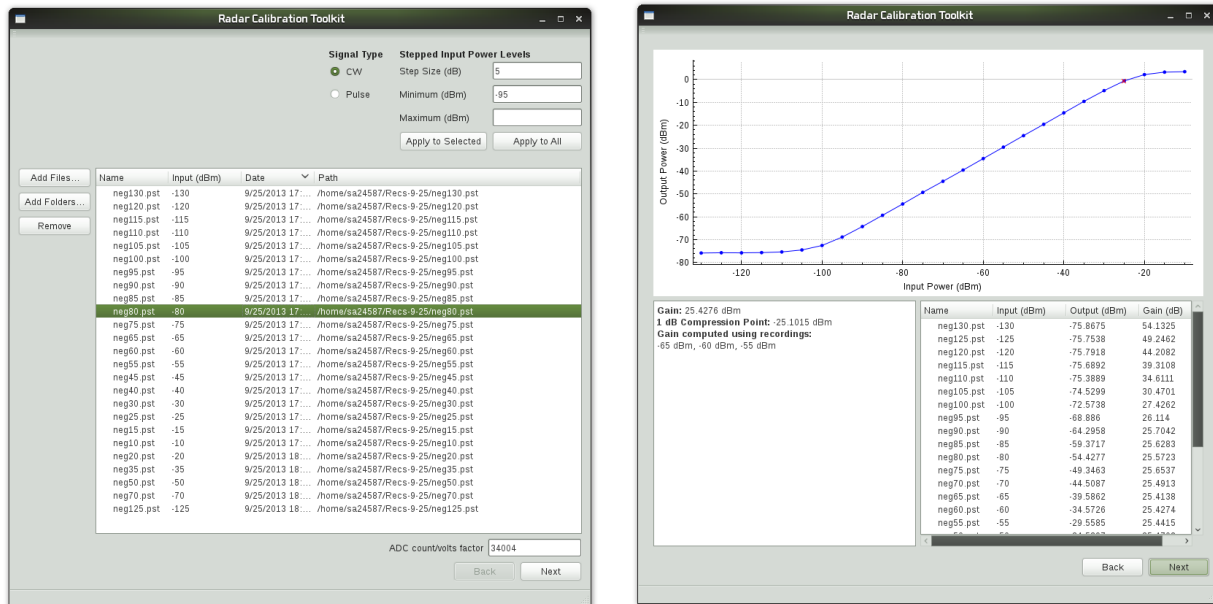
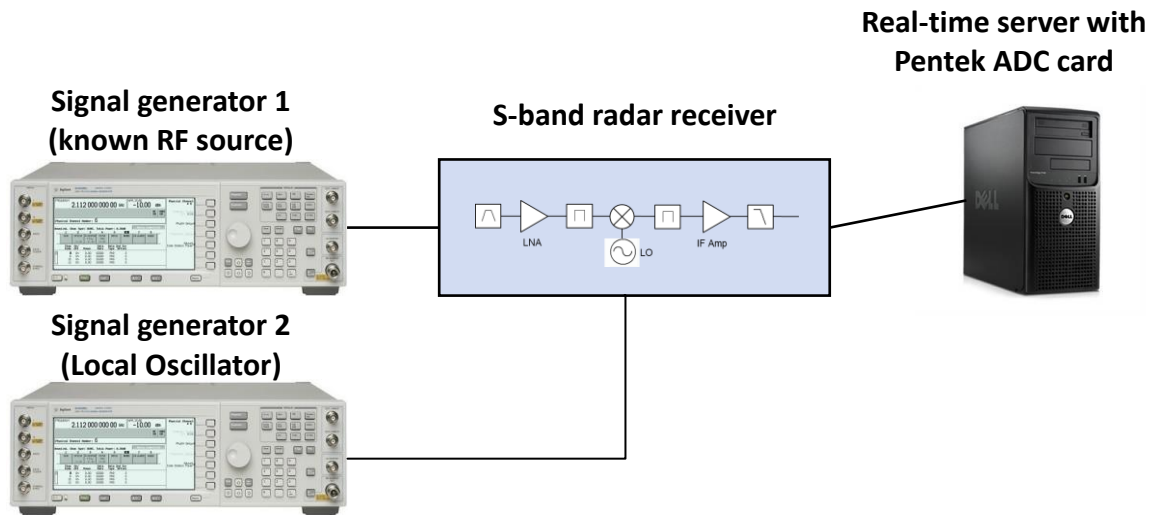


Figure 2: Screenshots of calibration toolkit. User input screen (left) and calibration results screen (right).

The first screen prompts the user to load the ROSA II recording files, enter the input power level associated with each file, and the counts per volt factor of the analog-to-digital converter. The tool then parses the files, computes the power levels of each signal, and computes the calibration factor and other measures. On the second screen, the application displays the results to the user intuitively, showing a plot of the output power versus input power of the receiver, a typical way that analysts visualize receiver performance. The calibration factor is also

computed and displayed to the user, along with the 1 dB compression point, defined as the input power level of the receiver that corresponds to a gain value 1 dB below the nominal gain (or calibration factor). The calibration results are also saved to a text file for later use. The application is fully integrated into a larger radar analysis program developed at Lincoln Laboratory called Post Mission Analysis.



*Figure 3: Test setup for performing calibration of S-band receiver.*

By testing the calibration tool with the hardware setup shown in Figure 3, the calibration results were found to be consistent with manual calibration. The output power calculations are quite accurate, with an error margin of 0.2 dB for the recordings made above the noise level, compared with manual measurements using a spectrum analyzer. For lower input power levels, the noise level in the output signal obscures the desired signal, so the computed power level is essentially the noise power. Signal processing such as bandpass filtering is necessary to remove the noise from the desired signal. Future work on the calibration tool could include detecting the test signal frequency, and applying a bandpass filter to remove noise before the power calculations are made. This procedure was demonstrated in MATLAB, since time did not permit implementing the algorithm in C++.

The calibration toolkit developed in this project has the potential to improve flight test practices for Group 108 at MIT Lincoln Laboratory. Making calibration simpler and less error-

prone can improve the accuracy of mission data and ensure that the receiver is functioning as expected, preventing waste of costly test time.

## Table of Contents

Abstract.....	2
Statement of Authorship .....	3
Acknowledgements.....	4
Executive Summary.....	5
Table of Contents .....	11
Table of Figures.....	14
Table of Tables .....	18
Chapter 1: Introduction .....	20
Chapter 2: Background .....	22
2.1 Radar Range Equation.....	22
2.2 Radar Cross Section .....	23
2.3 Radar Receiver Design .....	25
2.3.1 Simplified Single-Conversion Superheterodyne Receiver .....	25
2.3.2 Gain Dependency.....	29
2.4 Radar Receiver Gain Calibration .....	30
2.4.1 Receiver Dynamic Range, Noise Floor, and 1dB Compression Point .....	30
2.4.2 Receiver Gain Calibration Process .....	32
2.5 Analog-to-Digital Converters .....	34
2.5.1 ADC Error .....	34
2.5.2 I/Q Data.....	36
2.6 Radar Systems at Lincoln Laboratory.....	37
2.6.1 Radar Open System Architecture .....	37

2.6.2 Post-Mission Analysis.....	38
Chapter 3: Radar Receiver Simulation .....	40
3.1 Introduction: Motivating the Gain Calibration Toolkit .....	40
3.2 Methods of Simulation Model and Hardware Test Measurements.....	40
3.2.1 Model Basis .....	40
3.2.2 Model Functionality .....	42
3.3 Hardware Test Measurements .....	44
3.4 Model Implementation in Matlab and Simulink.....	45
3.5 Simulation and Hardware Test Results .....	47
3.5.1 Model Results .....	48
3.5.2 Simulation Model and Hardware Test Comparison.....	52
Chapter 4: Radar Receiver Calibration Tool.....	55
4.1 Methods .....	55
4.1.1 Program Function and User Interface .....	55
4.1.2 Algorithms.....	58
4.1.3 Development Process .....	65
4.1.4 Testing.....	67
4.2 Results.....	71
4.2.1 Calibration Tool Performance.....	74
4.2.2 Calibration Tool Use Demonstrations.....	84
4.2.3 Receiver Noise Floor Determination.....	87
Chapter 5: Discussion.....	92
5.1 Limitations.....	93
5.1.1 Model Simulation and Hardware Test Measurements.....	93

5.1.2 Calibration Tool .....	94
5.1.3 Future Work .....	95
Chapter 6: Conclusions .....	97
References .....	98
Appendix A: Simulation Datasheet Sources and Estimated Values.....	100
RF Bandpass Filter FL1 .....	100
LNA A1.....	102
RF Amp A2.....	103
RF Bandpass Filter FL2 .....	105
RF Amp A3.....	108
Attenuators ATT1, ATT2, ATT3, ATT4, and ATT5 .....	109
Mixer MX1 and LO .....	111
IF Bandpass Filter FL3.....	112
IF Amps A4 and A5 .....	115
IF Lowpass Filter FL4 .....	116
Appendix B: Hardware Test Measurements .....	119
Appendix C: Calibration Tool Performance Data .....	120
Appendix D: Time Test .....	123
Appendix E: LO Power Test.....	124
Appendix F: MATLAB Implementation Performance .....	125

## Table of Figures

Figure 1: Simulated receiver gain over the tunable bandwidth at -40 °C, +25 °C, and +85 °C .....	6
Figure 2: Screenshots of calibration toolkit user input and calibration results screens . .....	8
Figure 3: Test setup for performing calibration of S-band receiver .....	9
Figure 4: Examples of radar cross section measurements .....	24
Figure 5: Simplified single-conversion superheterodyne receiver chain example. ....	26
Figure 6: Frequency selectivity of RF bandpass filter. ....	27
Figure 7: The image frequency interference mixes directly to IF. ....	28
Figure 8: Example gain plot showing noise floor, linear, and saturation regions .....	31
Figure 9: Expanded view of the onset of receiver compression.. ....	32
Figure 10: Ideal ADC behavior .....	34
Figure 11: Behavior of an ADC exhibiting gain error and offset error.....	35
Figure 12: Plot showing I/Q vector and circular path of I/Q data points in a sinusoid .....	36
Figure 13: Difference between a customized radar system and ROSA radar system .....	37
Figure 14: Screenshot of the main window of Post-Mission Analysis Toolkit.....	39
Figure 15: Simplified circuit schematic of hardware test receiver. ....	41
Figure 16: Example of linear gain interpolation over frequency and temperature.. ....	43
Figure 17: Simulink receiver model simulated at +25 °C.....	47
Figure 18: Receiver model gain over 45 MHz span at -40 °C, +25 °C, and +85 °C. ....	49
Figure 19: Closer view of receiver model in-band gain at -40 °C, +25 °C, and +85 °C.....	50

Figure 20: Receiver model gain vs. temperature.....	51
Figure 21: Gain vs. LNA temperature for model and hardware at constant frequency.....	52
Figure 22: Model and hardware in-band gain for LNA temperatures +25 °C and +50 °C. ....	53
Figure 23: High-level functionality of radar calibration toolkit .....	56
Figure 24: Design of main user input screen .....	57
Figure 25: Design of calibration output screen .....	58
Figure 26: Flowchart of algorithm for parsing recording files and obtaining output power levels .....	59
Figure 27: Flowchart of algorithm for calculating overall receiver gain with example values for demonstration. ....	62
Figure 28: Plots of example data from Figure 27 .....	63
Figure 29: Plot showing interpolation of 1 dB compression point as described in Equation 9 ...	65
Figure 30: Screenshot of Qt Creator's form editor utility.....	66
Figure 31: Class diagram showing relationships between user interface classes .....	67
Figure 32: Configuration of signal generator recording test setup. ....	68
Figure 33: Diagram of test hardware configuration .....	69
Figure 34: Screenshot of input screen showing the file table populated with calibration recording files. ....	71
Figure 35: Screenshot of calibration results screen, showing gain curve and numeric data. ....	73
Figure 36: Screenshot of payload view screens showing continuous (left) and pulsed (right) waveforms .....	74



Figure 37: Computed power of signals from the signal generator directly connected to the ADC (solid line) and actual input power from the generator (dashed line) .....	75
Figure 38: Plot of the difference between actual and expected ADC values. Results are shown for linear region, -70 dBm input and above .....	76
Figure 39: Results from manual and computed calibration of test receiver with no added attenuation and a CW input signal .....	78
Figure 40: Deviation between manual calibration and calibration tool results in dB. Results are shown for linear region, -100 dBm input and above .....	79
Figure 41: Pulsed calibration results compared to corresponding continuous calibration results for 0 dB IF attenuation setting .....	80
Figure 42: Screenshot of payload waveforms of pulsed calibration for input power of -90 dBm (left) and -120 dBm (right). Pulse is buried within the noise. ....	81
Figure 43: Results from manual and computed calibration of test receiver with 31 dB of IF attenuation and a CW input signal .....	82
Figure 44: Deviation between manual calibration and calibration tool results in dB. Results are shown for linear region, -90 dBm input and above .....	83
Figure 45: Pulsed calibration results compared to corresponding continuous calibration results for 31 dB IF attenuation setting .....	84
Figure 46: Receiver output power after 0, 30, and 150 minutes of run time, as calculated by the calibration tool .....	85
Figure 47: Gain of receiver after 0, 30, and 150 minutes of run time .....	85
Figure 48: Calibration tool plots for two receiver setups; nominal and weak LO power .....	86
Figure 49: Unfiltered (left) and filtered (right) in-phase waveforms of output signal corresponding to -100 dBm input power .....	88

Figure 50: MATLAB algorithm plot of calculated power levels of signal generator CW tones ....	89
Figure 51: Unfiltered In-phase waveform of -130 dBm signal from signal generator.....	90
Figure 53: Bandpass filtering algorithm results compared with calibration tool results (without filtering) and manual calibration results.....	91
Figure 56: Simplified circuit schematic of hardware test receiver.....	100
Figure 57: LNA A1 datasheet gain vs. frequency for -55 °C, +25 °C, +85 °C..	102
Figure 58: RF Amp A2 datasheet gain vs. frequency for -55 °C, +25 °C, and +85 °C .	104
Figure 56: RF BPF FL2 attenuation (dB) versus frequency (GHz).....	106
Figure 60: RF Amp A3 datasheet gain vs. frequency for -55 °C, +25 °C, and +85 °C. ....	108
Figure 61: ATT1 - 5 datasheet attenuation vs. frequency. ....	110
Figure 62: Datasheet electrical specs of Marki Microwave T3-04 mixer, (MX1).....	112
Figure 63: IF BPF FL3 insertion loss (dB) versus frequency (MHz).....	112
Figure 64: IF Amps A4, A5 datasheet gain vs. frequency for -55 °C, +25 °C, and +85 °C.....	115
Figure 65: IF LPF FL4 datasheet insertion loss vs. frequency and electrical specs. ....	118

## Table of Tables

Table 1: Calibration tool results from 4 different calibration setups. ....	77
Table 2: Calibration toolkit results for nominal and weak LO power receiver setups .....	87
Table 3: RF BPF FL1 measured insertion loss vs. frequency for +25 °C and +50 °C .....	101
Table 4: LNA A1 datasheet estimated gain vs. frequency for -55 °C, 25 °C, 85 °C. ....	103
Table 5: RF Amp A2 datasheet estimated gain vs. frequency for -55 °C, 25 °C, 85 °C . ....	105
Table 6: RF BPF FL2 graph estimated insertion loss vs. frequency.....	107
Table 7: RF Amp A3 datasheet estimated gain vs. frequency for -55 °C, 25 °C, 85 °C. ....	109
Table 8: ATT1-5 datasheet and calculated attenuation vs. frequency. ....	111
Table 9: IF BPF FL3 graph estimated insertion loss values vs. frequency.....	114
Table 10: IF AMP A4, A5 datasheet estimated gain vs. frequency for -55 °C, 25 °C, 85 °C. ....	116
Table 11: Receiver gain tests for LNA temperatures of 0 °C, +25 °C, +50 °C.....	119
Table 12: Comparison of manual calibration and calibration tool results for CW calibration of test receiver set to 0 dB IF attenuation. ....	120
Table 13: Comparison of manual calibration and calibration tool results for CW calibration of test receiver set to 31 dB IF attenuation .....	120
Table 14: Comparison of continuous and pulsed waveform calibration tool results with test receiver set to 0 dB IF attenuation .....	121
Table 15: Comparison of continuous and pulsed waveform calibration tool results with test receiver set to 31 dB IF attenuation .....	121

Table 16: Calibration tool results without a receiver connected; signal generator input connected directly to the ADC.....	122
Table 17: Hardware receiver gain measured across dynamic range immediately after, 30 minutes after, and two hours and 30 minutes after powering on. Measurements taken for a constant signal frequency.....	123
Table 18: Hardware receiver gain measured across dynamic range for two different LO powers below minimum LO power required by the mixer. ....	124
Table 19: Comparison of hardware receiver gain measurements made with a signal analyzer against calculations of gain made by the calibration tool and a MATLAB implementation of bandpass filtering applied to the output signal. Gain values measured or calculated across receiver’s dynamic range.....	125

## Chapter 1: Introduction

Radar, an acronym for Radio Detection and Ranging, has become an indispensable component in the deployment of defense systems. Capable of acquiring data that can be processed to obtain information such as target speed, shape, and distance, radar provides operators and analysts a detection tool essential in identifying and tracking potential threats. Given this role as a critical component in defense applications, it is of vital importance that a radar system's performance meets specific mission standards, where variations in accuracy could determine success or failure.

MIT Lincoln Laboratory Group 108, Tactical Defense Systems, works to assess air vehicle survivability. Specifically, Group 108 studies vulnerability of U.S. Air Force (USAF) aircraft to weapons systems, electronic countermeasures, and air surveillance radar systems. The group focuses on understanding USAF and threat air defense systems through tests and measurements. Test activities include flight, field, and laboratory testing. The group develops new hardware for testing and prototype systems as well as for instrumenting existing sensors, such as radar systems. The group's activities continue to evolve in parallel with USAF efforts, but the emphasis remains on providing answers to questions from USAF sponsors by analyzing resulting data from field measurements.

In testing and instrumenting radar systems, a key facet to properly evaluating the data is calibration of the radar receiver's gain. With any electronic device, internal design and environmental considerations are contributing factors to variations in performance parameters and must be accounted for if peak operation is to be achieved. Methods of radar receiver gain calibration exist and are employed by Lincoln Laboratory's test engineers and radar operators, but there is a need to package these methods into a single, versatile software toolkit. Ideally, the software would effectively display results via an intuitive graphical user interface (GUI) and could be easily integrated into an encompassing system for radar analysis. This application would be useable in the field, so that flight test operators could calibrate and view results

before and during a mission, ensuring that the radar receiver is functioning properly and preventing wasted test time.

This project consists of two parts. First, the significance of radar receiver gain calibration was demonstrated through modeling a real receiver available to us at Lincoln Laboratory and observing the effects of temperature and signal frequency variations on gain through simulation and measurements on the physical hardware. The gain variation demonstrated by the simulation demonstrates the importance of calibration and motivates the calibration toolkit, which is the final deliverable of the project. The second part of the project was developing the receiver calibration toolkit application, which was written in C++ using the cross-platform Qt application programming interface (API) for GUI development. The toolkit computes radar receiver gain and other useful receiver health and performance measurements and displays the results to the user intuitively. Care was taken to ensure that the application is as useable and versatile as possible. In order to test the toolkit, we recorded calibration data using a physical receiver and a real-time server. With these test data, we verified the software's functionality and quantitatively compared the calibration tool results to manual calibration results. The toolkit is compatible for use and integration by external applications, and in the future it will likely be expanded by Group 108 to provide additional functionality to meet evolving needs. Ultimately, the toolkit will assist and improve flight test practices at Lincoln Laboratory by improving measurement accuracy and efficiency.

## Chapter 2: Background

### 2.1 Radar Range Equation

The radar range equation is the primary formula that applies to all radar systems. Mathematically, this equation describes the relationship between transmitted and received powers, transmitter and receiver antenna gains, radar cross section or RCS of the target (an imaginary area that would scatter a radar wave of the same intensity in all directions as is observed by the receiver antenna), radar signal wavelength, and distances (known as range) to the target from the transmitter and receiver antennas (Skolnik, 1980). In the simplest case, the radar system is taken to consist of a single isotropic antenna: an omnidirectional antenna that radiates electromagnetic waves out in a perfect sphere. For a given distance from the transmission antenna,  $R_t$ , the power density at any point on the sphere is the antenna transmission power divided by the sphere's surface area:  $P_t \frac{1}{(4\pi)R_t^2}$ . Most radars, however, utilize directive rather than isotropic antennas (Skolnik, 2008). Due to concentration of the radar's power in one direction from a directive antenna, the radar has a transmission gain  $G_t$ , which multiplies the isotropic power density:  $P_t \frac{G_t}{(4\pi)R_t^2}$ . The target experiences this increased power density and reflects a portion of it back towards the radar. The intensity of the wave reflected by the target can be represented as an area known as the radar cross section (RCS), denoted by sigma,  $\sigma$ . This RCS measure multiplies the power density incident upon the target, yielding a reflected power of  $P_t \frac{G_t}{(4\pi)R_t^2} \sigma$ . The power density that returns to the radar is  $P_t \frac{G_t}{(4\pi)R_t^2} \frac{\sigma}{(4\pi)R_r^2}$ , where  $R_r$  is the distance between target and receiver antenna. The final power absorbed by the receiver antenna is the power density of the reflected wave multiplied by the receiver antenna's effective area, which can be expressed in terms of its gain and the radar signal wavelength:  $\frac{G_r \lambda^2}{(4\pi)}$  (Knott, 2006). The full bistatic radar range equation is given as:

$$P_r = P_t \frac{G_t}{(4\pi)R_t^2} \frac{\sigma}{(4\pi)R_r^2} \frac{G_r \lambda^2}{(4\pi)}$$

*Equation 1: Bistatic radar range equation.*

The bistatic radar range equation specifically describes a radar system setup in which the transmitter and receiver antennas are at considerably different distances from the target such that they must each be accounted for separately. The more general radar range equation assumes a distance between antennas of not more than an antenna diameter or two, as is the case in most situations (Knott, 2006). With this assumption, the bistatic equation may be condensed to the following, where  $R = R_t = R_r$  is the distance to the target from the antennas:

$$P_r = P_t \frac{G_t G_r \sigma \lambda^2}{(4\pi)^3 R^4}$$

*Equation 2: Radar range equation.*

Likewise, in many applications the transmitter and receiver antennas are the same physical device and thus their associated gains are equivalent (Knott, 2006). This configuration is known as a monostatic radar. Its range equation is as follows:

$$P_r = P_t \frac{G^2 \sigma \lambda^2}{(4\pi)^3 R^4}$$

*Equation 3: Monostatic radar range equation.*

## 2.2 Radar Cross Section

The analysis of an aircraft's susceptibility to detection by a radar system lies in the determination of the aircraft's radar cross section. When a radar emits an electromagnetic wave, a portion of that wave impinges upon, or comes into contact with, the target. The energy of the impinging wave that is not absorbed by the target is scattered out unequally in various directions, with some of that energy returning back to the radar (Knott, 2006). The radar cross section describes the intensity of this "echo" signal by developing the notion of an effective area of a fictitious sphere. Assuming that the target scatters incident radar waves equally in all directions, the energy that returns to the radar can be expressed as the projected area of a metal sphere, several signal wavelengths in diameter, which would scatter a wave of the same intensity back to the radar, were the target to be replaced by this sphere (Knott, 2006). The RCS



of a particular target can vary depending on its orientation to the incident wave and frequency of the radar signal, and several example values are depicted in Figure 4 below to give a sense of typical RCS measurements for military, civilian, and environmental targets.

	<u>Square meters</u>
Small, single engine aircraft	1
Four passenger jet	2
Large fighter	6
Medium jet airliner	40
Jumbo jet	100
Helicopter	3
Small open boat	0.02
Small pleasure boat (20-30 ft)	2
Cabin cruiser (40-50 ft)	10
Ship(5,000 tons displacement, L Band)	10,000
Automobile / Small truck	100 - 200
Bicycle	2
Man	1
Birds	$10^{-2} - 10^{-3}$
Insects	$10^{-4} - 10^{-5}$

*Figure 4: Examples of radar cross section measurements (O'Donnell, 2002).*

In a radar system, identification of a detected target must occur as quickly as possible in order to assess if a potential threat exists. A detectable radar cross section not only alerts an operator to the presence of a target, but may also provide valuable insight in determining the target identity. The power  $P_r$  at the receiver antenna is directly proportional to  $\sigma$ , so highly accurate amplification and signal processing of this power is required at the radar receiver if useful RCS data are to be extracted. Ignoring range, RCS is the only design parameter of the radar range equation controllable by the target (O'Donnell, 2002). Thus, RCS is vitally important in the evaluation of aircraft vulnerability, since it dictates the maximum detectable range of a target. The smaller the RCS, the closer the target must be in order for the radar receiver to perceive the target's echo above noise present in the received signal.

## 2.3 Radar Receiver Design

### 2.3.1 Simplified Single-Conversion Superheterodyne Receiver

From the receiver antenna, a signal is routed through the radar receiver for processing, amplification, and frequency down-conversion, and then sampled by an analog-to-digital converter (ADC) to be stored in a digital format for further processing and interpretation. The ideal receiver would simply sample the received RF signal immediately after filtering and amplification, reducing the number of stages (circuit components) and avoiding the undesirable products output by a mixer during down-conversion. In practice however, most ADCs on the market are not capable of accurately measuring the RF signal directly. Hence, it is common for a radar receiver to employ at least one level of analog frequency down-conversion to an intermediate frequency (IF) that can be accurately measured by a standard ADC. This is because the signal-to-noise ratio (SNR) of an ADC is limited by the device's aperture jitter, the standard deviation of the time delay from the sample command to the actual sampling and digital conversion, and clock jitter, the fluctuations in the clock period (Dazhuan, Shenghua, & Xueming, 2005). Both phenomenon affect noise performance more severely with increasing input signal frequency (Dazhuan *et al.*, 2005). Due to the Nyquist theorem, the ADC would need to be able to sample at minimum twice the highest signal bandwidth in order not to lose any information, which translates to very high sampling rates for radar signals. While some devices do exist that are capable of effectively sampling at radio frequencies, such as Texas Instruments' 12-bit ADC12Dxx00RF product line, their complexity makes them very expensive.

The predominant design in radar receivers is the superheterodyne architecture (Skolnik, 2008). While the circuitry of such a receiver is often more complex than that shown below in Figure 5, the basic functionality performed can still be described in terms of the depicted simplified example.

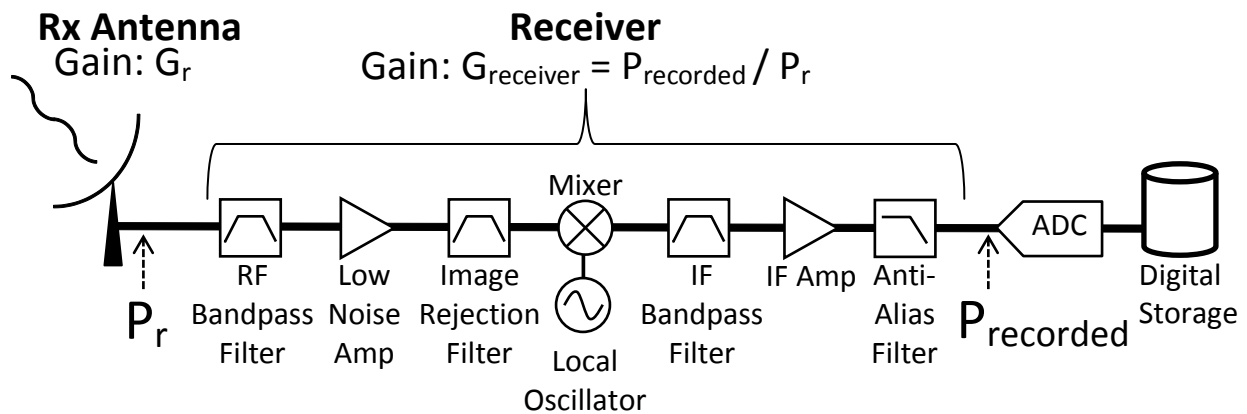


*Figure 5: Simplified single-conversion superheterodyne receiver chain example. Real receivers often have many more stages and components.*

As shown in Figure 5, the signal received directly from the antenna is first sent to a RF bandpass filter (BPF). Centered near the carrier frequency of the desired signal, the RF bandpass filter is used to remove all frequencies outside the radar's receive band. However, since any attenuation introduced by the first RF stage has a direct impact on the receiver noise figure (the SNR degradation in dB of the entire receiver), the RF bandpass filter is designed to sacrifice some frequency selectivity in favor of preserving minimal power loss (Razavi, 2011). The result of this trade-off is inadequate attenuation of receive band interference, exemplified in Figure 6, where LNA represents the low noise amplifier following the RF bandpass filter.

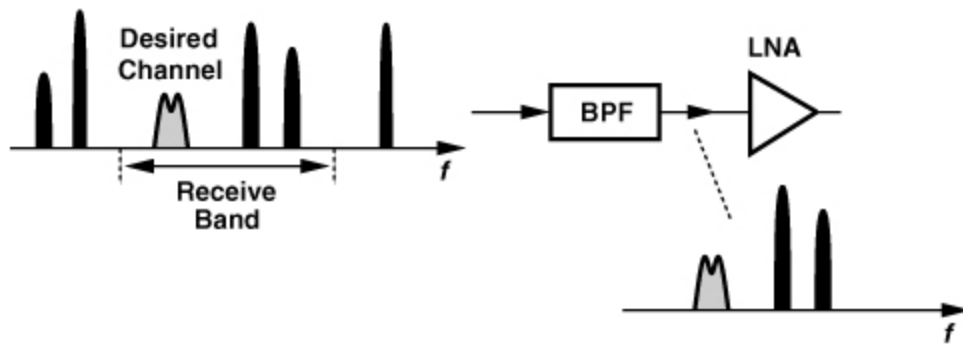


*Figure 6: Frequency selectivity of RF bandpass filter. The spectrum of the received waveform, shown on the left, contains in-band and out-of-band interference as well as the desired signal. The limited selectivity of the filter removes out-of-band interference but passes in-band interference along with the desired signal, shown on the right (Razavi, 2011).*

The LNA is used to boost the power of the desired signal while introducing little noise into the signal path. Though any linear amplifier equally increases signal and noise powers at the same frequency by the same factor, each component in the receiver chain contributes additional noise to the signal; thereby the receiver noise figure increases (the overall SNR degrades). The LNA, then, becomes essential in amplifying the desired signal while the system noise is still relatively low. Continuing through the receiver chain of Figure 5, the signal leaving the LNA is sent to an image rejection filter. During down-conversion, there is a specific frequency, known as the image frequency, which mixes directly down to the exact same IF at which the desired signal is down-converted. The image frequency is dependent on the desired signal frequency and the IF. As depicted in Figure 7, once any interference is brought down to the IF, it cannot be attenuated by a linear filter without also affecting the desired signal. Due to the lack of attenuation by the RF bandpass filter in the interest of minimizing in-band loss, an image rejection filter is inserted between the LNA and mixer. The placement of this filter, which acts as a bandpass filter, is such that the image frequency interference is highly attenuated prior to down-conversion without severe cost to the receiver's noise figure (Razavi, 2011).

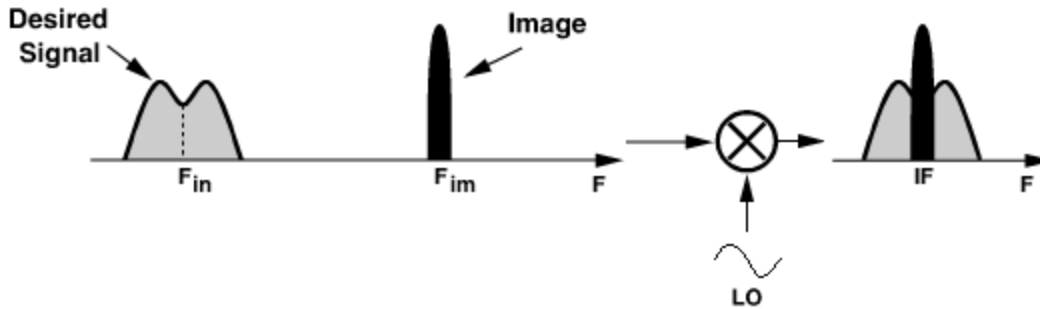


Figure 7: The image frequency  $F_{im}$  mixes directly to IF, creating interference with the desired signal  $F_{in}$  (Razavi, 2011).

From the image rejection filter, the signal is routed through the mixer, which performs down-conversion of the RF signal to the IF by means of a local oscillator (LO) frequency. The signal frequencies output by an ideal mixer are  $f_R + f_{LO}$  and  $f_{LO} - f_R$ , where  $f_R$  is the received RF signal frequency and  $f_{LO}$  is the LO frequency (Skolnik, 2008). Depending on system requirements, either high-side injection (a LO frequency above the desired signal carrier frequency) or low-side injection (a LO frequency below the desired signal carrier frequency) is used to produce the same IF signal (Razavi, 2011). Thus, the choice of LO frequency determines which frequency output by the mixer is down-converted, the other being up-converted. In practice however, the mixer produces spurious or unwanted signals at frequencies  $\pm n f_{LO} \pm m f_R$  (where  $n$  and  $m$  are integers) along with the up- and down-converted signals (Skolnik, 2008). To remove these spurious products and the up-converted signal, a bandpass filter centered on the IF is utilized just after the mixer. A second amplifier designed to operate at the intermediate frequency follows the IF bandpass filter, again enhancing the signal power. This amplifier, along with the LNA, also serve to boost the desired signal close to the maximum amplitude the ADC can convert in order to utilize the ADC's highest resolution. Finally, the signal is processed by a lowpass filter acting as an anti-alias filter to limit the bandwidth of signals entering the ADC (Skolnik, 2008). Because the Nyquist theorem requires that the sample rate be at least twice the highest signal bandwidth in order to preserve all signal information, the anti-alias filter removes frequencies above the desired signal frequency to prevent corruption of the desired sampled signal.

Each of these components influences the overall receiver gain. When the components are all impedance matched at their inputs and outputs, reflections of signal waves from the input of one component back toward the output of the previous component is minimized (Kalivas, 2009). Under this condition, the recorded power output by the receiver is the product of each component's gain and the power input to the receiver as shown in Equation 4 (Davis, 2011).

$$P_{recorded} = P_r G_1 G_2 G_3 \dots G_k$$

*Equation 4: Receiver output power recorded by the ADC is the product of the received power and the gain of each component (Davis, 2011).*

The entire receiver's gain is thus the product of every individual component's gain. More commonly, the receiver's gain is reported in decibels (dB), the base-10 logarithm of the gain multiplied by 10 (when working with power). By applying the product rule of logarithms,  $\log(ab) = \log a + \log b$ , the gain of the receiver in dB is the summation of the component gains in dB, displayed in Equation 5.

$$G_{receiver (dB)} = G_1 (dB) + G_2 (dB) + G_3 (dB) + \dots + G_k (dB)$$

*Equation 5: Receiver gain in dB. Summation of each component's gain in dB equals entire receiver's gain.*

### 2.3.2 Gain Dependency

For many radar applications, such as target speed calculation or ranging, the precise amplitude of the received signal is not important, so long as it is distinguishable from noise, since these metrics operate on principles of frequency or time difference. However, when measuring the radar cross sections of aircraft, the precise amplitude of the signal received by the antenna, and thus also the receiver gain, is crucial (Skolnik, 2008). Where receiver gain in dB is the difference between recorded power  $P_{recorded}$  and received power  $P_r$ , and received power is directly proportional to RCS  $\sigma$ , the calculation of a target's RCS depends on the gain determined for the receiver. Hence, the receiver must be calibrated so that its gain is known to

a high degree of accuracy. Because the receiver gain can vary depending on the test environment, it must be determined by calibration at the test site.

## **2.4 Radar Receiver Gain Calibration**

### **2.4.1 Receiver Dynamic Range, Noise Floor, and 1dB Compression Point**

An important attribute of the response of a radar receiver system is the receiver's dynamic range. This parameter describes the span of input signal powers over which the receiver can be expected to perform according to its intended behavior (most often being a linear response), characterizing both the upper and lower bounds of the system (Skolnik, 2008). These bounds are established by physical limitations and imperfections inherent in the electrical components that comprise the receiver. The dynamic range is depicted in Figure 8. The bottom of this range is defined by noise generated internally by the individual components as well as the noise present at the input to the receiver from the radar antenna (Skolnik, 2008). Known as the noise floor, this lower limit of the receiver's sensitivity to small signals sets the minimum input power level required to produce an output power perceivable from the noise. At the other extreme of the dynamic range is the compression or saturation region. When the receiver enters the compression region, the amplitude of the recorded power converges to a constant value, resulting in decreasing gain for increasing received signal powers (Razavi, 2011).

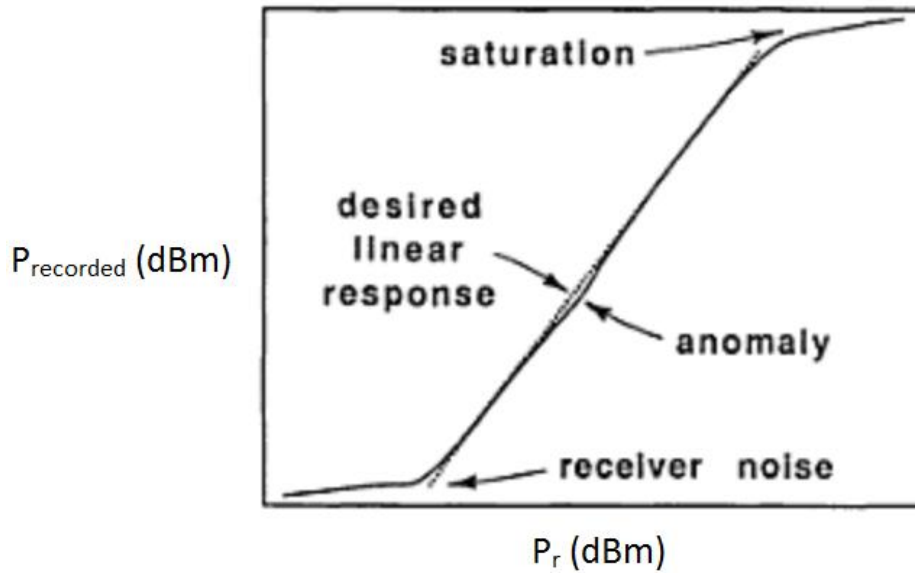
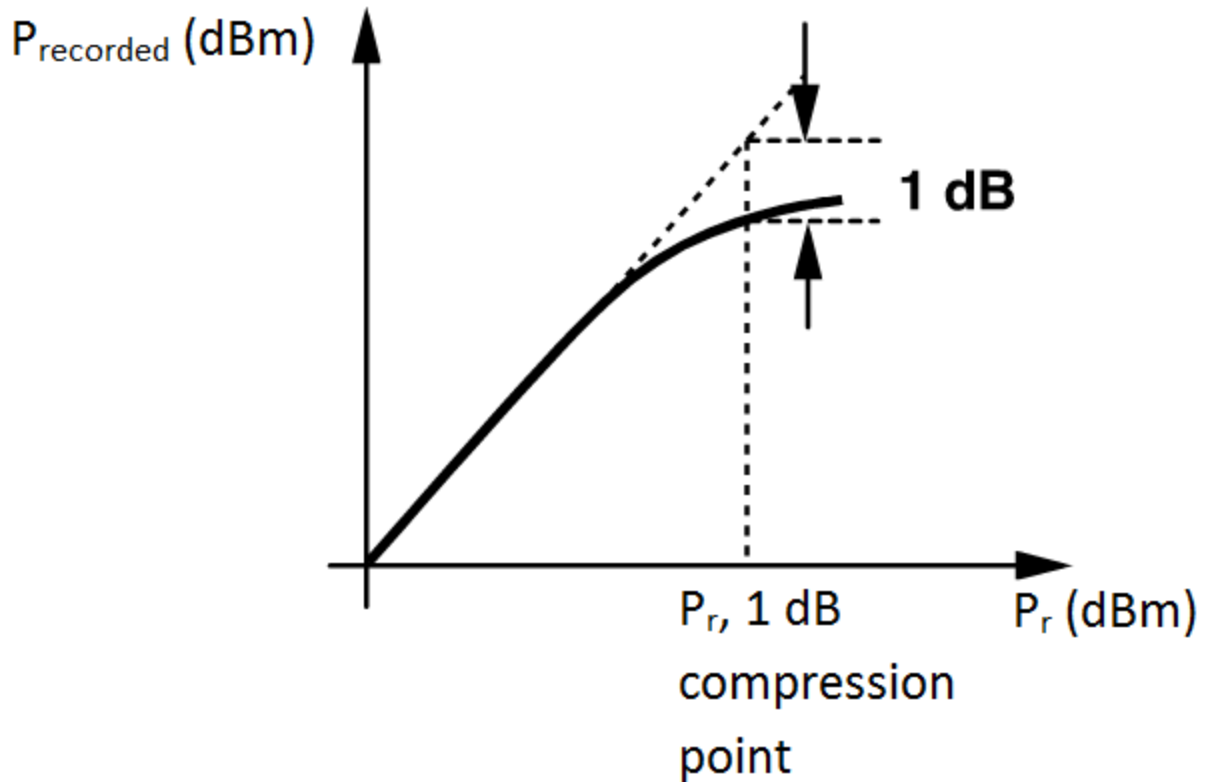


Figure 8: Example gain plot showing receiver noise or “noise floor”, linear, and saturation (compression) regions (Knott, 2006).

The standard metric used to identify the onset of compression is the 1 dB compression point, the input power level at which the receiver’s gain is 1 dB less than the gain of the linear response region (Skolnik, 2008). An illustration of the 1 dB compression point is shown in Figure 9. Beyond this point, the receiver’s output converges to a maximum level for increasing input power, placing an upper bound on the receiver’s performance. The components within a receiver that are capable of saturating are those that possess nonlinear response regions, primarily mixers and amplifiers (Skolnik, 2008).





*Figure 9: Expanded view of the onset of receiver compression. The input power at which the receiver's gain is 1 dB less than the gain of the desired linear response is the 1 dB compression point (Razavi, 2011).*

Due to component noise and compression factors, most receivers have a dynamic range no greater than 60 or 70 dB (Knott, 2006). The span of the dynamic range determines the resolution or measurement precision of the receiver. The greater the dynamic range, the more precisely the receiver can respond to subtle changes in the input signal.

#### 2.4.2 Receiver Gain Calibration Process

The calibration process consists of a series of gain measurements, performed through bypassing the receiver antenna and injecting a known test signal into the receiver at the RF bandpass filter's input. The output signal is measured, and the ratio of the output signal power to input signal power in dB is then computed. The simplest test signal is a continuous waveform (CW) signal, or a sine wave, which can be created using a signal generator. Additionally, the

known signal can be a pulsed sinusoid generated using the pulse feature of a signal generator. For CW input signals, the corresponding output power can be measured by using a signal analyzer on a general setting. For pulsed signals, the output power can be found by using a signal analyzer on a time-domain setting, at the output frequency, to measure the power of the signal during the pulse. Occasionally, receiver calibration is performed while the radar transmitter is outputting pulsed signals, and in order to eliminate the effect of interference from the transmit pulses, the measured receiver pulses must occur long after the transmit pulses.

In the case of receiver gain calibration, flight test operators need to examine the gain of the system over its entire dynamic range (Gekat, Mehl, Rühl, & Verstappen, 2003). To acquire the full dynamic range response, multiple gain measurements are made using different input signal powers. Starting from an input power level at the noise floor, the input power is incremented in steps up to a power level well past the point where gain compression takes effect. By incrementing the input power level across this range while measuring the input and output power at each step, the full linear region of the gain curve can be observed and analyzed. This procedure allows the operator to verify whether the receiver is functioning as expected or not.

Given the imperfect nature of electrical devices, the components within the receiver will inevitably vary in performance. The combined effects of factors such as component tolerances, frequency response, temperature, and aging on each component impact the system performance (Skolnik, 2008). Hence, deviations from the expected gain curve occur, giving rise to the need for frequent calibration of the receiver to ensure measurement accuracy. Because the existing calibration process requires manually incrementing the input power of a signal generator, manually measuring the output powers on a signal analyzer, logging these measurements, and then computing and plotting a gain curve, calibration can be a relatively lengthy task. Often, the results from the calibration are not available to the operator before the mission, since the calibration data are not reviewed by an analyst until well after the mission. Furthermore, the practices between Group 108's radar operators differ significantly, where one

operator may calibrate once a year while another calibrates at least once every test flight. Thus, there is interest in determining how regularly calibration must actually occur.

## 2.5 Analog-to-Digital Converters

Analog to digital converters, or ADCs, are often the final stage of the receiver chain. In most modern systems, the intermediate frequency output of the receiver is sampled by an ADC in order to obtain a binary value that represents the voltage at that instant. The process of converting a voltage into a binary value is called quantization. From there the data can be stored to disk, used in computation, or put to other use.

### 2.5.1 ADC Error

An ideal ADC should quantize the signal perfectly linearly throughout its full-scale voltage range. In reality there are factors that cause nonlinearities, such as offset error, gain error, and quantization error.

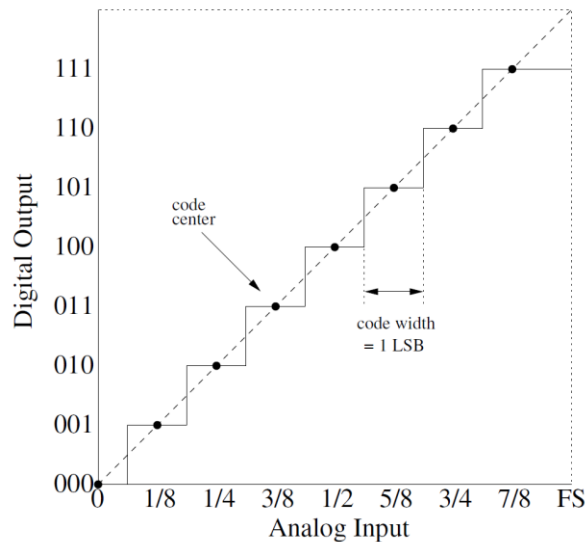
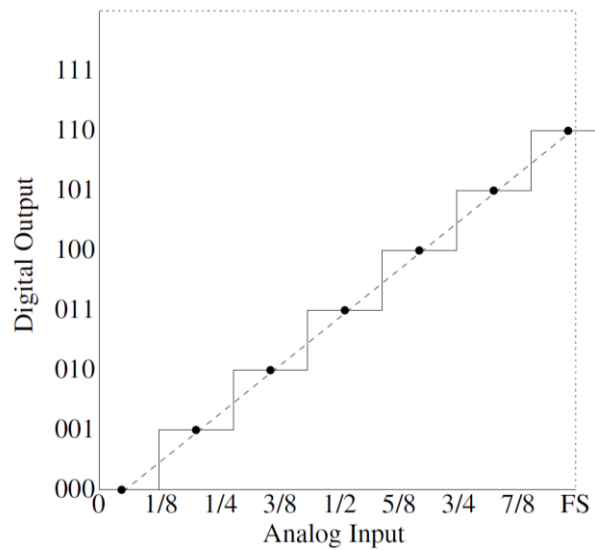


Figure 10: Ideal ADC behavior (Lundberg, 2002).

Offset error is the difference between the ideal output and the actual ADC output shown in Figure 10. Ideally, the voltage at which the first transition occurs is half of one code width. Code width is the voltage step represented by one bit, which can be obtained by dividing the dynamic range by the binary resolution. If offset error is present, it is easily observable close to zero

volts, since the first transition will not occur at half of one code width. Graphically, the “code center” line as shown in Figure 10 will not pass through the origin. Similarly, gain error is present when the slope of the ADC’s quantization deviates from the ideal  $2^N/V_{FS}$  value, such that the maximum binary output does not correspond with the intended full-scale voltage, which is defined as the maximum amplitude (in Volts) that the ADC can convert. Both these effects are seen in Figure 11; notice that the dotted line does not intersect with the origin or the maximum digital output level.



*Figure 11: Behavior of an ADC exhibiting gain error and offset error (Lundberg, 2002).*

A perhaps more prevalent factor in the processing of ADC data is quantization error, which is effectively the introduction of additional error into the signal as a result of quantization. A voltage is encoded as a binary value that represents the small range of voltages between two transition levels, thus some of the precision is lost (Lundberg, 2002). At high voltage levels, the relative effect is negligible, but at low voltage levels where the binary value output is low, the effect can result in significant percent error. In addition, the input signal to the ADC will likely have its own noise, which can impact the quantization by a few bits. Again, the error caused by the ADC’s noise will be more evident at low signal levels. For receiver calibration, this phenomenon means that gain measurements for small signals will be more susceptible to error.

### 2.5.2 I/Q Data

High-speed ADC's used in radar systems are often equipped with signal processing implemented on an FPGA that extracts the in-phase (I) and quadrature-phase (Q) data from the waveform. I/Q data are a mapping of the amplitude and phase of a sinusoidal signal into a Cartesian coordinate system, rather than a polar coordinate system. This mapping simplifies signal processing algorithms and is the standard format of radar data recordings. All radar applications use sinusoidal signals, whether pulsed or continuous. The I component of the signal is the real component, and the Q is the imaginary component. As the sine wave continues, the phase increases, rotating counter-clockwise in the polar domain. In the Cartesian coordinate system, this rotation causes the I/Q vector to follow a circular path (Smith, 2008). For a sine wave with constant amplitude, the I value always leads the Q value by 90 degrees.

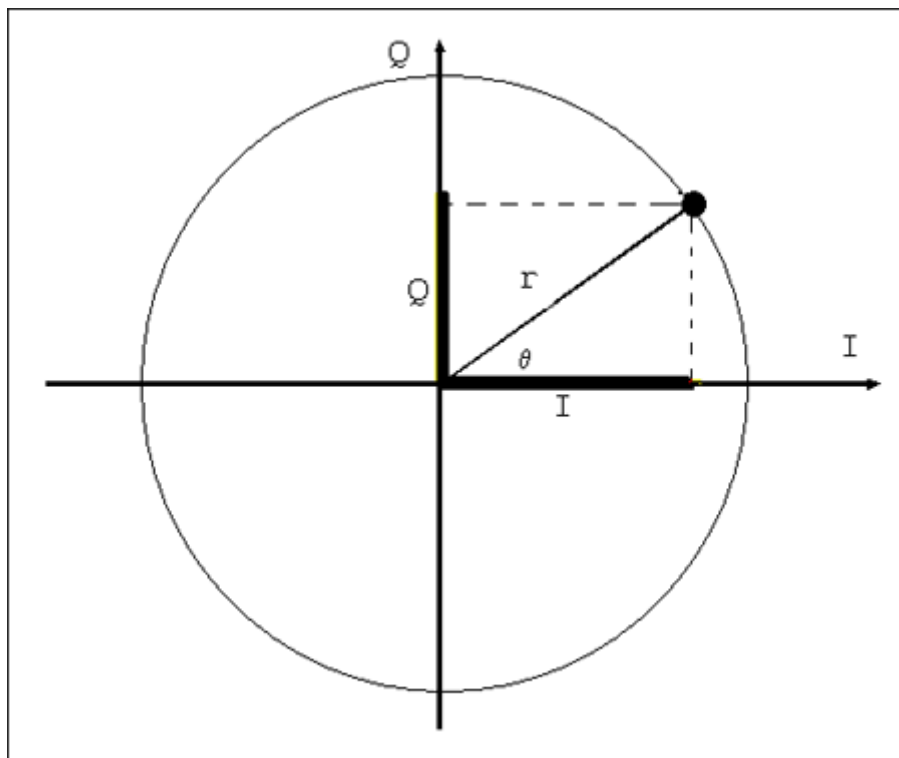


Figure 12: Plot showing I/Q vector and circular path of I/Q data points in a sinusoid (National Instruments, 2006).

The I/Q data format simplifies calculating signal amplitude, since at any given point of the signal, the amplitude can be computed using Equation 6. The amplitude is the length of the I/Q vector, represented as  $r$  in Figure 12. An accurate amplitude calculation requires averaging of multiple instantaneous amplitudes to reduce the effect of noise.

$$r = \sqrt{I^2 + Q^2}$$

Equation 6: Amplitude of signal from I/Q data.

## 2.6 Radar Systems at Lincoln Laboratory

### 2.6.1 Radar Open System Architecture

As mentioned previously, Lincoln Laboratory fields and operates a variety of radar systems. Each of these systems is unique, but many of them utilize Radar Open System Architecture (ROSA), an effort developed at Lincoln Laboratory to standardize radar system interfaces by using commercial-off-the-shelf (COTS) components and pre-defined standards (Rejto, 2000). An illustration of the difference between custom and ROSA radar systems is shown in Figure 13.

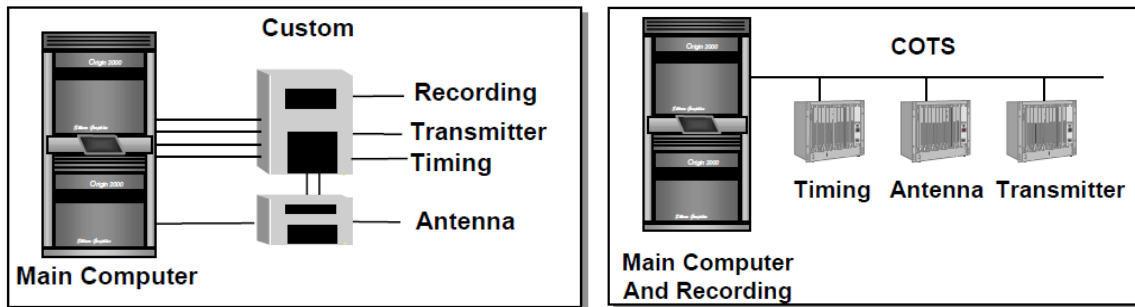


Figure 13: Diagram showing the difference between a customized radar system (left) and a ROSA radar system (right).

Our calibration toolkit benefits from the fact that all ROSA systems store data in pre-defined, standardized file formats. The most up-to-date version of these formats is ROSA II, which we use in our project. The most commonly used ROSA II file format for storing waveform data is Pulse Short T (PST), which records data as segmented payloads of variable length. Our tool operates on recordings stored in this format for calibration. Radar operators can record

PST files of continuous wave (CW) signals or pulsed signals, but pulsed signals are more frequently used since real radar systems often use pulsing to detect range or velocity. In a pulsed recording, each of the payloads within the file contains data over one pulse repetition interval (PRI), the time between two consecutive pulses. When the entire radar system is operational, the PRI starts with the transmission pulse, and the received pulse occurs at some later time in the PRI after it has reflected off of the target and returned. When calibrating with a CW test signal, each payload contains a slice of the CW signal, and the payloads are not contiguous. When calibrating with a pulsed test signal, the PRI is triggered by the sync pulse from the signal generator, which is connected to the ADC's trigger port. The signal generator is configured to delay the pulse to ensure the pulse occurs somewhere in the middle of the payload.

PST files consist of one file header followed by a series of payload headers and payloads. The file header contains the ROSA version number, the number of messages in the file, and the start and end timestamps. Each payload header contains the time at which it was recorded and the payload size in bytes. In the context of this project, radar operators generally record the data as I and Q values rather than amplitude values, so each payload simply contains the I and Q values of the data interleaved as signed short ints, a 16-bit data type. The I/Q data continue until the next payload header.

### **2.6.2 Post-Mission Analysis**

To store, manage, and manipulate radar data, Group 108 has developed the Post Mission Analysis (PMA) application. A screenshot of the main PMA window is shown in Figure 14. Radar analysts can import recordings in any ROSA format to a central database, as well as add documents and metadata containing information about the recording. This database can then be easily queried for recordings by name or by some other field. A current development initiative is to incorporate analysis tools so that analysts can work with a set of mission data directly from PMA. One existing feature is that the user can launch MATLAB from PMA so that the working directory includes the selected data. Additional analysis tools, such as our receiver calibration tool, will increase the value of PMA as a comprehensive radar toolkit.

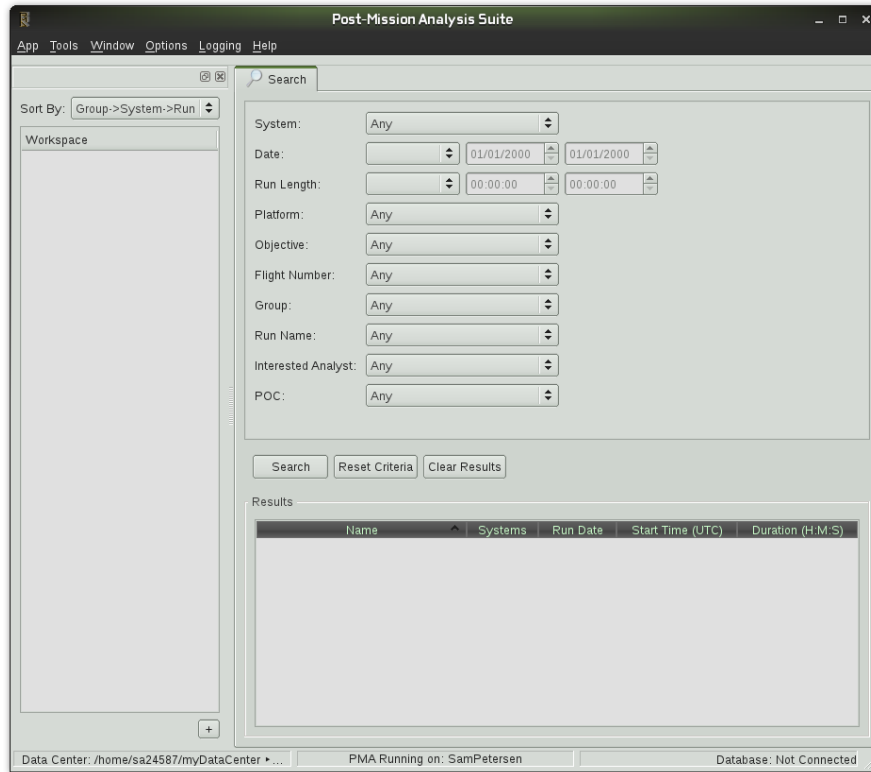


Figure 14: Screenshot of the main window of Post-Mission Analysis Toolkit.



## **Chapter 3: Radar Receiver Simulation**

### **3.1 Introduction: Motivating the Gain Calibration Toolkit**

Any radar system deployed in the field is exposed to non-ideal conditions that can adversely affect the performance of the radar. Operators must have a sense of how these factors will affect their system and, even more importantly, when it is necessary for them to calibrate their equipment to counteract inconsistencies. A valuable approach in determining the impact of a parameter on a radar system is simulating various test conditions for a model of real hardware. In the absence of extensive testing capabilities, simulation grounded in accurate empirical data such as that provided by a vendor of a component or by small-scale testing can demonstrate performance variation of a system and provide a high degree of confidence in extrapolating for untested conditions. To motivate the need for an intuitive and versatile software tool that will encourage more effective calibration practices in the field, a model of our test hardware receiver was developed and its gain simulated for changing received signal frequencies and operating temperatures.

### **3.2 Methods of Simulation Model and Hardware Test Measurements**

#### **3.2.1 Model Basis**

The approach taken in constructing our model identified each core component of our hardware receiver cascade and compiled (from its datasheet or related material the vendor generated) gain or insertion loss (attenuation) as a function of frequency and temperature. Specifically, vendors measured their components' gain or attenuation values at many frequencies both within and beyond the devices' frequency bands of operation, usually taking these data points at room temperature (+25 °C) as well as the maximum and minimum operating temperatures. The manner in which these data were reported varied between components, thus several methods were employed to extract the information appropriate for the model.

Figure 15 is a simplified version of the receiver's schematic, depicting only the components that need be simulated by our model, therefore serving as our model's block diagram. These

components define the core gain functionality of the receiver, thus analysis and modeling of components contributing to supplementary features were ignored for the purposes of this project. The first three filters of the receiver schematic, FL1, FL2, and FL3, are the only components not labeled with a specific device number, since these parts were custom ordered. To incorporate these filters into our model, we contacted the vendor directly for performance data as well as took test measurements.

The design of the test hardware follows the typical superheterodyne receiver configuration described in Chapter 2, with two additional RF amplifier stages (A2 and A3) and an extra IF amplifier stage (A5) beyond the stages discussed in Chapter 2. The addition of these amplifiers is necessary to supplement the relatively low gains of A1 and A4 in maintaining a low noise figure and boosting the desired signal to the ADC's full-scale value. Several attenuators (ATT1-5) are also included to reduce the power of large interference signals, such as those reflected by objects very near to the radar receiver antenna. The hardware contains the familiar RF bandpass (FL1) and image rejection (FL2) filters, mixer (MX1) and local oscillator (LO) for frequency down-conversion, IF bandpass filter (FL3), and an anti-alias lowpass filter (FL4) to facilitate proper analog-to-digital conversion.

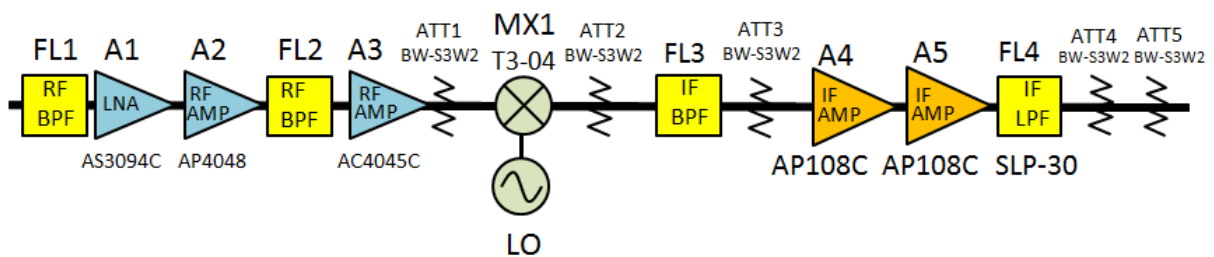


*Figure 15: Simplified circuit schematic of hardware test receiver. Components not necessary to the core functionality were omitted. Components without model numbers were custom ordered.*

*Each component displayed in this schematic was simulated in our model.*

Each amplifier in Figure 15 was manufactured by Teledyne-Cougar, located in Mountain View, California, who provides on each of their datasheets a graph of the particular device's gain versus frequency response for operating temperatures of -55 °C, +25 °C, and +85 °C. Data

used in simulating these components were estimated directly from these graphs. Likewise, the vendor of the custom filters FL2 and FL3 (Reactel, Incorporated, Gaithersburg, Maryland) sent us plots of insertion loss versus frequency from which we estimated values for the model. Values for the mixer MX1 (Marki Microwave, Morgan Hill, California) and the lowpass filter FL4 (Mini-Circuits, Brooklyn, New York) were provided in tables of typical performance data and electrical specifications. Model data for the attenuators, also Mini-Circuits devices, were taken from a table for typical performance at +25 °C and then extrapolated for -40 °C and +85 °C using the temperature coefficient of attenuation provided with the electrical specifications. Since no vendor data could be acquired for the custom filter FL1 (K & L Microwave, Salisbury, Maryland), test measurements were taken to determine the component's insertion loss over frequency at room temperature (approximately +25 °C) and +50 °C. Extrapolation was then performed to determine the filter's insertion loss at -40 °C and +85 °C. Due to the limited data available for certain components, several assumptions were made based on feedback from one of our Lincoln Laboratory mentors and correspondence with representatives from the manufacturers of these components. Estimated values from vendor-provided graphs, measured values for FL1, assumptions made, and further details are listed in Appendix A.

### 3.2.2 Model Functionality

The intent of the simulation was to quantify the effects of received signal frequency and operating temperature on the gain of our receiver; therefore gain was analyzed as a function of both of these parameters. Due to differences in the test conditions measured by the vendors and ourselves for various components, linear interpolation was employed to determine the system response at a common set of frequency and temperature conditions. Through defining a linearly spaced frequency array within the smallest range of all vendor and self-tested frequencies, the gain or loss of each component was calculated at the points in this array for a fixed operating temperature, and then repeated for each temperature tested for that particular component. Because linear interpolation was employed, gain or loss at frequencies other than those specified in the common frequency array could be determined from the line connecting each consecutive pair of vendor-tested values, as seen in Figure 16 on the left. Since the

vendor-tested operating temperatures are not consistent across all components, the most restrictive range imposed by any of the components' ratings, -40 °C to +85 °C, was used for the receiver model. Components with maximum or minimum operating temperatures exceeding either boundary of this range were interpolated for their gain or loss at the model limits using the two vendor-tested temperatures closest to a model temperature limit. This process was performed at every frequency of the common frequency array. The entire receiver model's performance at -40 °C, +25 °C, and +85 °C for the common input signal frequencies was thus determined by the cascade (logarithmic summation) of the individual components' gain or loss responses across frequency for each temperature. To obtain a resolution of gain versus temperature better than three temperature-gain values for a given frequency, each consecutive pair of values was connected with a line, as was done with gain or loss values versus frequency. An example of this process is shown in Figure 16, where the gain at -40 °C, +25 °C and +85 °C is interpolated for several frequencies from the vendor-measured gain values (left) and then linearly connected across temperature for a fixed frequency F2 (right).

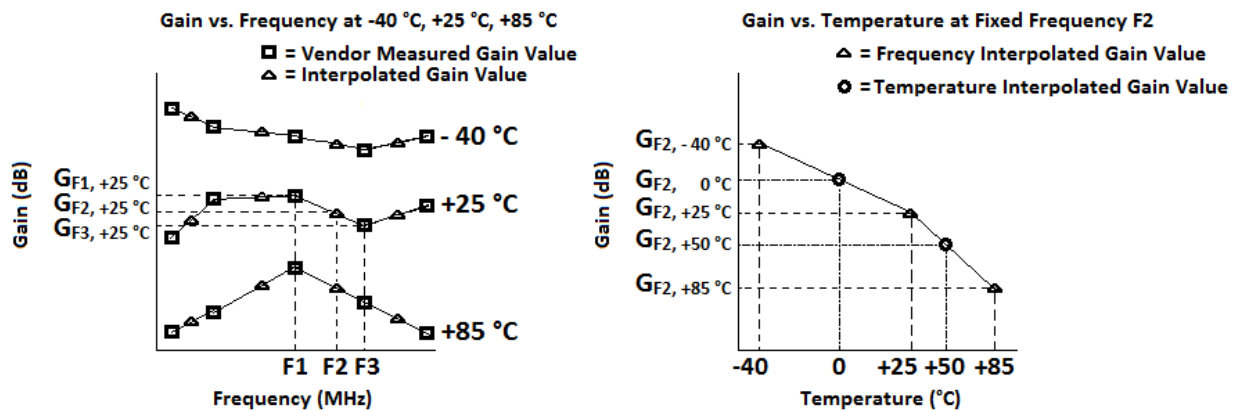


Figure 16: Graphical example of linear gain interpolation over frequency and temperature. The gain at frequency F2,  $G_{F2}$ , is interpolated from the vendor-measured gains  $G_{F1}$  and  $G_{F3}$  for -40 °C, +25 °C and +85 °C operating temperatures (left).  $G_{F2}$  is then determined for 0 °C and +50 °C (right).

The receiver that we modeled operates in only a small portion of S-band (2 – 4 GHz) due to its highly selective second RF bandpass filter FL2, and thus the input signal frequency array

spans only a small range of frequencies. A second frequency array over a greater bandwidth was also defined to simulate the receiver's response to frequencies outside its band of operation. The step size between each frequency in the first array was chosen to be 1 MHz, paralleling our test procedure practice of measuring gain at 1MHz steps due to the tight passband of the hardware, which is only about 6 MHz wide. The second frequency array was defined with a greater resolution of 190 points from 2987.5 MHz to 3032.5 MHz, yielding step sizes of approximately 237 kHz.

### **3.3 Hardware Test Measurements**

To determine the accuracy of our model and establish a margin of error, several test measurements were taken on our hardware receiver. Though these tests were not comprehensive due to time and resource restrictions, they serve as experimental data against which to compare the model's performance as well as the model data for the first RF bandpass filter, FL1.

Our primary objective in performing temperature tests was to analyze the influence of temperature on system gain by producing gain versus frequency curves for the physical receiver at the operating temperatures -40 °C, +25 °C and +85 °C, similar to those shown in Figure 16. Not having access to a temperature chamber, the desired effect could only be approximated by cooling and heating individual components. Given the time that would have been needed for full testing of every component, we chose to vary the temperature of just the LNA (A1) of the receiver. In this way we were able to take data with which to validate our model. The orientation of the LNA within the hardware setup allowed us to alter the LNA's temperature without removing it from the circuit; hence measurements of the entire receiver's gain were taken at different LNA temperatures. To realize cooling of the LNA, we utilized an EFFA duster, which, when turned upside down and pressed, sprays cold Freon gas. Heating was accomplished with a heat gun. Temperature readings of the LNA's package were frequently taken via a thermocouple and Fluke 179 True RMS Multimeter.

The lack of stringent control over the cooling and heating process through proper instrumentation, as well as the potential for component damage, limited the range of

temperatures we were able to achieve to approximately 0 °C to +50 °C. Colder temperatures were more difficult to maintain for any length of time and as a result only one measurement at 0 °C was taken. Stability around +50 °C was more manageable, so our measurements primarily compare the hardware receiver's performance at LNA temperatures of +25 °C (room temperature) and +50 °C, with all other components kept at +25 °C. Because we had no control over the soak time of the LNA, the time it takes for temperature changes to propagate through the device packaging to the circuitry, our achievable temperature range may have been more restricted than what was measured.

To take a measurement for a given temperature, a continuous wave signal at an input power of -70 dBm, which lies within the linear region of our test hardware, was injected directly into the receiver from a signal generator and the power output of the receiver measured with a spectrum analyzer. This procedure was repeated for several frequencies in 1 MHz steps, roughly spanning the receiver's band of operation. Calculation of the gain was done manually from the power measurements.

As described in section 3.2.1 there were no data available for the custom-ordered K & L Microwave RF bandpass filter FL1 that precedes the LNA in the hardware. Therefore, we conducted a brief testing of the filter's insertion loss versus frequency at room temperature and +50 °C. The filter output was connected directly to an Agilent Technologies N5230A PNA-L Network Analyzer and the digital trace used to determine insertion loss values at different frequencies. The heat gun was again used to induce the desired temperature change, with measurements made on the thermocouple and multimeter.

### **3.4 Model Implementation in Matlab and Simulink**

To programmatically simulate our model and graphically display variations in its gain, we coded our model functionality as Matlab scripts, encapsulated into Simulink blocks to create an intuitive component level layout mirroring our hardware schematic. Each block in the receiver model chain is a subsystem that represents one physical device contained within the hardware's configuration. Within each subsystem are Matlab functions that define the component block's gain or loss from vendor-provided or measured data, interpolate the

component's gain or loss value at each point in the common frequency array for fixed temperature, add the block's values to the cascade of the previous blocks' values, and pass the accumulated system performance on to the next component block. A two column matrix, where the first contained gain and loss values and the second frequencies, was used to pass the cascaded performance and the model's common frequency array between blocks. Since there are two distinct frequency ranges at which the model operates, RF and IF, the mixer block takes each radio frequency from the common frequency array and subtracts the value of the LO frequency defined to create a downshifted array of intermediate frequencies.

Five separate simulations of our model were executed. In the first three configurations, the entire receiver model was set at  $-40\text{ }^{\circ}\text{C}$ ,  $+25\text{ }^{\circ}\text{C}$ , and  $+85\text{ }^{\circ}\text{C}$ , respectively. In the last two configurations, our model was simulated with an LNA temperature of  $0\text{ }^{\circ}\text{C}$  and  $+50\text{ }^{\circ}\text{C}$ , respectively, while the other components in the receiver model were kept at  $+25\text{ }^{\circ}\text{C}$ . These final two configurations were run for the purpose of comparing the model with the test data we were able to collect. The full Simulink model of the receiver simulated at  $+25\text{ }^{\circ}\text{C}$  is shown in Figure 17.

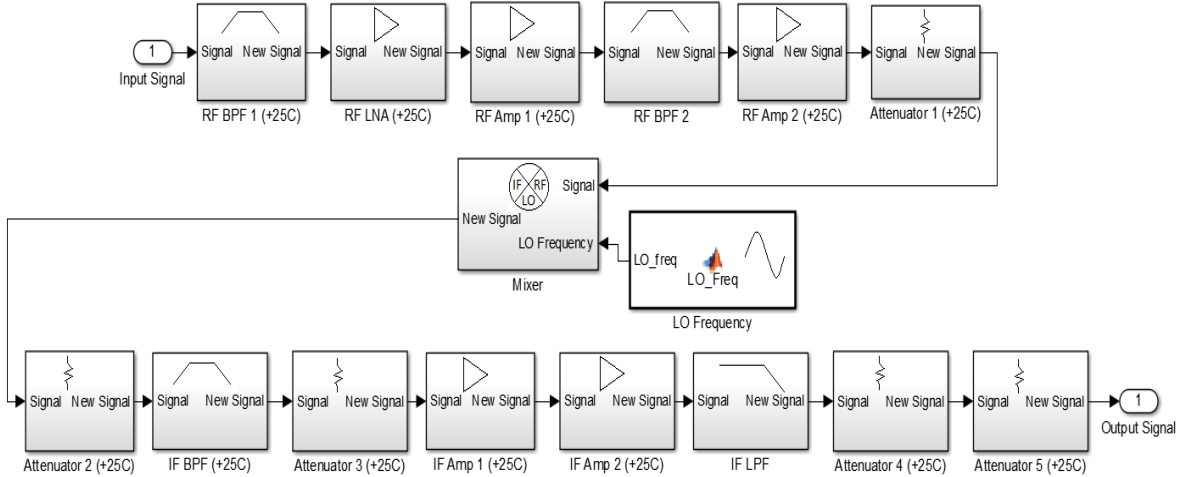


*Figure 17: Simulink receiver model simulated at +25 °C. Each block is a subsystem describing the gain or loss of one component in the receiver chain. Block names that do not specify temperature indicate that the corresponding component was assumed constant in performance across temperature.*

The output of the receiver model was input to a graphing function which plotted the gain over the frequency range for room temperature and the operating temperature limits of -40 °C and +85 °C, as well as across this temperature range at select frequencies. The model was also graphed against our hardware test measurements for the test conditions discussed in Section 3.3

### 3.5 Simulation and Hardware Test Results

Through a Matlab and Simulink implementation of cascading a chain of receiver components and analyzing their behavior over common frequency and temperature ranges, a model of our hardware receiver was simulated for various operating conditions, including some that we could not produce experimentally. The results of the simulation provide a level of insight as to how a single-conversion superheterodyne receiver operating in S-band may respond with varying frequencies and temperatures. The results are evaluated and a margin of error established where applicable through a comparison to measurements taken on the physical test hardware.



### 3.5.1 Model Results

To analyze the model's general performance, its gain at three operating temperatures, -40 °C, +25 °C, and +85 °C, was analyzed over a range of S-band frequencies. Though most components were guaranteed proper operation at -55 °C, a few could operate safely only at a lower limit of -40 °C, therefore setting the lower temperature bound of the receiver model. Below this limit, the receiver cannot be expected to perform as intended because of potential damage to any of these devices. Figure 18 displays the model's gain performance versus frequency for each of the three operating temperatures. The curves are defined over a 45 MHz region approximately in the center of the S-band. Because of the high selectivity of the receiver's bandpass filters, the model exhibits positive gain only in an approximately 6 MHz portion of the 45 MHz sweep. Once the signal frequency goes beyond the cut-off points of the receiver's filters, a sharp drop in gain occurs and causes a net attenuation for the system rather than a gain. Figure 19 provides a closer view of the in-band gain response of the receiver model.

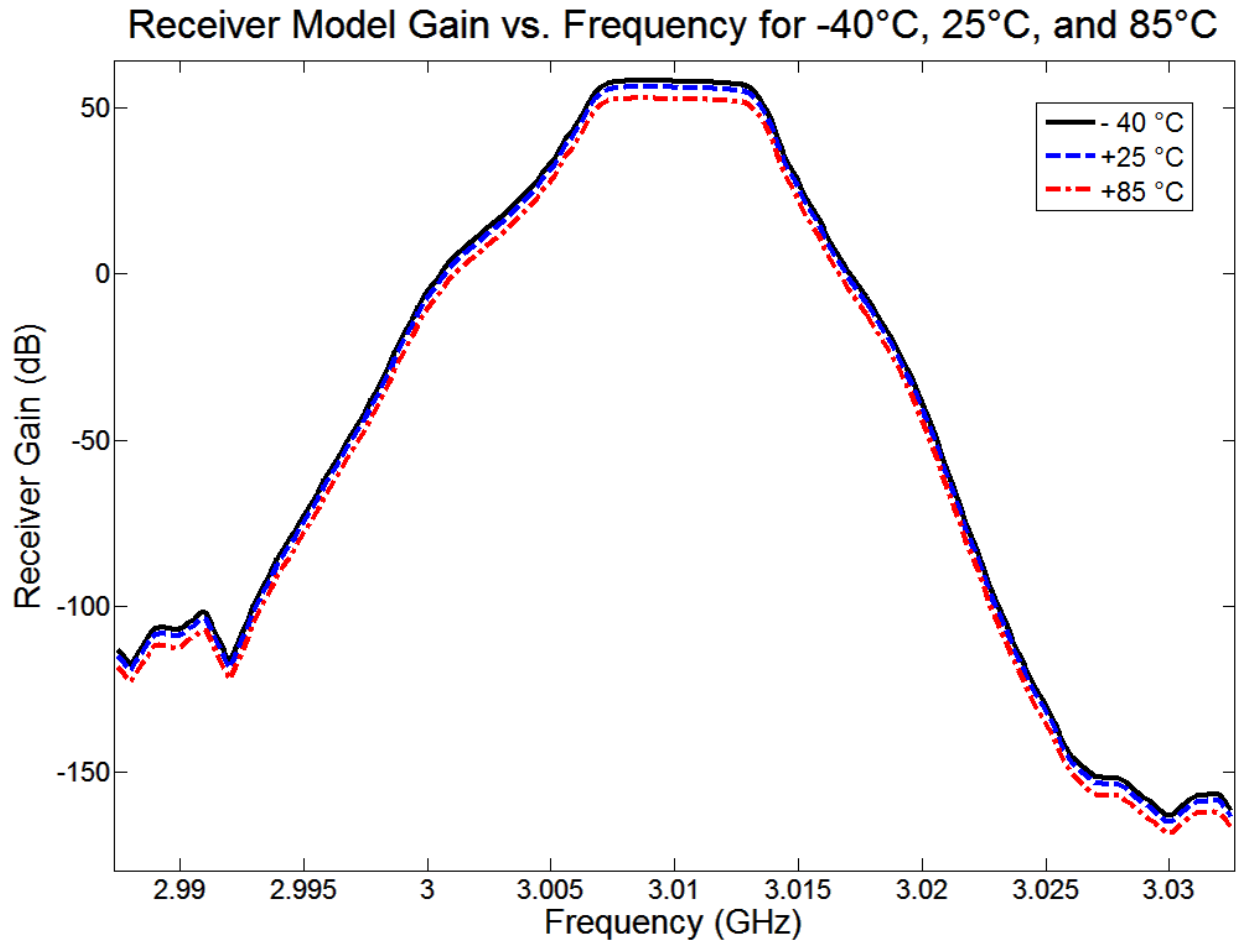


Figure 18: Receiver model's gain performance over a 45 MHz frequency span at -40 °C, +25 °C, and +85 °C operating temperatures. Receiver gain decreases quickly outside a relatively small band due to highly selective RF and IF bandpass filters.

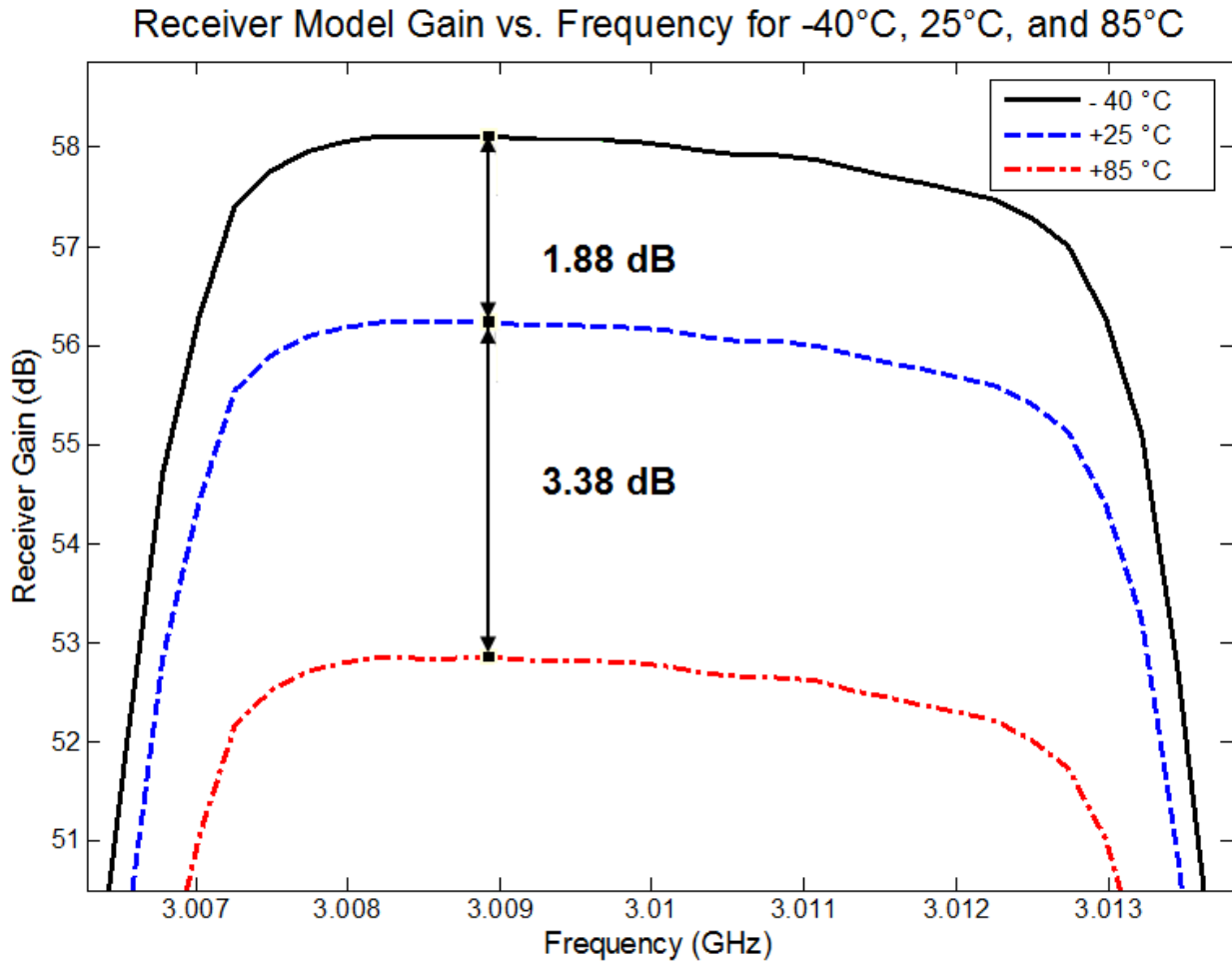


Figure 19: Focused view of Figure 18 receiver model's gain performance in-band at -40 °C, +25 °C, and +85 °C operating temperatures. Receiver gain decreases with increasing temperature. Gain decreases slightly with increasing frequency in-band.

A general decrease of approximately 0.56 dB (a 12.1% decrease) occurs for increasing frequency from 3.008214 GHz to 3.012024 GHz for a given temperature within -40 °C to +85 °C. At the edges of the passband, approximately 3.007 GHz and 3.013 GHz, gain decreases between 1.65 to 1.78 dB (32.62% decrease on average) from the average gain within 3.008214 GHz to 3.012024 GHz. For any given frequency, the model predicts a drop in receiver gain for increasing temperature across both in-band and out-of-band frequencies. As shown in Figure 19, in-band gain decreases on average about 1.88 dB from -40 °C to +25 °C and about 3.39 dB

from +25 °C to +85 °C (thus approximately 5.26 dB across the entire temperature range). This change in gain across the full temperature range corresponds to a 70.21% decrease.

To visualize the general effect of changing temperature from -40 °C to +85 °C on receiver gain at a constant signal frequency, one in-band frequency and two on either edge of the passband were chosen at which to plot this temperature range. While the trends seen in Figure 20 are equally discernible from Figure 19 with some inspection, Figure 20 more readily displays the receiver model's gain at an arbitrary temperature between -40 °C and +85 °C for any of the three frequencies specified. The average decrease in gain for the selected frequencies of Figure 20 is 0.03 dB/°C from -40 °C to +25 °C and 0.06 dB/°C from +25 °C to +85 °C.

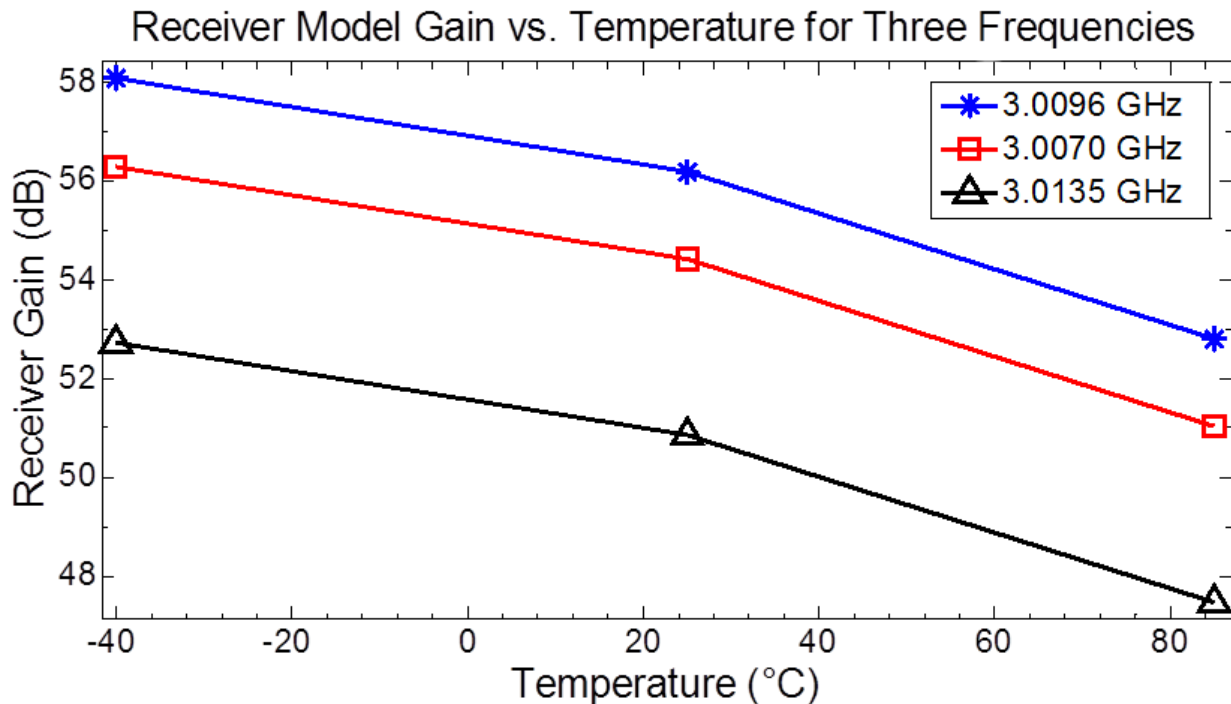
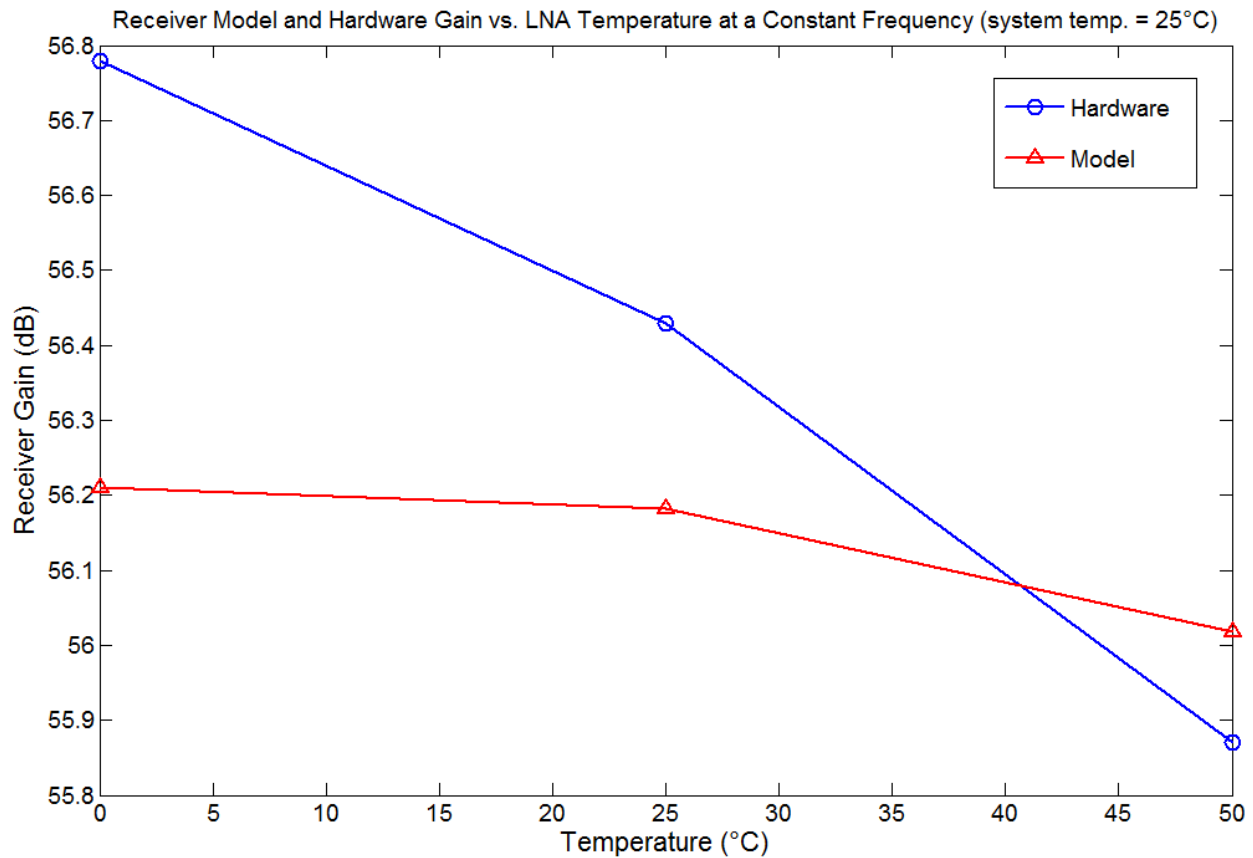


Figure 20: Receiver model gain vs. temperature. Each curve corresponds to a specific frequency either in-band or at one of the edges of the passband. Temperature points are plotted for -40 °C, +25 °C and +85 °C and linearly connected (-40 °C was interpolated from -55 °C and +25 °C for most components).

### 3.5.2 Simulation Model and Hardware Test Comparison

As discussed in Section 3.3 we measured our hardware receiver's gain at LNA temperatures of +25 °C and +50 °C across its band of operation in 1 MHz steps (as well as 0 °C for one frequency) to compare with the model's simulation of changing LNA temperature. For these test and simulation scenarios, all other hardware and model components remained at +25 °C. The results of this comparison are displayed in Figure 21 and Figure 22, highlighting respectively the gains of the hardware and model across LNA temperature for a fixed frequency and across frequency for two fixed LNA temperatures. The temperatures at which we measured gain were the best achievable extremes given our test equipment and procedure.



*Figure 21: Gain versus LNA temperature for receiver model and hardware setup at a constant frequency of 3.010 GHz. For both model and hardware, only temperature of the LNA was varied, with the system temperature kept at +25 °C.*

Figure 21 reveals a flatter change in gain by the model, 0.19 dB, between temperature extremes as compared to the hardware's response, a change of 0.91 dB. However, the model yielded lower gains by about 0.6 dB or less at 0 °C and +25 °C LNA temperatures compared to those produced from the hardware. With the LNA at +50 °C, the model gain exceeded that of the hardware by about 0.15 dB. However, since components near the LNA likely increased in temperature during heating of the LNA, our hardware gain measurement is lower than would be observed if the LNA was truly the only component changed in temperature, as is the case in the model. Figure 22 juxtaposes hardware and model gains at LNA temperatures of +25 °C and +50 °C for a sweep over the hardware's frequency band of operation in 1 MHz steps. Because the hardware's bandpass filters are highly selective, the range of operation spans only 6 MHz.

Receiver Model and Hardware Gain vs. Frequency for LNA temperatures of 25°C and 50°C (system temp. = 25°C)

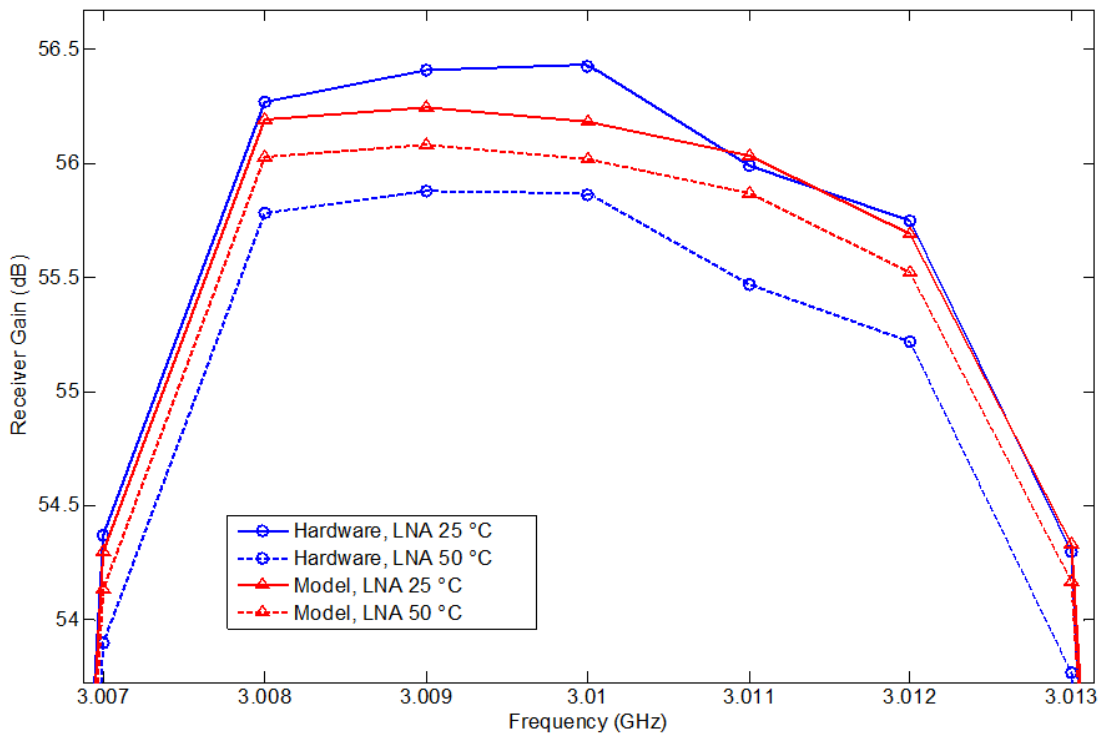


Figure 22: Model and hardware gain across the hardware's frequency band of operation for LNA temperatures of +25 °C and +50 °C.

At +25 °C, our model matches the hardware measurements to within 0.3 dB. On average the model is 0.1 dB lower than the measurements. The model's gain at +50 °C was consistently

higher on average than the gain of the hardware by 0.41 dB. The hardware showed a larger difference in its gain of 0.52 dB on average between the two test temperatures while the model only had an average gain displacement of 0.16 dB between temperatures. This greater variability in the hardware tests may again be a result of nearby components increasing in temperature during heating of the LNA. As a whole, our model simulation results matched the response observed in our hardware test measurements to within 1 dB or less, yielding very similar trends in gain for varying frequencies and temperatures.

## **Chapter 4: Radar Receiver Calibration Tool**

The receiver calibration application is our main deliverable for Group 108. Developed using the Qt GUI framework for C++, the application enables the user to import recording files and enter parameters intuitively, after which it displays a gain plot and computes the calibration factor and other metrics.

### **4.1 Methods**

Our calibration tool simplifies the radar receiver calibration procedure outlined in Chapter 2: To perform the calibration process, a radar operator connects a signal generator or other known source to the input of a receiver, bypassing the antenna, and records the output from the receiver using a real-time server with an ADC for data acquisition, in the same manner by which real mission data are recorded. During this calibration procedure, the radar's transmitter is not used, and can in fact be turned off. The operator makes several distinct recordings, stepping the input power into the receiver from below the expected noise floor up to a level past the expected 1 dB compression point of the receiver. The data from each recording is stored in a ROSA II file and the known input power levels that correspond to each file are written in a log. Once data recording is complete, the operator runs the receiver calibration application using the recording files, and the application displays the gain of the receiver and other measures such as the 1 dB compression point and the noise floor level. The application also displays a plot of the gain over the dynamic range of the receiver. Automating the calibration replaces manual calculation and eliminates the need for acquiring manual measurements of the receiver output power using a signal analyzer or other instrumentation.

#### **4.1.1 Program Function and User Interface**

With the high level requirements of the application laid out, we began the development process by detailing the operation and user interface of the software. The flowchart in Figure 23 below shows the overall operation of the program.



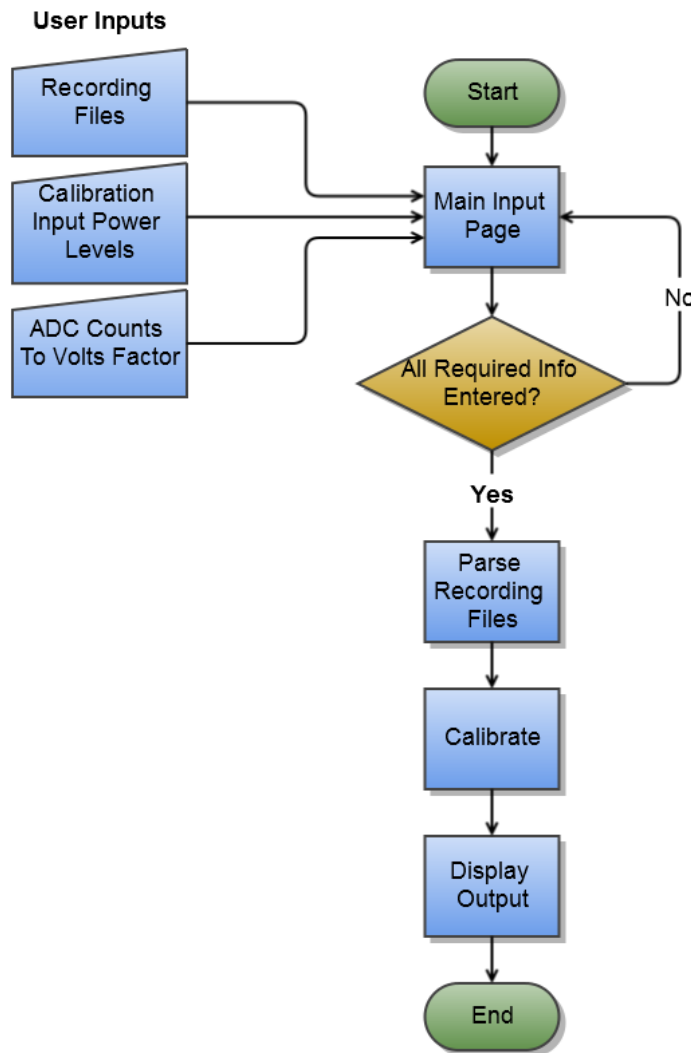


*Figure 23: High-level functionality of radar calibration toolkit.*

When the program starts, the main window is displayed, showing buttons and forms for user input. The conceptual design for this screen is shown in Figure 24. There are three main items of user input necessary for calibration. First, the application needs the file system paths to the analyst’s ROSA II recording files, which contain the waveform data taken for each power level step in the calibration procedure. Second, the user needs to enter the corresponding input power level to the receiver corresponding to each recording file. Third, the user must input the count to Volts conversion factor for the analog-to-digital converter in the real-time server used for recording. Since different ADCs have different resolutions and ranges, different recorded

ADC values correspond to different voltage levels. Thus, an ADC count conversion factor is necessary for gain calibration. We determined the best method to obtain these user inputs would be one main page displaying a list of files with their corresponding input power levels and a form to enter ADC counts per volt. The page has an intuitive interface for entering the necessary user input.

The screenshot shows a software interface for ADC calibration. At the top right, there is a label "ADC Counts per Volt" next to a text input field containing the value "32768". On the left side, there are two buttons: "Add File" and "Remove File". In the center, there is a table with two columns: "File Name" and "Input Power(dBm)". The table contains three rows: "File1" with "-60", "File2" with "-55", and a row with "....." in both columns. At the bottom right, there is a "Calibrate" button.

File Name	Input Power(dBm)
File1	-60
File2	-55
.....	.....

Figure 24: Design of main user input screen.

After all the required information is entered, the application reads the data and performs the calibration algorithm, and the output is displayed to the user on a new screen, the conceptual layout of which is shown in Figure 25. This screen shows numeric values of the measurements as well as a gain plot with data points corresponding to each input power level.

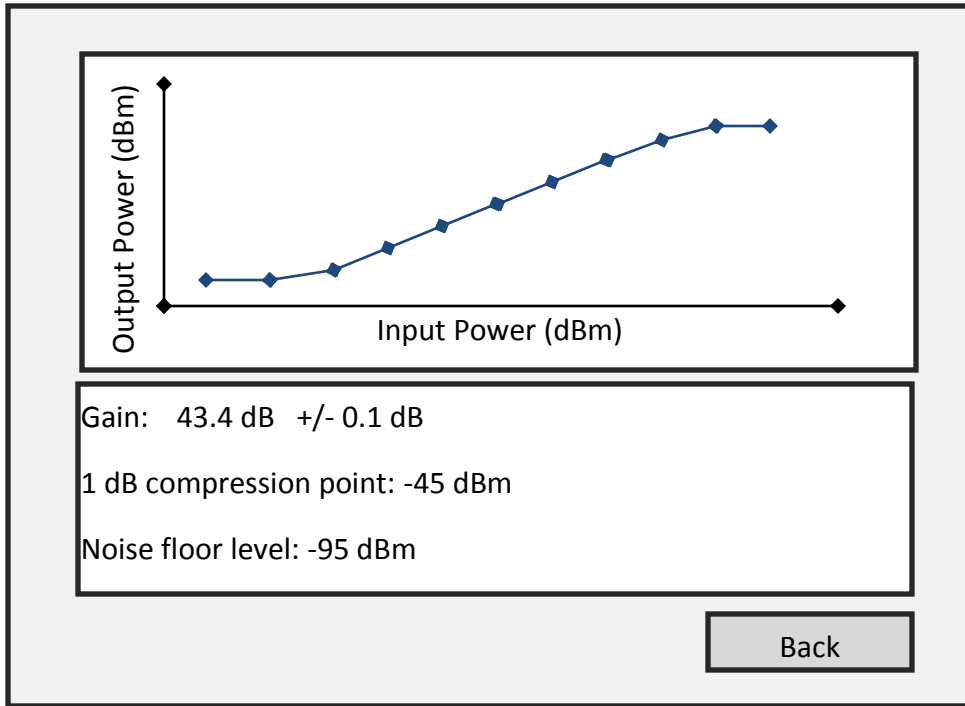


*Figure 25: Design of calibration output screen.*

#### 4.1.2 Algorithms

Once the user interface was conceptually designed, the next step was to design the algorithms for parsing recording files and performing calibration.

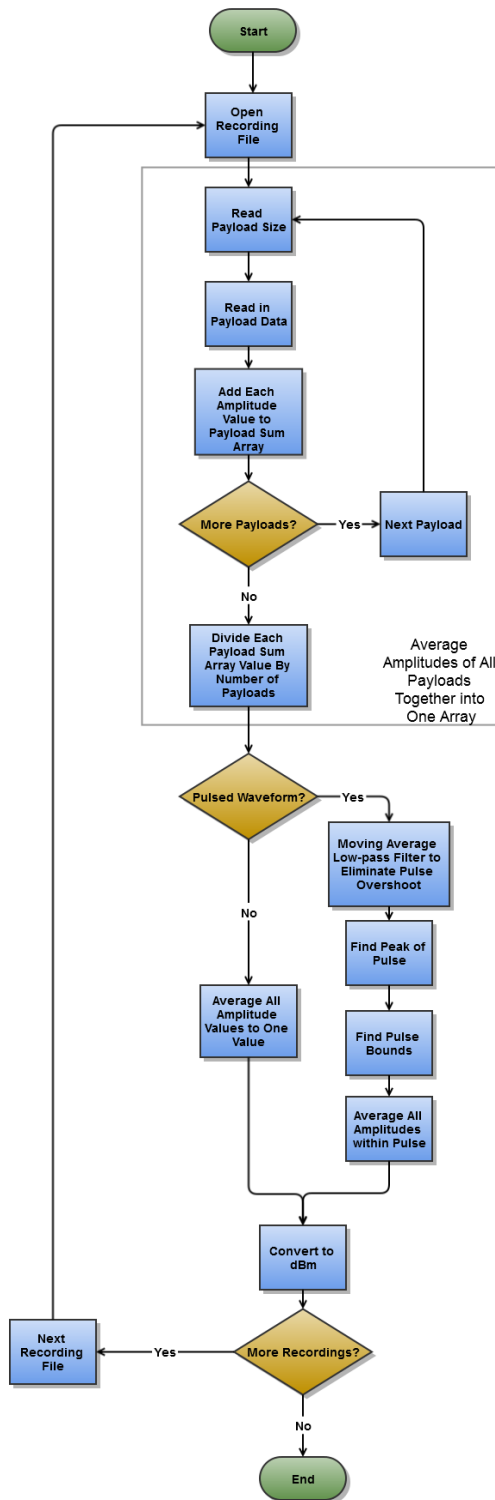


Figure 26: Flowchart of algorithm for parsing recording files and obtaining output power levels.

The algorithm for extracting output power levels from the recording files is shown in the flowchart in Figure 26. The algorithm first opens a file, computes the amplitudes of each sample within the payload, and ensemble averages all of the payload amplitudes together into one time vector. The amplitude of each sample can be calculated from the I/Q data using Equation 7. The ensemble average vector will be the same size as one payload but will be a more accurate representation of the amplitude content of the signal, since it is averaged over multiple payloads. A coherent averaging method, in which the waveforms of each payload would be averaged rather than just the amplitudes, is not used because the recording payloads are not synchronized with the signal.

$$A_{ADC} = \sqrt{I^2 + Q^2}$$

*Equation 7: Equation for amplitude calculation from I and Q data*

Once the ensemble average vector is computed, the program calculates output power depending on whether the signal is pulsed waveform or continuous waveform (CW). In the case of CW calibration, the output power is simply the mean of the ensemble average vector converted to dBm. For pulsed calibration, the output power is computed from the mean of the amplitude values within the range of indexes where the pulse occurs. To find the pulse location, the program first applies a basic mid-point moving average low-pass filter to eliminate overshoot at the beginning of the pulse, which is not a correct measure of pulse amplitude. We found that a 15-point moving average was sufficient to eliminate the overshoot. The index of the maximum value of the filtered vector is then known to be within the pulse, and the program finds the start and end bounds of the pulse based on that value. To do so, the program iterates forwards through the vector until it finds a value less than a threshold value, set as 95% of the maximum value. This point is defined as the maximum index of the pulse. The minimum index is defined the same way, but iterating backwards through the vector. The mean of all amplitudes within this pulse window is computed and converted to dBm, yielding output power. Conversion to dBm uses the formula in Equation 8. The output power level for each recording is computed and stored with its corresponding input power.

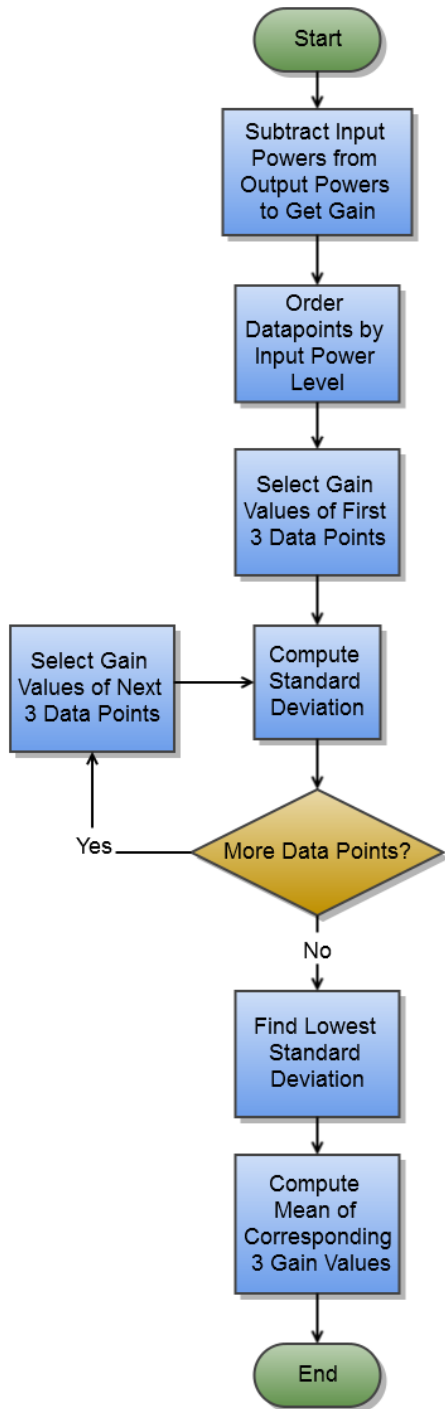
$$P_{out(dBm)} = 10 \log_{10} \left( \frac{V_{rms}^2 / 50 \Omega}{.001 W} \right)$$

$$V_{rms} = \frac{A_{ADC}}{d * \sqrt{2}}$$

where  $d$  = ADC counts per volt

$$P_{out(dBm)} = 10 \log_{10} \left( \frac{(A_{ADC})^2}{d^2 * 0.1} \right)$$

*Equation 8: Receiver output power in dBm calculated from recorded amplitude.*



### Example

Input(dBm)	-60	-50	-40	-30	-20
Output(dBm)	-42	-30.2	-20	-9.8	1
Gain (dB)	18	19.8	20	20.2	21

Moving Window Standard Deviation:

Input(dBm)	-60	-50	-40	-30	-20
Gain (dB)	18	19.8	20	20.1	21

Std Dev: **1.10**

Input(dBm)	-60	-50	-40	-30	-20
Gain (dB)	18	19.8	20	20.1	21

Std Dev: 1.10 **0.15**

Input(dBm)	-60	-50	-40	-30	-20
Gain (dB)	18	19.8	20	20.1	21

Std Dev: 1.10 0.15 **0.55**

Std Dev: 1.10 > **0.15** < 0.55

$$G = \frac{19.8 + 20 + 20.1}{3} = 19.97 \text{ dB}$$

Figure 27: Flowchart of algorithm for calculating overall receiver gain with example values for demonstration.

After the output power levels for each recording are computed, the program must compute the calibration factor, or nominal gain of the receiver in the linear region. Figure 27 shows the algorithm for this computation as well as an example data set, which is also plotted below in Figure 28.

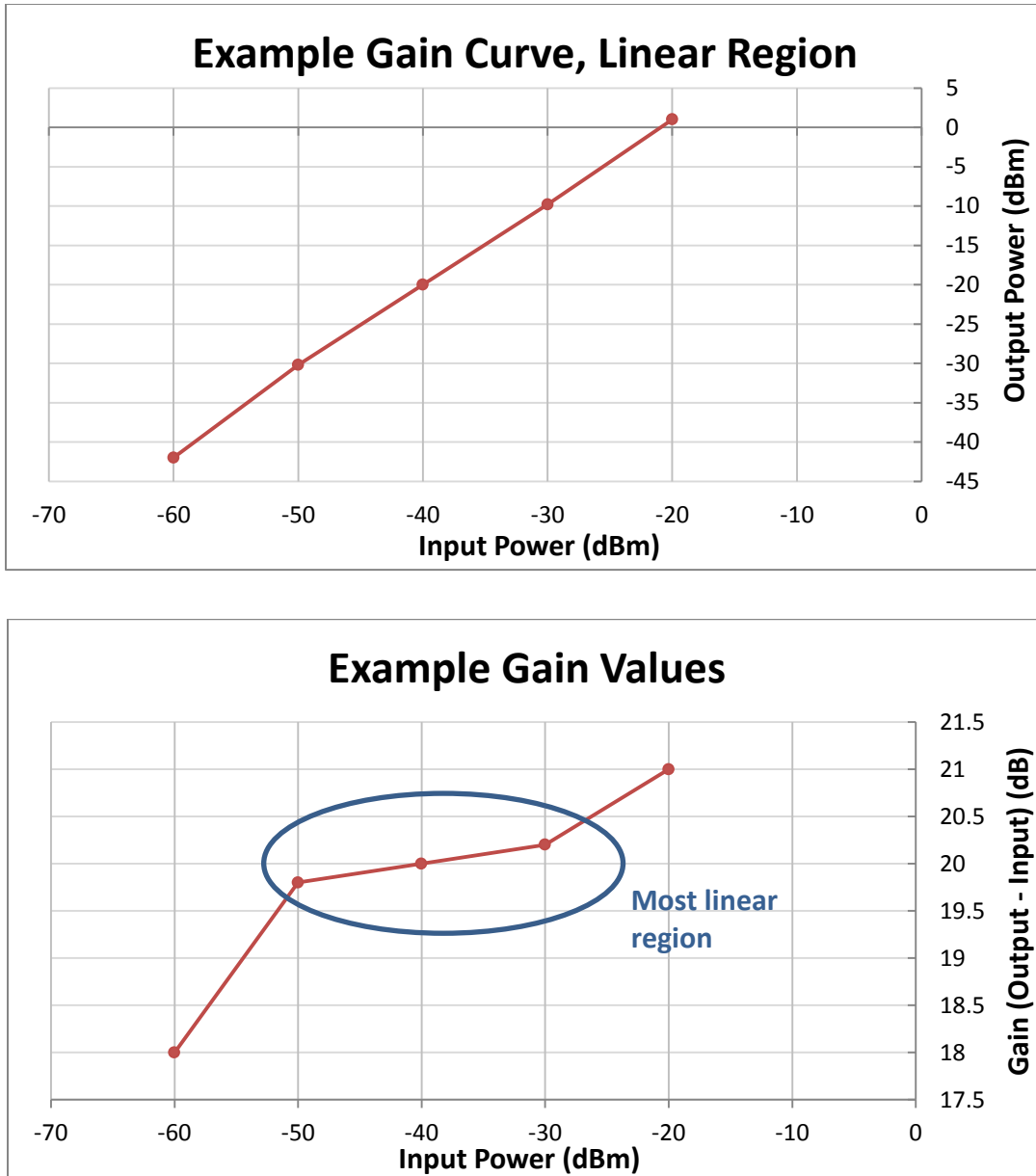


Figure 28: Plots of example data from Figure 27.

The program subtracts each input power from its corresponding output power to obtain gain values corresponding to each input power. Then, the program uses a sliding window



method (sliding across the successive input power levels) to compute standard deviations of consecutive gain values. For each group of three consecutive input power levels, the sample standard deviation of the three gain values is computed. The lowest resulting standard deviation indicates the most linear portion of the gain curve, and the average of the three corresponding gain values is used as the gain of the receiver in the linear region. The sliding window size of three is appropriate, but somewhat arbitrary; the sliding window could be increased to average a larger number of gain values. A large window size runs the risk of exceeding the linear region of the amplifier, and using only two values may not accurately represent the gain over the whole linear region.

The 1 dB compression point of the receiver is next computed by finding the calibration data points that are closest to the point beyond the linear region where the gain is 1 dB less than the computed calibration factor – in other words, the point at which the output power is 1 dB less than what would be found from a straight-line extrapolation of the linear region. Using these points, the 1 dB compression point is computed by a linear interpolation shown in Equation 9 and Figure 29. Interpolating between measured data points produces a more accurate estimate than choosing the closest data point to the 1 dB compression point.

$$m = (y_B - y_A)/(x_B - x_A)$$

Where  $(x_A, y_A)$  and  $(x_b, y_b)$  are the two points from which to interpolate

$$x_{1dB} = x_A + (y_{1dB} - y_A)/m$$

Where  $y_{1dB} = \text{calibration factor} - 1$

$$x_{1dB} = x_A + \frac{(y_{1dB} - y_A)(x_B - x_A)}{(y_B - y_A)}$$

*Equation 9: Formula for linear interpolation of 1 dB compression point.*

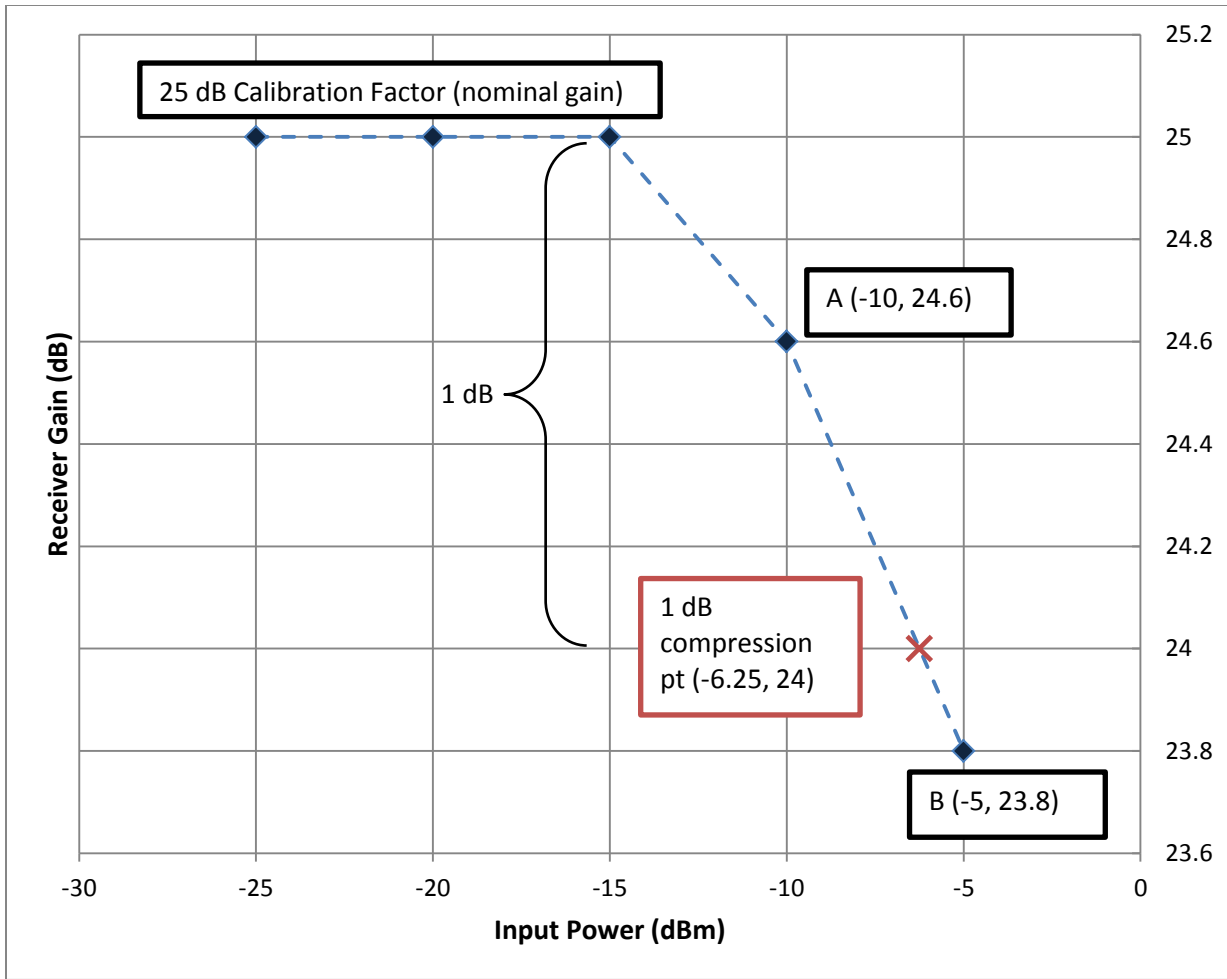


Figure 29: Plot showing interpolation of 1 dB compression point as described in Equation 9.

#### 4.1.3 Development Process

In developing the receiver calibration application, we utilized Apache Subversion for version control, and our repository was stored in Group 108's GForge server, their standard for storing and managing source code. We committed our changes as often as possible to ease collaboration. We met weekly with the Post-Mission Analysis (PMA) development team and integrated our latest version of the cal tool weekly with PMA to ensure that there were no integration issues at the end of our project.

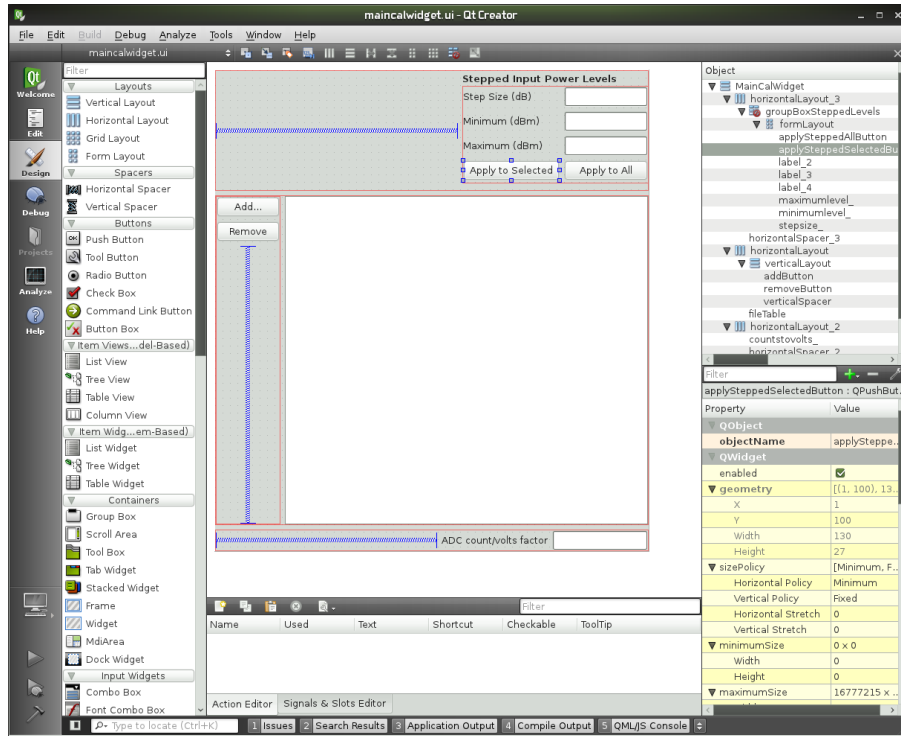
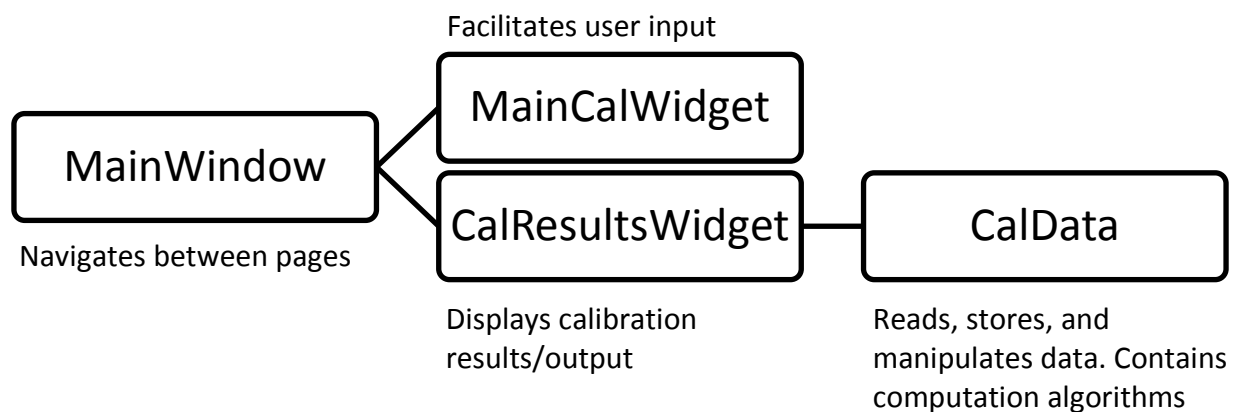


Figure 30: Screenshot of Qt Creator's form editor utility.

Initial layout of the user interface was done using Qt Creator's Form Editor, which auto-generates Qt XML files from a user-friendly GUI that enables dragging, dropping, and resizing of form elements. Figure 30 shows a screenshot of the user input form we developed using Qt Creator. Designing the forms in this way saved a lot of time in comparison to manually typing XML or C++ files. Fine editing of the UI was performed in the XML files.

Since ROSA II recording files are used by the calibration tool, there are pre-existing reader classes from Post-Mission Analysis (PMA) and other ROSA II software that we utilized in our code. Using these classes saved us from doing unnecessary work. In addition, we incorporated a third party tool for generating plots in Qt called QCustomPlot. This software is free under the GNU General Public License.



*Figure 31: Class diagram showing relationships between user interface classes.*

Since the application is GUI-based, much of the code is contained in user interface classes. The class diagram in Figure 31 shows the relationship and function of each class. MainWindow, MainCalWidget, CalResultsWidget inherit from Qt user interface classes, enabling the code that we developed to easily interact with user actions. CalData is an independent class that is used for storing and manipulating the input information and the data read from the recording files. All of the algorithms for file parsing and calibration computation are contained in CalData. To assist with the physical reading of recording files, CalData uses pre-existing reader classes developed by Group 108 software engineers, though we modified these classes for our specific needs. The C++ code developed is readable and well-commented so that it can be understood by other software developers. In addition, it was designed to be as modular as possible to facilitate future improvement or modification.

#### 4.1.4 Testing

To ensure that the calibration tool results are accurate and reliable, several tests were performed. To record data, we used a real-time server with a Pentek analog-to-digital converter. The first test of the calibration tool was performed using recordings of signal generator output alone. A diagram of the test setup is shown in Figure 32.

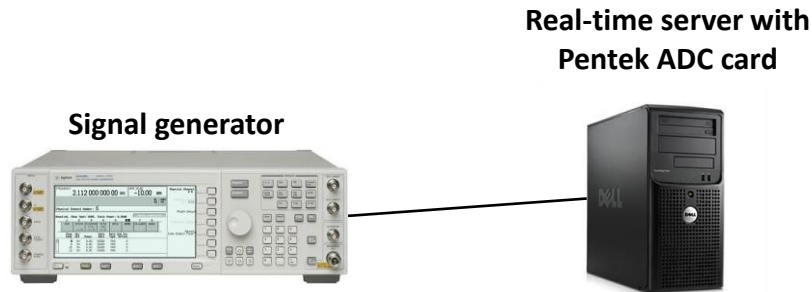


*Figure 32: Configuration of signal generator recording test setup.*

The signal generator was connected to the Pentek ADC using a standard SMA cable and a SMA/SMC adaptor cable, since the ADC input ports are SMC connectors, which are smaller. The signal is sampled by the ADC at 200 MHz (with 16 bit resolution), digitally downconverted in frequency, and recorded using the real-time server. The real-time server is a computer running Linux that has the ROSA software suite installed, used for recording, viewing, and playing back data from ROSA systems. The signal generator power was incremented from -130 dBm to 0 dBm, in 10 dB steps, outputting a 30 MHz CW tone. This initial test was done to verify that the calibration tool could accurately calculate power, by comparing the calibration tool results with the signal generator power setting used.

Thorough testing of the receiver calibration toolkit required using hardware similar to actual receiver configurations in the field. For our test setup, we used an S-Band radar receiver with two signal generators. This is the same receiver that was modeled in Simulink, as described in Chapter 3: A diagram of this setup is shown in Figure 33.

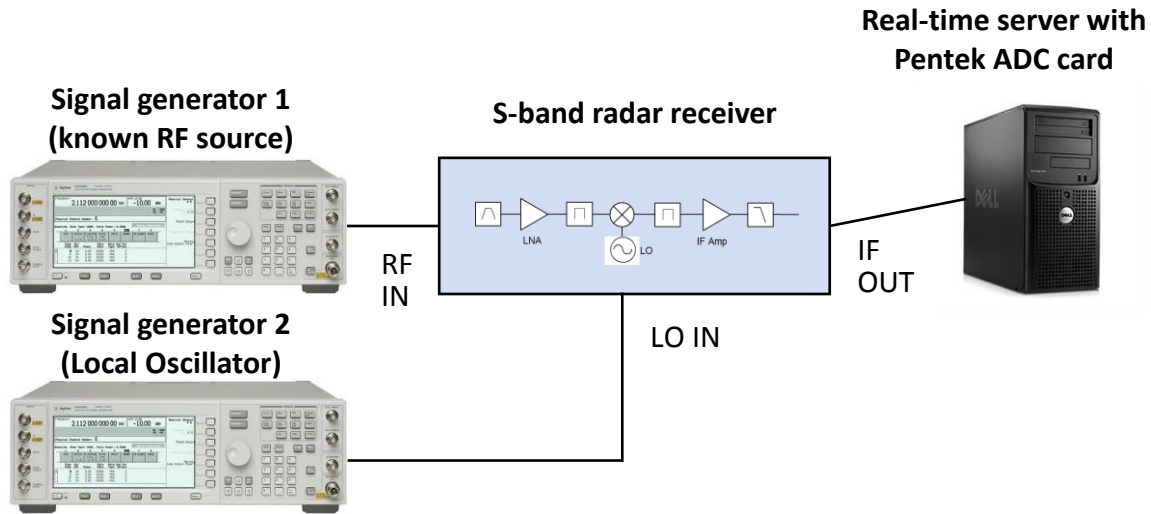


Figure 33: Diagram of test hardware configuration.

Signal generator 1 is used as the known test source for radio frequency input into the receiver. It can be configured to produce a continuous waveform or a pulsed waveform with variable pulse width and pulse repetition frequency. The power output of this signal generator was stepped for each recording in the calibration procedure. Signal generator 2 is used to generate the local oscillator (LO) signal that mixes the RF down to the intermediate frequency (IF). This input signal was necessary because the receiver did not contain an internal LO. The LO power is specified at 21.75 dBm in the receiver schematic, so the signal generator was set to that level. Such a high LO power level is necessary to ensure the desired IF signal contains a significant amount of power with respect to spurious signals. The IF output of the receiver is connected to the Pentek ADC using the same configuration as does the signal generator test.

The procedure for taking receiver test data was essentially the same procedure an operator would use in the field to calibrate a radar receiver. Stepping the input power from -130 dBm to -10 dBm in 10 dB increments, we took one-second long recordings of the receiver output signals. We recorded multiple sets of calibration data, varying the receiver attenuation, and the input signal type. Two continuous waveform (CW) calibrations were performed with the IF variable attenuator set to 0 dB and 31 dB of attenuation. Adding attenuation enabled recording output signals with the receiver operating in the compression region; with 0 dB attenuation the output signal amplitude is higher than the ADC's full scale voltage. These calibrations were then

repeated using pulsed waveform input. To record CW signals, the software on the real-time server was configured to constantly sample the signal. The signal generator used to create the known input signal was set to continuous mode at the specific S-band frequency that the receiver is designed to receive. For pulsed signals, the software was configured to sample the signal in triggered mode, in which the software captures a payload starting when the trigger input of the ADC is high. The signal generator was set to pulsed mode, and the pulse trigger output of the signal generator was connected to the ADC trigger input to synchronize each payload within the recording to the pulsed signal. Synchronizing the recording with the signal ensures that the pulse occurs at the same time in each payload. The signal generator was configured to output an RF signal with pulse width of 300  $\mu\text{s}$  and a pulse repetition interval of 10 ms, and each pulse was delayed 600  $\mu\text{s}$  from the trigger, so that it would be somewhere in the middle of the payload.

We then ran the calibration toolkit on the test files and examined the output. Additionally, by performing the same calibration procedure with a signal analyzer connected to the receiver IF output instead of the real-time server, we made manual measurements of the output power levels and gain values. These manual measurements were then compared to the calibration tool output for verification purposes. Comparison with manual calculations also yielded the error margin of the calibration tool.

## 4.2 Results

The calibration toolkit released to Group 108 is a functional and robust application that can be utilized in the field or after the mission, as long as the recording files are present. The user interface of the tool is designed to let the analyst enter the required information quickly and easily. The main input screen is shown in Figure 34.

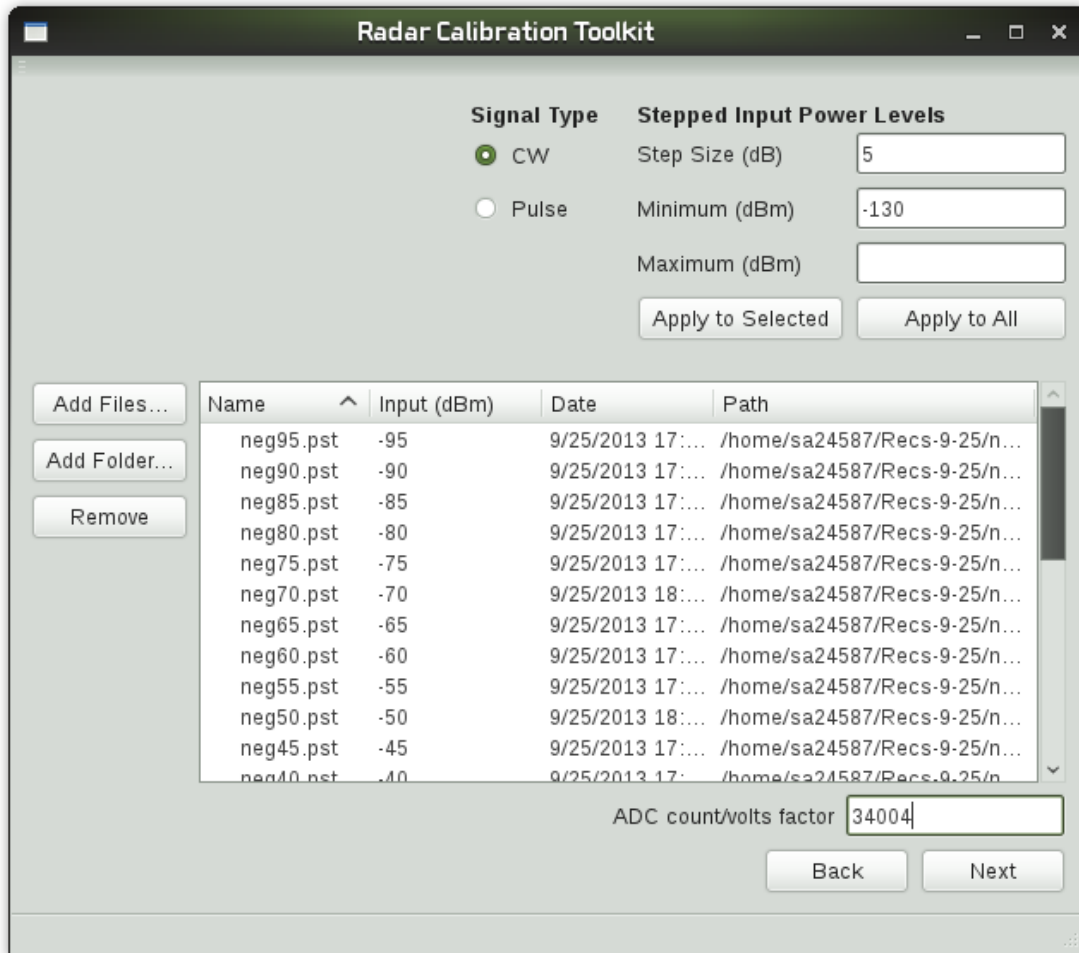


Figure 34: Screenshot of input screen showing the file table populated with calibration recording files.

On the main input screen, the user first adds recording files using the “Add Files...” button, which opens a standard dialog box for file selection. The selected files are then validated to ensure the contents of the files are not corrupted or invalid, and the file table box is populated



with information about the files. The validation routine checks if each file header and payload header has the correct contents, such as the 32-bit “magic number” that is repeated at the beginning of each header. Each recording’s input power, the second column in the table, must be entered by the user. The user can double click and type the value manually, or utilize the “Stepped Input Power Levels” form in the top right corner. This form allows the user to specify the step size of the recordings, the minimum power level, and the maximum power level, and the program will populate the input power list with the correct values. The user can opt to apply the stepped values to only the files that are currently selected, which is useful in case the set of files is missing a power level or if the operator varied the step size at a particular range of input levels. Also on this screen, the user can specify the ADC counts per volt factor as well as whether the input signal was continuous waveform or pulsed waveform. When the user presses the “Next” button, the tool runs the calibration algorithm discussed in the previous section, and the results screen is displayed as shown in Figure 35.

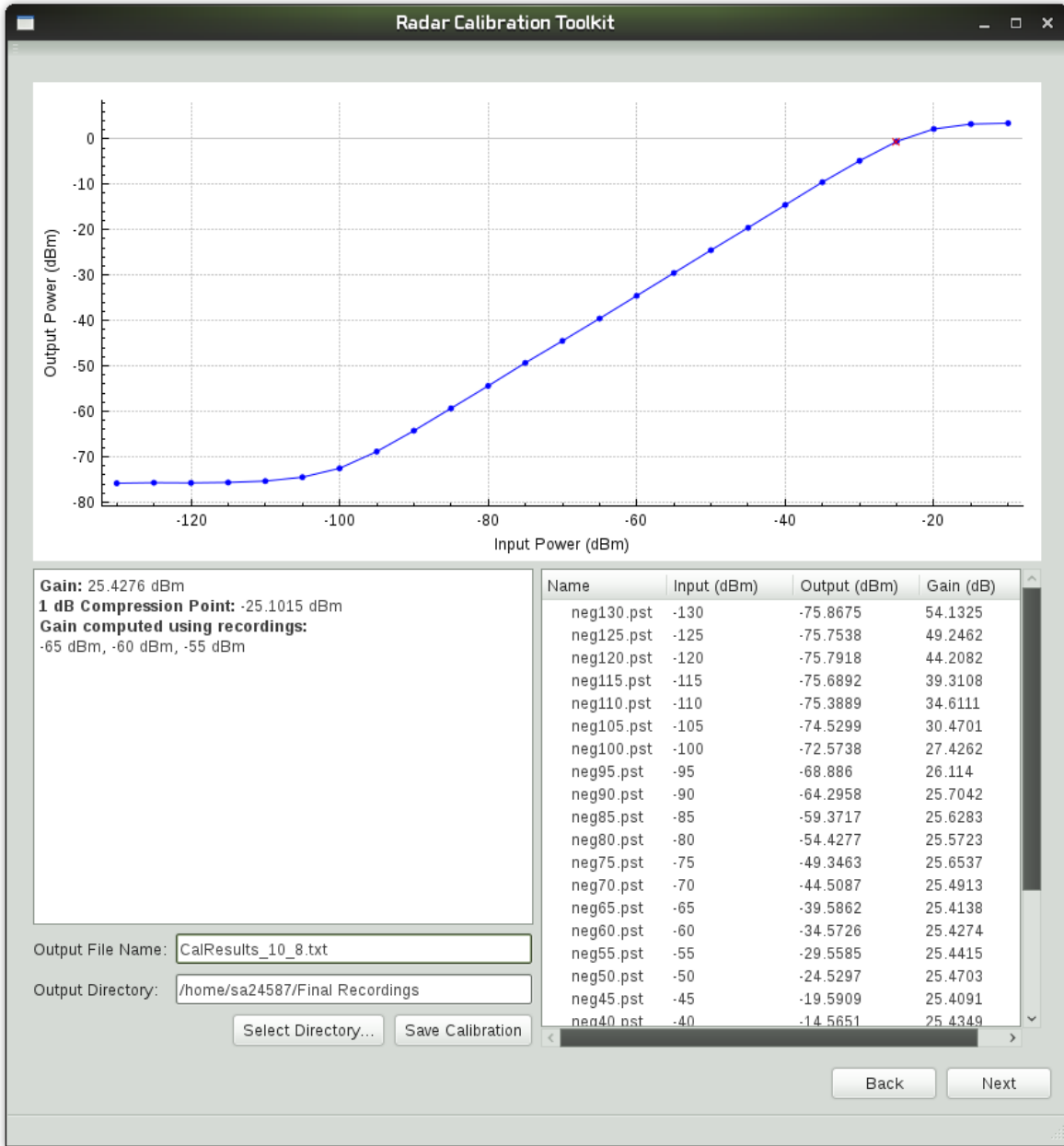
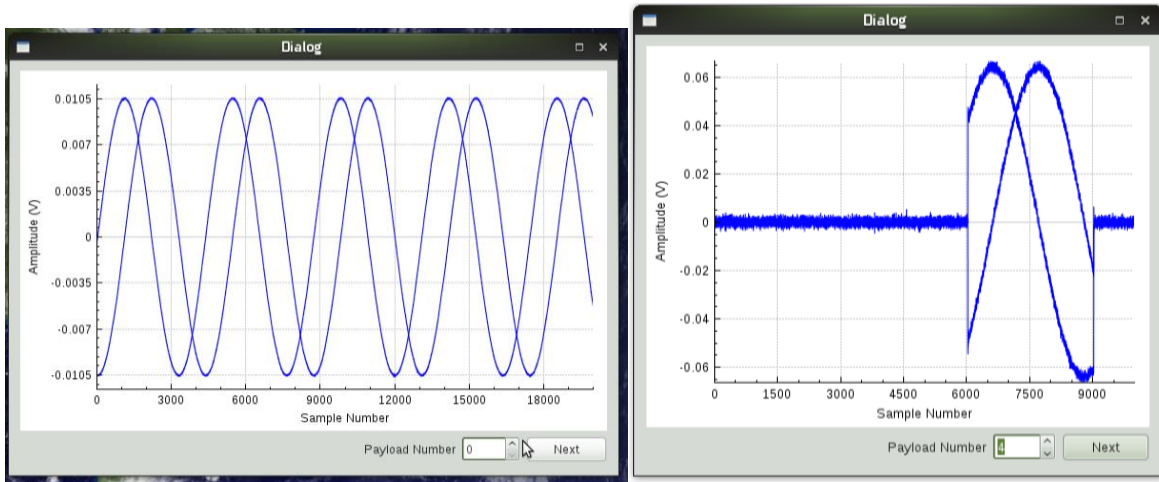


Figure 35: Screenshot of calibration results screen, showing gain curve and numeric data.

The results screen displays a plot of the receiver output power versus input power, in units of dBm. Radar operators and analysts are very familiar with this type of plot, and viewing it immediately after performing the calibration enables quick detection of problems with the receiver. The 1 dB compression point is plotted as a red X on the output power curve. Similar to the file list on the main input screen, the results screen shows a list of files with their

corresponding input power, computed output power, and computed gain value. The text browser on the bottom left displays the calibration factor (the nominal gain value in the linear region) and the 1 dB compression point. All of the calibration results displayed below the plot can be saved to a text file with a file name and location specified by the user, enabling access to the results after the program is closed.



*Figure 36: Screenshot of payload view screens showing continuous (left) and pulsed (right) waveforms.*

An additional feature of the results screen is the ability to view payload waveforms of each recording. Double clicking on a recording in the list displays a pop-up window with a plot of the raw I/Q waveforms contained in the first payload of the recording, shown in Figure 36. The user can step through the payloads or seek to a specific payload using the buttons below the plot. This utility is an extra feature not initially specified as a goal of the project, but we determined that it was a useful addition to the tool. Enabling the user to visualize the signal improves the value of the tool in diagnosing errors. For pulsed waveforms, this plot shows the user the range of samples within the payload at which the pulse occurs.

#### 4.2.1 Calibration Tool Performance

Initially, the calibration tool was tested with CW input from the signal generator to verify that the tool could accurately measure the power of a CW tone.

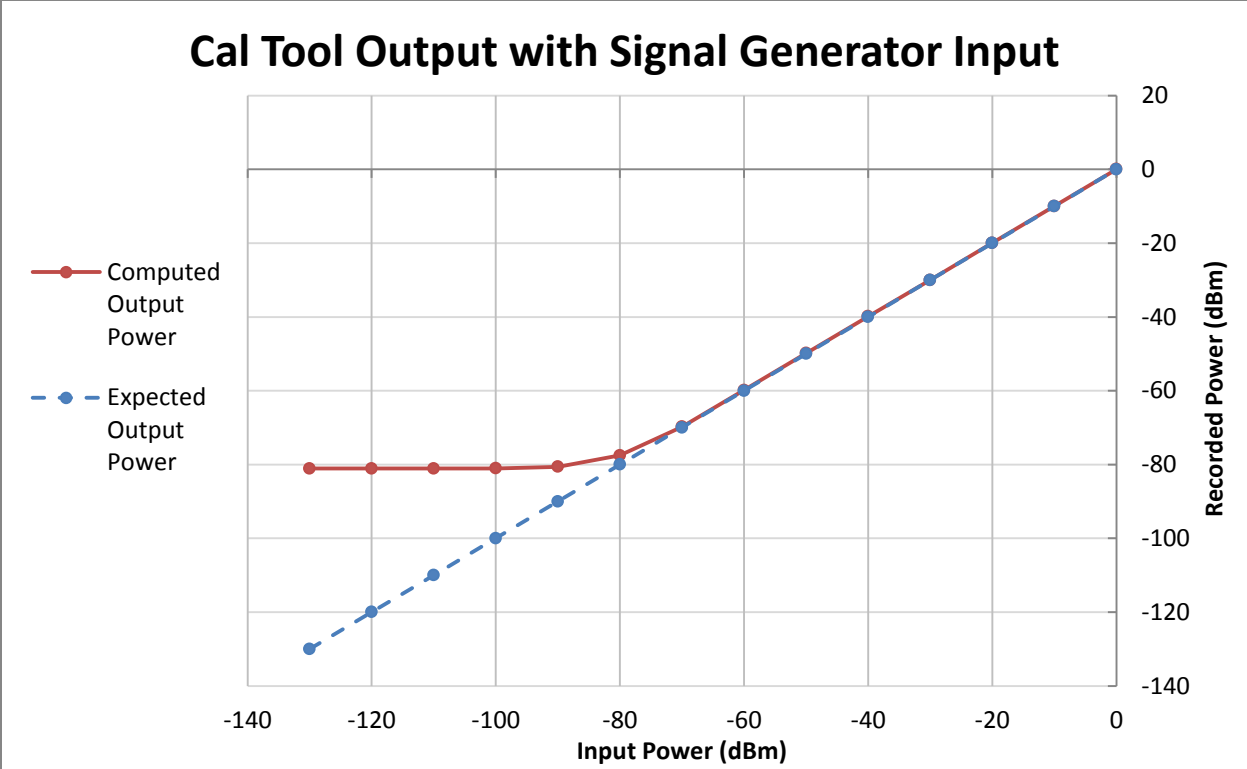


Figure 37: Computed power of signals from the signal generator directly connected to the ADC (solid line) and actual input power from the generator (dashed line).

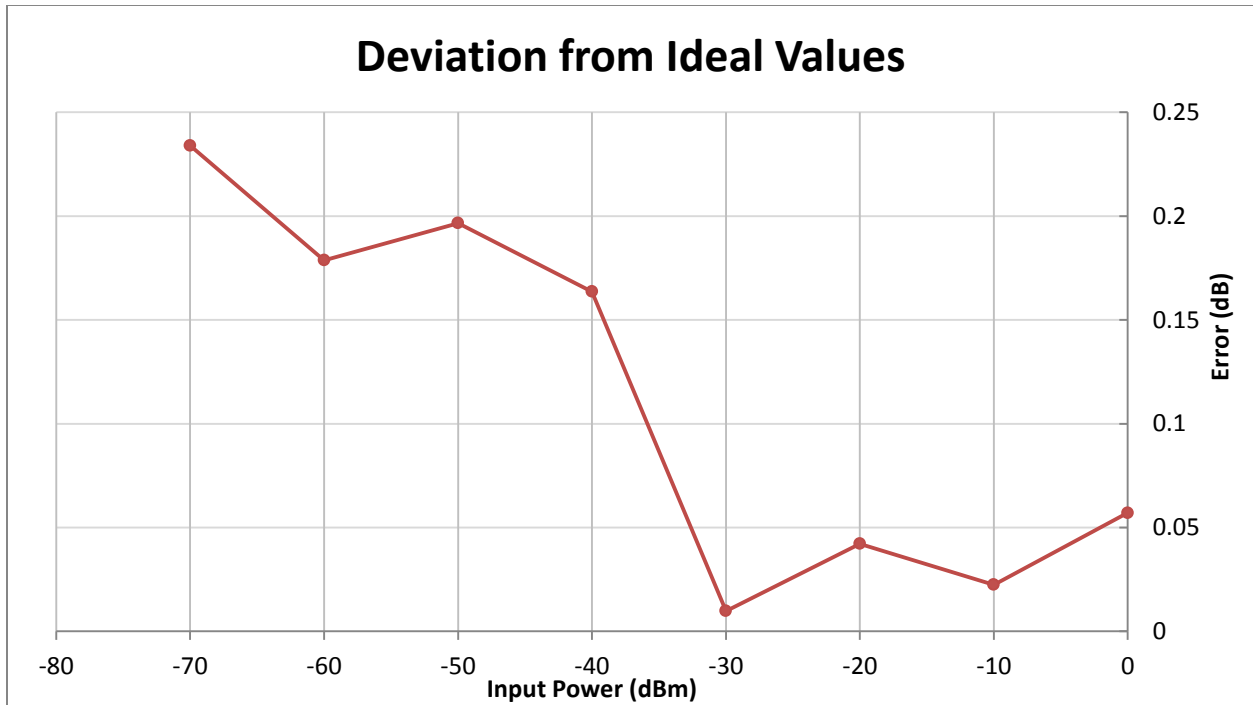


Figure 38: Plot of the difference between actual and expected ADC values. Results are shown for linear region, -70 dBm input and above.

Figure 37 shows that the calibration tool power computations are within 0.25 dB of the ideal values in the linear region, equivalent to 5.9% error in signal power. For power levels -30 to 0 dBm, the error is under 0.06 dB, equivalent to 1.4% error. Much of this error stems from nonlinearity in the ADC, which we deduced by verifying the accuracy of the signal generator. Using the signal analyzer, the signal generator output power was measured for each power setting, resulting in measurements that are within 0.05 dB of the signal generator power setting. This indicates that the ADC in our test setup was the major source of error. Also, Figure 37 and Figure 38 show that the calibration tool cannot measure power below -80 dBm, which is far above the noise floor of the signal generator. This limitation is because the power calculation is performed on the raw amplitudes of the signal, where the combined power of the noise at all frequencies obscures the signal power. Without filtering out the broadband noise or performing a frequency domain analysis, the calibration tool cannot measure power down to the true noise floor of the receiver. This limitation is revisited and ultimately resolved in Section 4.2.3

To test the calibration tool as it would be used in the field, we made four sets of calibration recordings using the receiver setup in the lab, which is temperature-controlled at 25 °C. The first set of recordings was taken using a CW input signal with the receiver functioning normally, without any added attenuation by the variable attenuator. The second set was taken with a pulsed waveform input signal. The third and fourth sets were taken the same way as the first and second sets, but with the variable attenuator set to 31 dB of attenuation. Each calibration stepped the input power by 10 dB for each recording.

		Cal #	Cal Factor (dB)
<b>0 dB IF Attenuation</b>	<b>CW</b>	1	56.1939
	<b>Pulsed</b>	2	56.1925
<b>31 dB IF Attenuation</b>	<b>CW</b>	3	25.2567
	<b>Pulsed</b>	4	25.2398

*Table 1: Calibration tool results from 4 different calibration setups.*

As expected, setting the variable attenuator to 31 dB attenuation lowers the gain by 31 dB  $\pm 0.06$  dB. In the first calibration listed in Table 1, the true gain of the receiver can be examined. However, without additional attenuation, we were unable to make recordings in the compression region of the receiver, since the output in that region exceeds the 8 dBm dynamic range of the ADC. A signal above 8 dBm causes the ADC to clip the peaks of the signal, making any gain calculation meaningless. In addition, signals well above 8 dBm can damage the ADC card. This problem is simply a limitation of our test setup as the ADC range is not the source of compression in field radars.

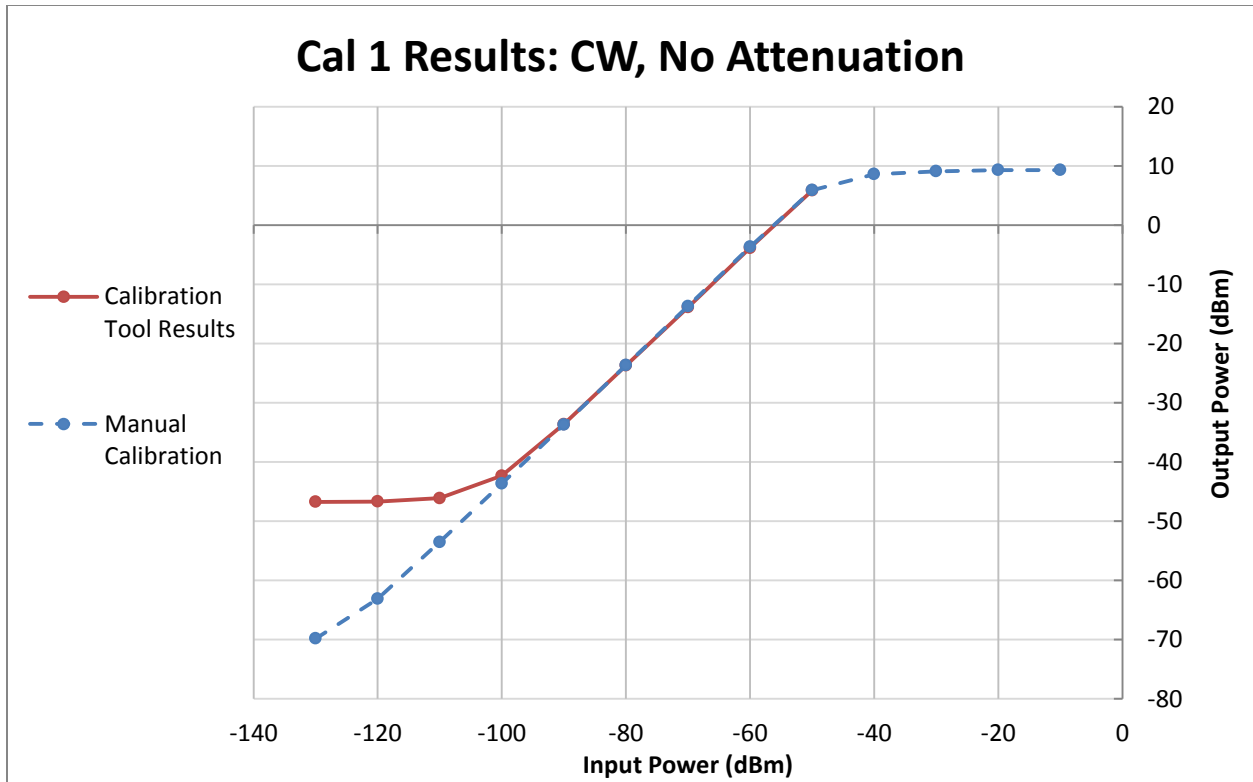


*Figure 39: Results from manual and computed calibration of test receiver with no added attenuation and a CW input signal.*

Figure 39 shows the gain curve produced by the calibration tool for the calibration listed in the first row of Table 1, plotted alongside manual measurements of the gain curve taken using a signal analyzer. The maximum input level of the calibration tool data is -50 dBm, since any higher input would result in an output level above the ADC's dynamic range. Similar to the signal generator test, the computed curve does not match the measured curve at lower input levels, where the noise power level is higher than the signal power level. The signal analyzer can determine the signal power at low power levels by measuring the power at a specific frequency, achieved by performing a discrete Fourier transform and measuring a specific frequency bin. The power level at that frequency is averaged over time to eliminate the effect of in-band noise. However, the calibration tool is quite accurate in the upper part of the receiver's linear region. A plot of the error in dB is shown in Figure 40 below.

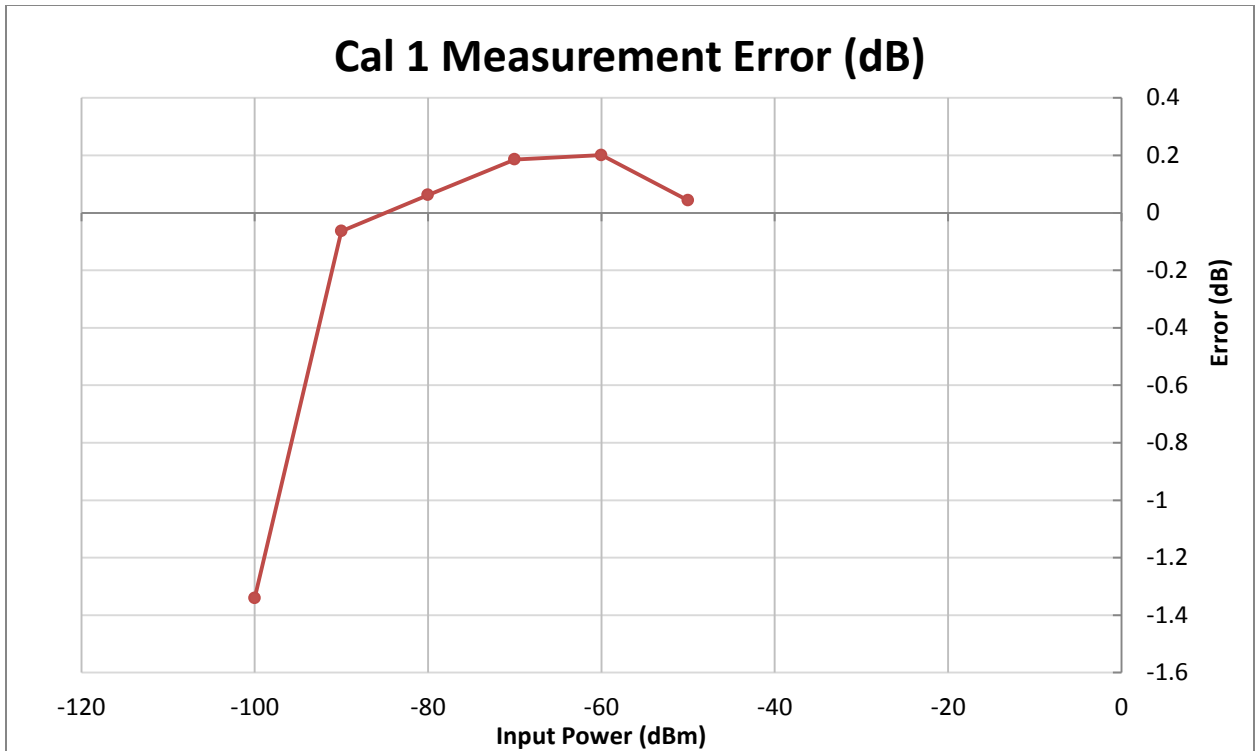


*Figure 40: Deviation between manual calibration and calibration tool results in dB. Results are shown for linear region, -100 dBm input and above.*

From -90 dBm to -50 dBm, the measured output power varies less than 0.2 dB. This variation may be caused by cable loss or receiver gain variation. The SMA/SMC adaptor used to connect the receiver IF output to the ADC is not present when taking signal analyzer measurements, so the signal at the ADC may be slightly weaker than the same signal at the signal analyzer depending on the cable loss. Also, we found that receiver gain measurements taken using the signal analyzer can vary by about  $\pm 0.1$  dB in a short period of time, so the error may just be from the receiver itself.

The second calibration, shown in the second row of Table 1, used a pulsed waveform signal as an input to the receiver, set to 0 dB of attenuation. Figure 41 shows the computed pulsed calibration gain curve compared to the computed continuous signal calibration gain curve. The results are quite consistent with the CW signal calibration tool results of the first calibration, although there is slight deviation for the low input power signals.



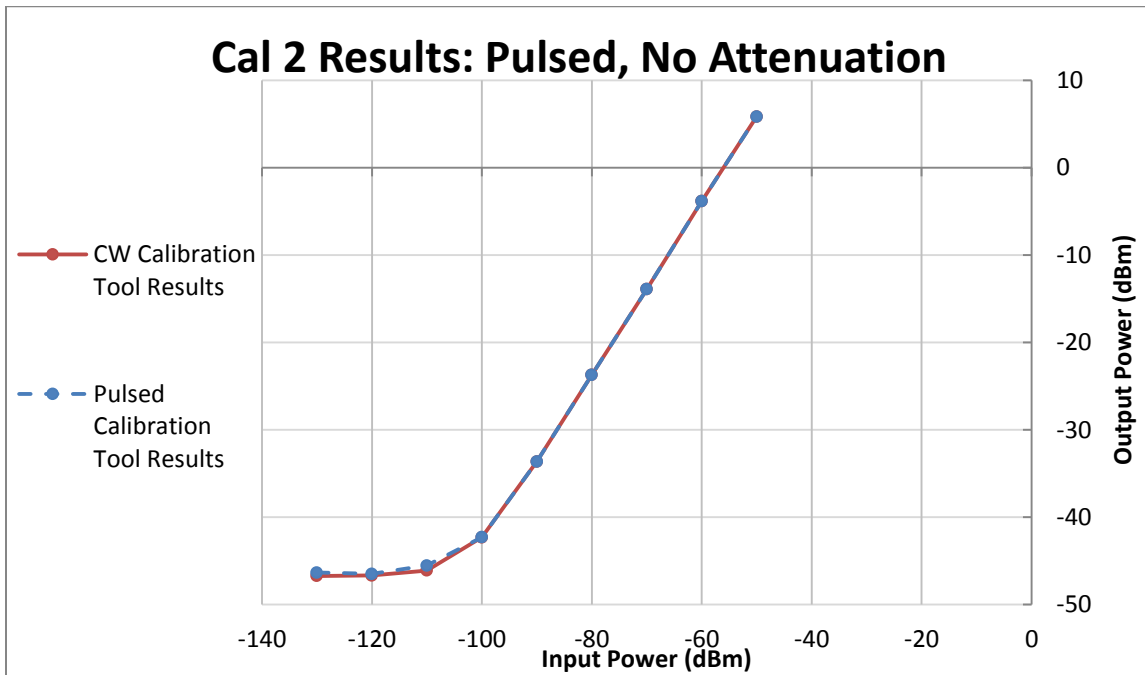
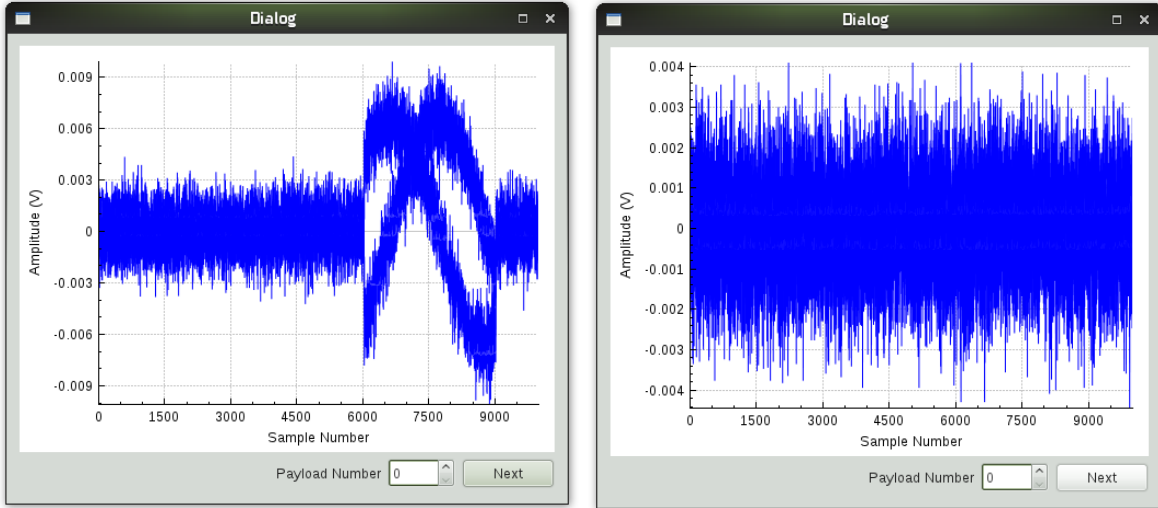


Figure 41: Pulsed calibration results compared to corresponding continuous calibration results for 0 dB IF attenuation setting.

For low input power signal recordings, the pulse location is not detectable, as shown in Figure 43. The program instead uses the pulse range indexes of the next highest input power recording.



*Figure 42: Screenshot of payload waveforms of pulsed calibration for input power of -90 dBm (left) and -120 dBm (right). Pulse is buried within the noise.*

The third set of calibration recordings was taken using a CW input signal with the variable attenuator set to the maximum setting, enabling us to make recordings in the receiver's compression region. The variable attenuator is located in front of the IF amplifiers in the receiver design. The attenuation lowers the gain by 31 dB, which also means that the point at which the signal becomes distinguishable from the noise floor occurs at an input power 31 dB above normal, limiting the dynamic range. Figure 43 compares the calibration tool results with manual measurements. Again, the computed output power levels in the linear region are within 0.2 dB of the values measured using the signal analyzer, as shown in Figure 44.

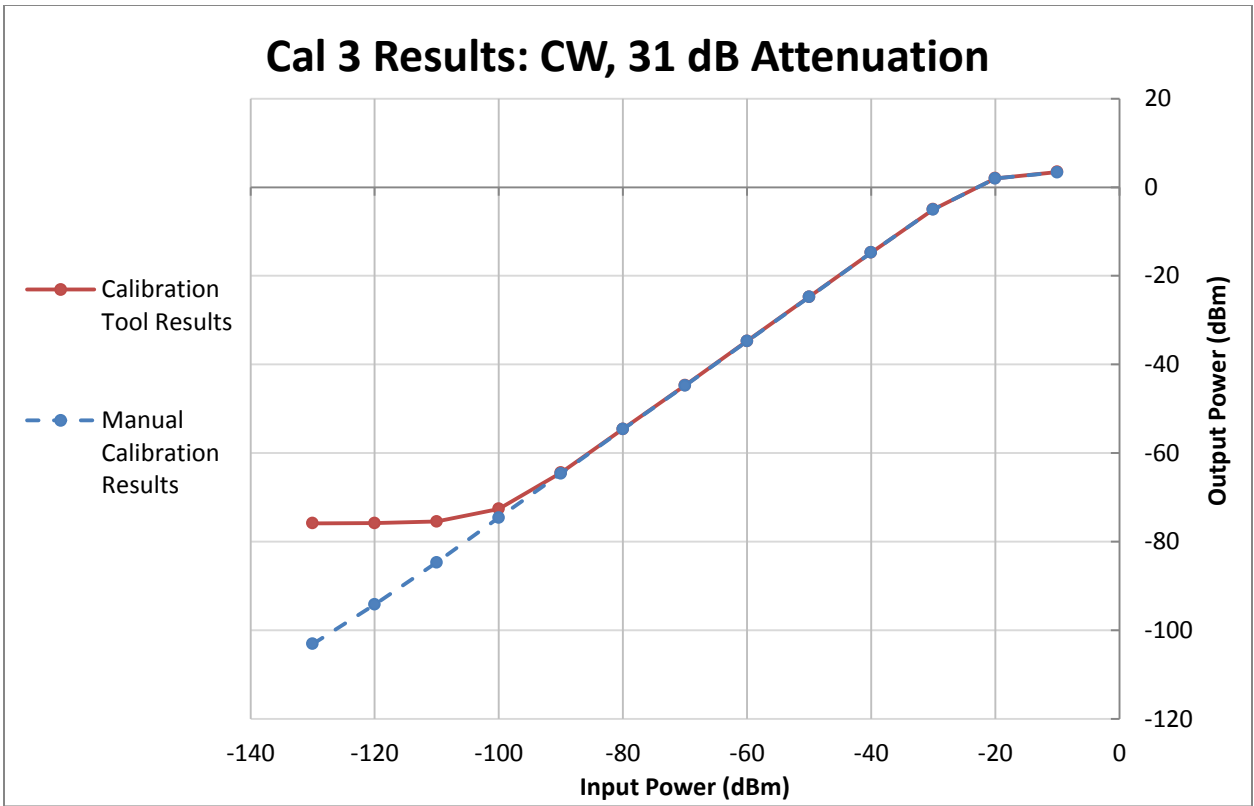
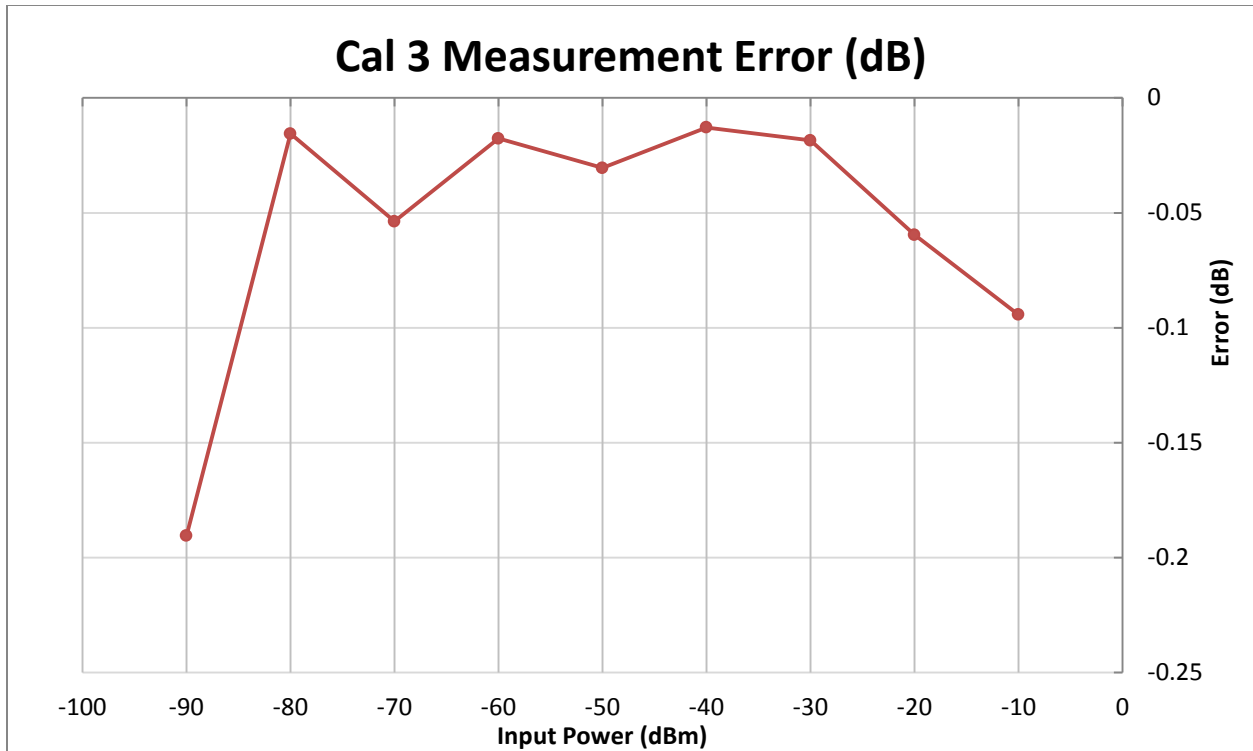


Figure 43: Results from manual and computed calibration of test receiver with 31 dB of IF attenuation and a CW input signal.



*Figure 44: Deviation between manual calibration and calibration tool results in dB. Results are shown for linear region, -90 dBm input and above.*

The final calibration was performed using a pulsed input signal with the receiver set to 31 dB of attenuation. The pulsed results plotted alongside the CW results are shown in Figure 45, and the two data sets are very consistent.

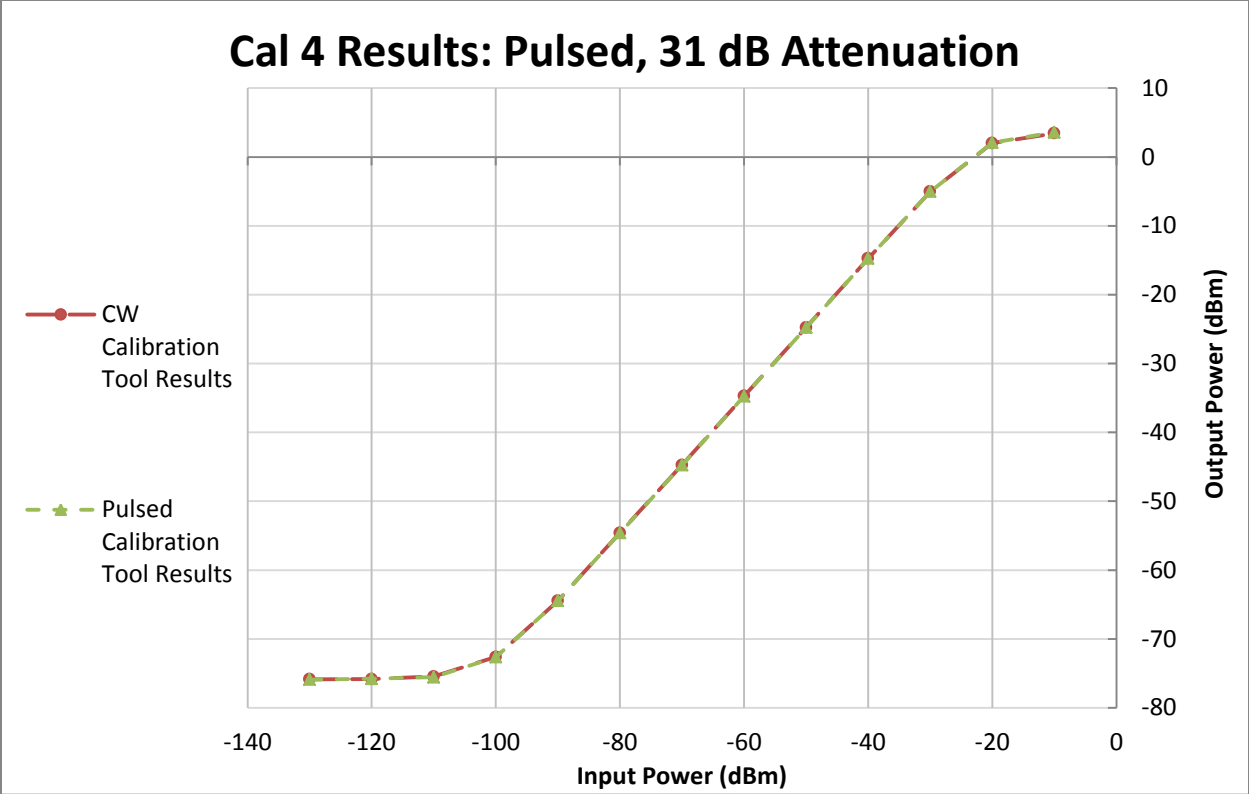


Figure 45: Pulsed calibration results compared to corresponding continuous calibration results for 31 dB IF attenuation setting.

#### 4.2.2 Calibration Tool Use Demonstrations

To demonstrate the usefulness of the calibration tool, a few additional calibrations were performed. To examine the change in receiver gain based on how long it has been powered on, we performed three calibrations at three different elapsed times after power-up. The calibrations were done using the calibration tool, and the receiver was set to 16 dB of IF attenuation.

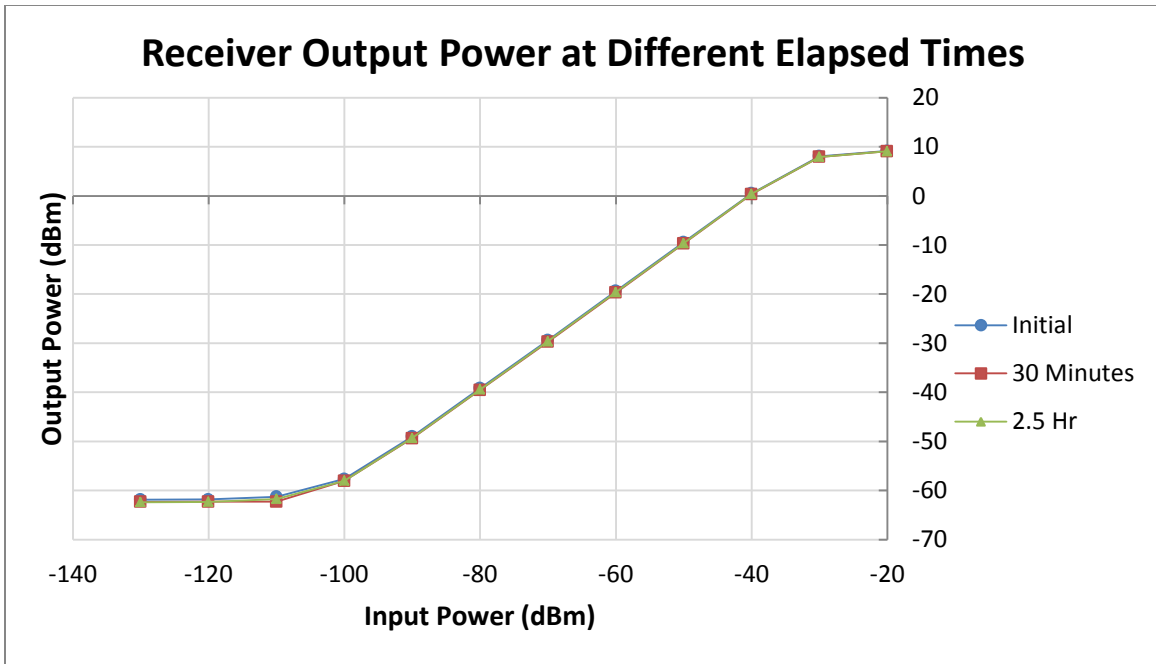


Figure 46: Receiver output power after 0, 30, and 150 minutes of run time, as calculated by the calibration tool.

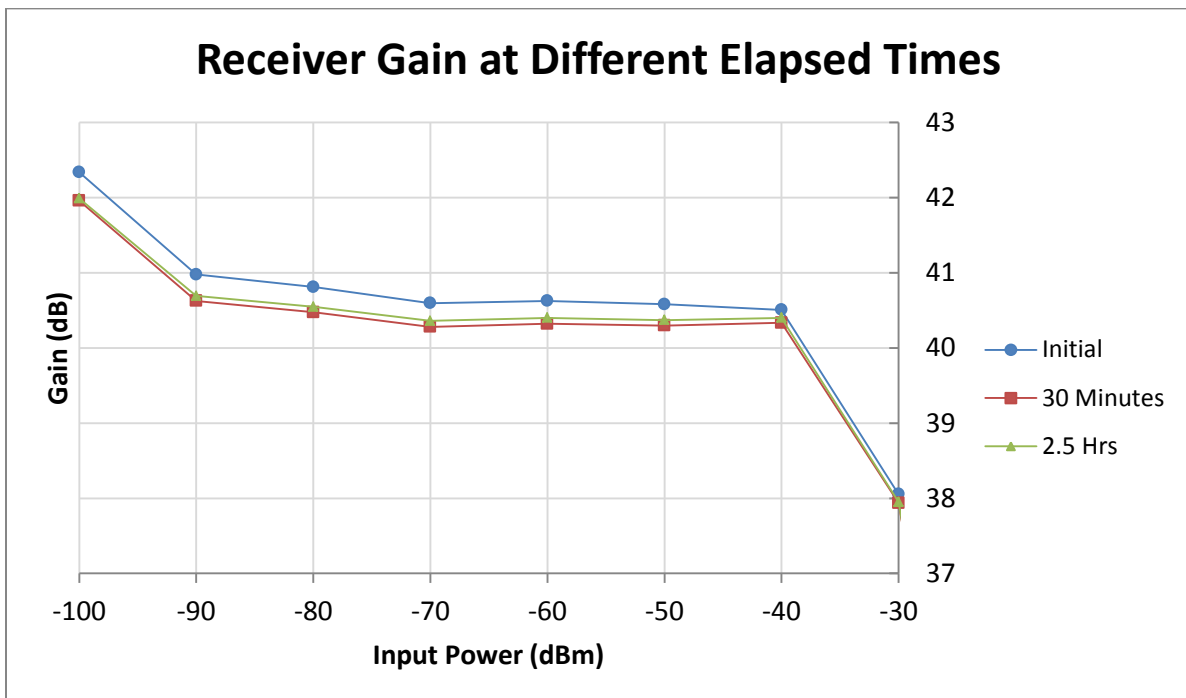


Figure 47: Gain of receiver after 0, 30, and 150 minutes of run time.

Figure 46 and Figure 47 show how the receiver performance can vary even in a room temperature setting. When the receiver is turned on, it takes a few minutes for the electronics to heat up and reach their final, stable gain value. Over the linear range of the receiver, the final gain value is approximately 0.2 – 0.3 dB below the initial value.

A major benefit of using the calibration toolkit is easy detection of receiver malfunction. If the plot or the numeric results of the calibration appear different than expected to the operator, chances are there is a problem with the receiver configuration, the recording software, or the receiver itself.

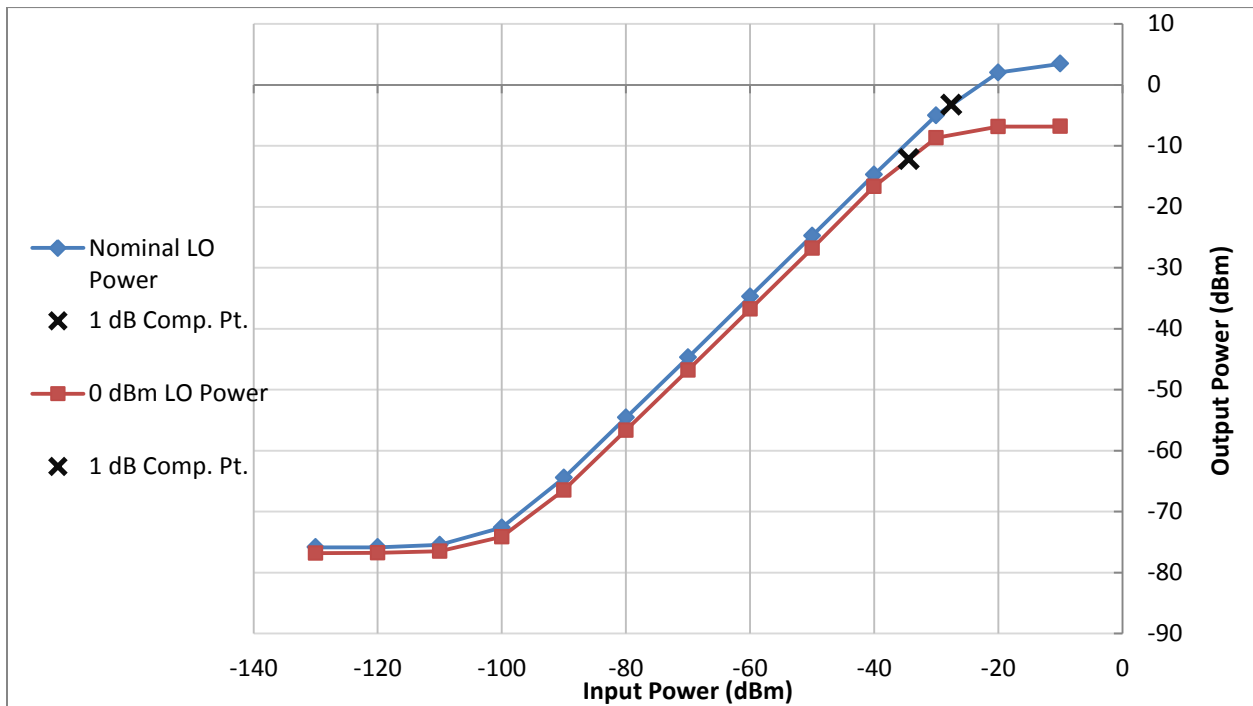


Figure 48: Calibration tool plots for two receiver setups; nominal and weak LO power.

Figure 48 shows two calibrations of the test receiver, set to 31 dB of IF attenuation. One was performed with the LO power at 21.75 dBm, the nominal level specified on the design schematic, and one was performed with the LO power at 0 dBm. The calibration was performed using our tool.

Table 2: Calibration toolkit results for nominal and weak LO power receiver setups.

LO Power	Calibration Factor (dB)	1 dB Compression Point (dBm)
21.75 dBm	25.2567	-27.5503
0 dBm	23.1913	-34.3973

In this scenario, calibration of the receiver with nominal and 0 dBm LO power levels yields two cal factors that only differ by about 2 dB, but 1 dB compression points that vary by almost 7 dB. The difference in compression region performance can also be observed when plotting both curves as in Figure 48. If the operator knows roughly where the 1 dB compression point should be for a receiver, a significantly different 1 dB compression point calculation from the calibration tool alerts the operator to a possible error in the receiver setup. In this case, the error is that the LO signal is too weak.

#### 4.2.3 Receiver Noise Floor Determination

As previously mentioned, the calibration tool is currently unable to distinguish signals in the presence of significant receiver noise, and thus displays the noise floor at a power greater than that of the true receiver noise floor. The combined noise power over the entire bandwidth of the signal overpowers the signal and dominates the power calculation. The spectrum analyzer shows a lower noise floor, since it shows the power at the specific signal frequency by computing the Discrete Fourier Transform (DFT) of the signal. This limitation restricts the usefulness of the software, since manual calibration measurements can reach the true noise floor and are not affected by broadband noise power. Though the calibration tool does not employ such techniques due to the time constraints of this project, an implementation in MATLAB was developed as a proof-of-concept that filtering and averaging of the signal is a viable method of reducing the signal noise to expose the desired waveform at low power levels. For each payload, the simulation applies a 2<sup>nd</sup> order Butterworth bandpass filter to each of the I and Q data and computes the amplitudes of the final 5000 filtered data points, ignoring the first 15,000 because of the filter startup time. The filter is not operating in steady-state until after



15,000 samples, since the passband chosen is so narrow: about  $0.0002 \cdot \pi$  radians /sample in normalized frequency. A narrow passband ensured the minimum amount of noise from frequencies other than the signal frequency, which is important at low power levels. Unfortunately, consecutive payloads are not contiguous data recordings, so the filter had to be applied to each payload individually. The effect of the filter on the I data of one payload is shown in Figure 49.

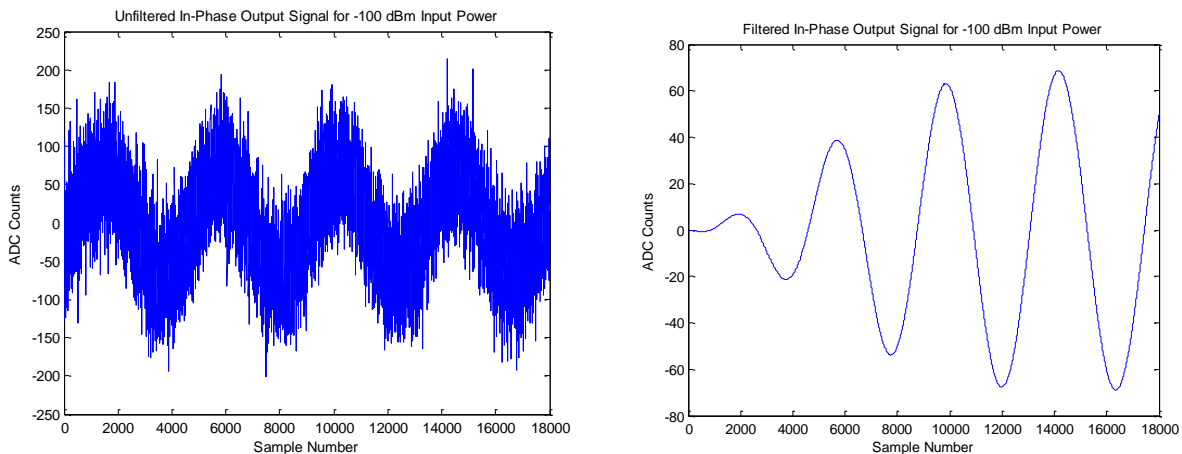


*Figure 49: Unfiltered (left) and filtered (right) in-phase waveforms of output signal corresponding to -100 dBm input power.*

Using such a narrow filter enables maximum filtering of unwanted noise, but causes the passband gain of the filter to be less than one. Because the filter introduces some loss to the signal, an attenuation factor is calculated from the ratio of the filtered data to the unfiltered data for a high power input signal, where noise is negligible. The filtered data are divided by this factor to restore the amplitudes to the original values prior to the filter. The mean of the scaled, filtered amplitudes is found and converted to dBm from ADC counts. This process is repeated for each recording, and the computed output power value of each recording is calculated and plotted.

To test the algorithm, we used the recordings of signal generator output to ensure the results were accurate and to test the lowest power value that could be calculated. Figure 50 below shows that the calculated values are very close to the nominal power values from the

signal generator. Also, the algorithm is capable of computing power levels well below -80 dBm, the minimum value that could be measured without filtering.

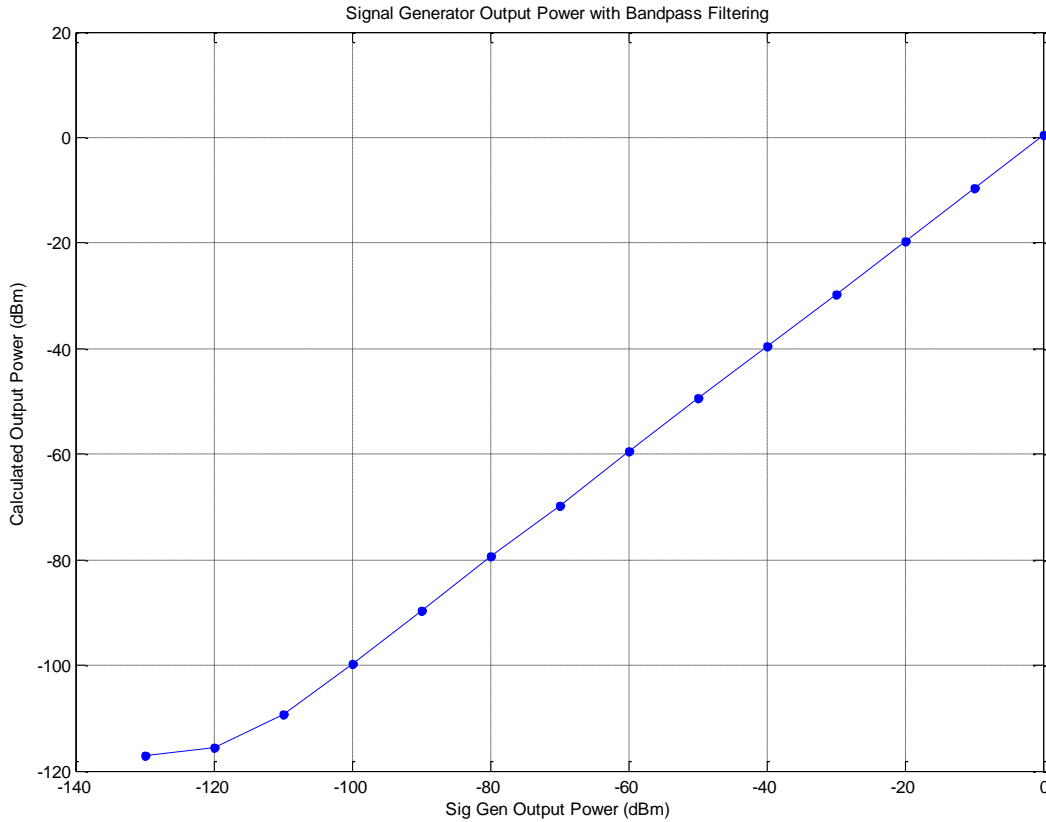


*Figure 50: MATLAB algorithm plot of calculated power levels of signal generator CW tones.*

The lowest output power calculated, closest to the noise floor of the signal generator, is -117.2 dBm. The true noise floor of the signal generator is about 133.7 dBm/Hz, measured using a signal analyzer. Part of this discrepancy is related to the resolution of the ADC at low voltages. At -130 dBm, the ADC represents the signal with values ranging from merely -3 to 3 counts, shown in Figure 51 below.

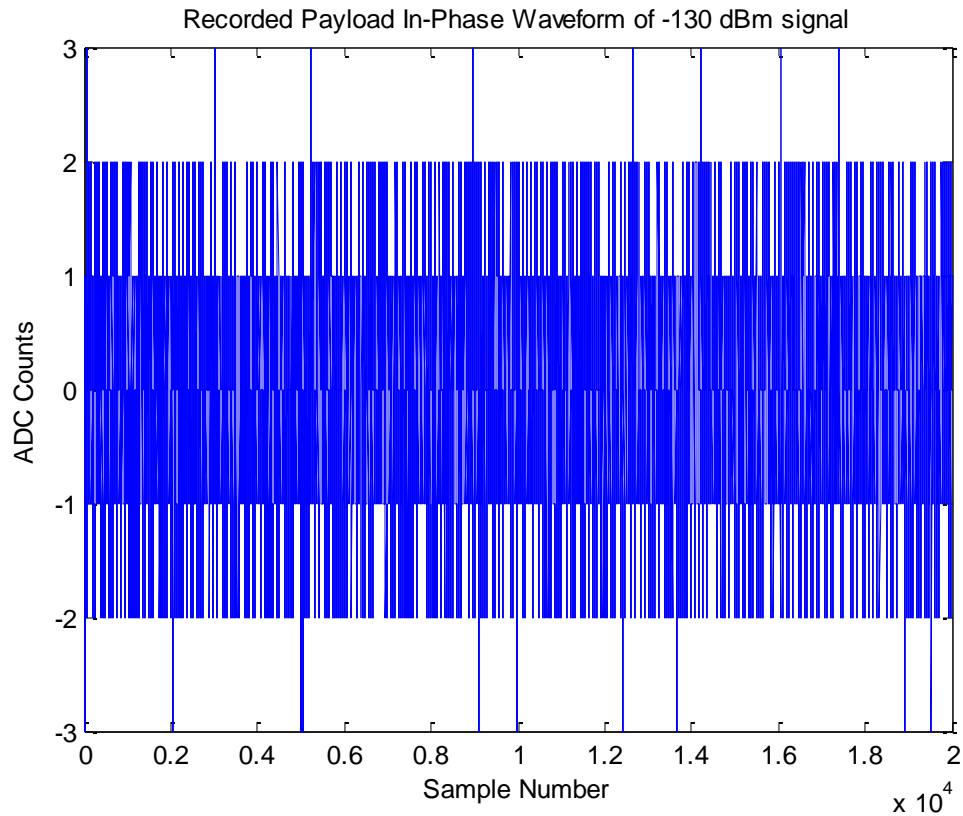


*Figure 51: Unfiltered In-phase waveform of -130 dBm signal from signal generator.*

Even with filtering and averaging, at a certain point the quantization error of the ADC skews the amplitude calculation. However, the noise floor of most receivers is well above the minimum level the algorithm is capable of calculating, so this limitation is not a serious drawback.

To further demonstrate its functionality, the MATLAB algorithm was run on the calibration recordings of the test receiver. The recordings were taken with CW input signals with no attenuation, the same test data as in Calibration 1 in Section 4.2.1, with additional recordings at lower input power levels. Figure 52 shows the bandpass filtering algorithm results compared to the calibration tool results and manual measurements. The complete data are listed in Appendix F.

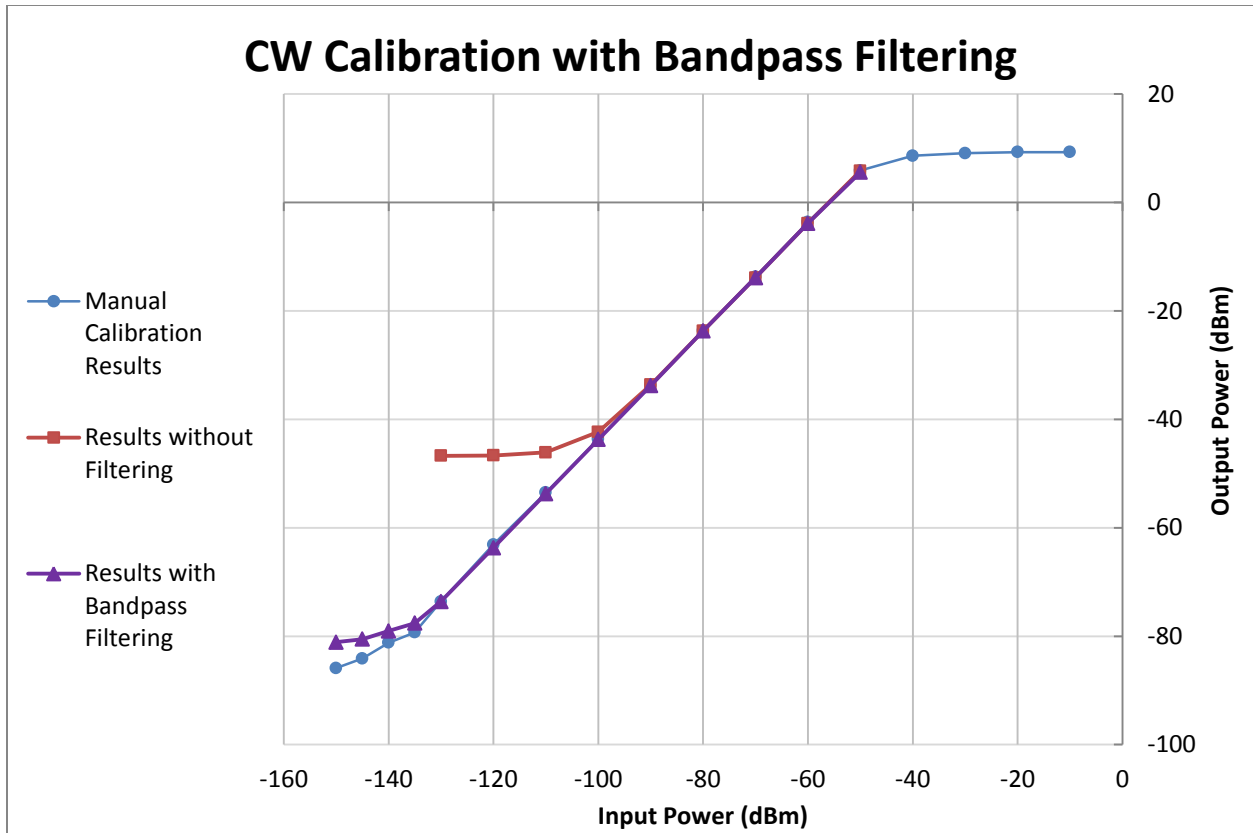


Figure 52: Bandpass filtering algorithm results compared with calibration tool results (without filtering) and manual calibration results.

This algorithm comes much closer to the receiver noise floor level of -86 dBm than the calibration tool. Further refining of the filtering process might facilitate measurements as precise as the signal analyzer.

Since the signals we analyzed with the simulation were generated at a known frequency in the test lab, the normalized high and low cutoff frequencies of the Butterworth filter were manually calculated and coded into the filter. Ideally, an FFT should be applied to the signal to allow for determination of an unknown test signal's frequency. Nonetheless, the MATLAB implementation indicates that with the proper implementation of filtering, scaling, and averaging in C++, the performance of the calibration toolkit could be substantially improved to detect signals of power levels down towards the receiver noise floor.

## Chapter 5: Discussion

The results of our simulation and testing of the physical S-band radar receiver show that frequency and temperature affect receiver performance significantly. As expected, gain remained relatively flat across the in-band frequency range for our model simulation and hardware measurements and decreased sharply as the signal frequency moved out-of-band. Within the frequency range of 3.008 GHz to 3.012 GHz, gain remained flat to within 1 dB for both our simulation and hardware tests. Near the edges of the passband (approximately 3.007 GHz and 3.013 GHz), gain decreased between 1.6 to 1.9 dB from the average gain within 3.008 GHz to 3.012 GHz for both our simulation and hardware measurements. Since some radar receivers allow for a tunable center frequency, it is important that the operator calibrate if this setting is changed. Over  $-40\text{ }^{\circ}\text{C}$  to  $+85\text{ }^{\circ}\text{C}$ , our model showed that the overall gain of the receiver should vary by as much as 5.26 dB. This variation is just an example; different receivers are subject to different amounts of gain variation depending on the design. Generally, radar systems are not used in environments outside of the range of approximately  $0\text{ }^{\circ}\text{C}$  and  $+50\text{ }^{\circ}\text{C}$ , or  $+32\text{ }^{\circ}\text{F}$  and  $+122\text{ }^{\circ}\text{F}$ , but hardware testing confirmed these temperatures cause significant gain variation as well. From  $0\text{ }^{\circ}\text{C}$  to  $+50\text{ }^{\circ}\text{C}$ , the LNA alone contributes 0.91 dB of gain deviation according to our test measurements.

Clearly radar receiver performance depends heavily on the temperature of the environment. However, even with the receiver at room temperature, the electronics heat up from operation, causing a change in gain over time. In general, frequent calibration is a prudent practice to ensure accurate results, and it makes sense to calibrate before every mission, especially under atypical environmental conditions. However, the receiver should be calibrated after the receiver electronics have been allowed time to heat up to a constant temperature. A calibration performed as soon as the receiver is powered on will not be valid for data taken after a few minutes. For verification purposes, a calibration could also be performed after the mission is complete, to ensure the calibration factor has not changed since the initial calibration. Missions during which the temperature varies significantly may even warrant additional calibrations in the middle of the mission.

Ultimately, radar operators should make the decision of how often to calibrate based on the variance of the calibration results. Certain receivers will be more vulnerable to gain variation than others, depending on their design and operating conditions. If an operator calibrates a receiver several times under different environmental conditions and determines that there is very little gain variation, perhaps that receiver is more resistant to temperature effects, and does not need to be calibrated as often. When in doubt, however, frequent calibration may be a good idea, and our calibration tool supports that effort, enabling operators to calibrate quickly and easily.

The calibration tool improves the process of calibration by expediting and standardizing it. Essentially, the only difference between the calibration setup and the data collection setup is that the signal generator or other test signal source is connected to the RF input of the receiver, bypassing the antenna. There is no need to attach additional instrumentation; the IF output remains connected to the ADC. Also, because the tool can calibrate with pulsed test signals, the real-time server does not have to be reconfigured to acquire CW data. In addition, eliminating the need for the operator to make signal analyzer power measurements mitigates user error, such as incorrect instrumentation setups or incorrect readings. Because the calibration tool works with data in the ROSA file format and works at any frequency, many different systems can use the tool.

## **5.1 Limitations**

### **5.1.1 Model Simulation and Hardware Test Measurements**

While our model based on vendor-measured data proved to be very accurate as compared to test measurements of the actual hardware, it cannot necessarily be used to predict the performance of other receivers. The general trends observed in our simulation and test measurements for temperature changes should hold true for most receiver structures, but numerical estimations of gain variation cannot be assumed to apply to other systems. The receiver model trend of decreasing gain for increasing frequency within the band of operation cannot be extrapolated to other receivers since different radars operate in diverse frequency

bands and may employ configurations and components that differ from our S-band hardware receiver. The benefit of our model thus lies in providing a high level approximation of how gain will typically vary for temperature changes, as well as demonstrating that a model based on component datasheet values yields a reasonable approximation of a physical system. Hence, the methodology of our modeling and simulation may be applied to other radar receiver systems, or used for preliminary analysis in the development of a radar receiver, with high confidence in the accuracy of the model simulation. The major hindrance to using our modeling technique is that the simulation is limited to the constraints imposed by conditions tested by the vendor. Though many components were tested across a very wide range of frequencies, the simulation of the entire receiver was confined to the smallest frequency range common to every component. For some components, extrapolation of gain performance outside the frequencies tested by the vendor may reasonably be approximated, but this was avoided since there is no way to necessarily verify such values. As previously described in Section 3.3 our hardware temperature tests were severely limited by a lack of proper instrumentation and test environment control, therefore they serve to provide a general idea of how gain might vary with temperature rather than a representative dataset that describes the entire receiver's gain variation.

### **5.1.2 Calibration Tool**

Some of the limitations of the calibration tool can stem from the ADC used to collect the data. If the dynamic range of the ADC is not as high as the range of the receiver, the receiver output signal can reach voltages higher than the ADC can record. This problem causes clipping in the recordings, skewing the power calculations and possibly damaging the ADC. This issue existed in our test setup, and it prevented us from recording within the receiver's compression region without attenuating the IF signal. Additionally, low power signals are difficult to measure with the ADC, since the effective resolution of the signal will be degraded. When the signal is represented by a small number of bits, quantization error has a more significant impact.

Due to time constraints, some of the algorithms implemented in the toolkit have some inherent limitations. Finding the linear region of the curve currently only uses a sliding window

method with a window size of three, but higher accuracy could be achieved with a window size that changes depending on the data. When there are a high number of data points in the linear region, a larger window size would enable an average gain value that is a better representation of the entire linear region. The window size would also shrink if the linear region was very narrow or if few data points were present.

One of the major drawbacks of the calibration tool as compared to manual calibration is its limited capability at low power levels. Broadband noise power obscures signal power when the signal power is low enough. This problem can be solved by using a matched filter on the output of the IF signal, attenuating all noise other than at the frequency of the signal. This practice is common in the field. However, without matched filtering, digital filtering can be implemented in the calibration tool as outlined in the next section.

### **5.1.3 Future Work**

As it stands now, our deliverable is a strong tool for calibrating radar receivers, but it could be improved by refining and adding features. An area for future work is the calibration toolkit's limited capability at low power levels. To fix this limitation in software, future work on the calibration tool should include implementing an algorithm for bandpass filtering the recordings to reduce noise, enabling accurate power measurements of the desired signal even when noise is present. This addition is necessary for measuring the true receiver noise floor, a useful indicator of receiver health. As outlined in the results, the amplitude calculation algorithm should be altered to compute the DFT of the I/Q data to automatically find the test signal frequency, apply a bandpass filter to the data about that frequency, and then extract and average the amplitudes of the I/Q data. Since filtering can introduce a small amount of attenuation in the pass band, care must be taken to counteract that attenuation in order to obtain accurate amplitude results. The application should be further modified to display the receiver noise floor level on the results screen as a numeric value.

Additionally, the 1 dB compression point calculation algorithm could be improved to implement more advanced interpolation. Currently, the tool computes this value using linear



interpolation to find values in between data points of the gain curve. By interpolating the data using more complex curve fitting, values in between data points would more closely model the actual performance of the receiver.

For greater compatibility with radar systems, more file reader classes could be added to the tool. Though we found that the ROSA II Pulse Short T file format was the most common format for data recordings, there are additional formats that could be easily incorporated into the tool. The file reader classes, initially created by the developers of Post-Mission Analysis, have a hierarchical structure that allows for easy addition of new formats.

Full automation of the calibration procedure could also be worthwhile, since it would require minimal effort from the operator. To do this, the signal generator and ROSA recording software would both be controlled by the calibration tool, so that the calibration could be completed in one step. The calibration tool would use a network or direct connection to the signal generator to control its output, stepping through the calibration process automatically. The ROSA software suite would be modified to enable the calibration tool to control the recording of data. The calibration tool could then step through the input power levels, take recordings at each level, and compute the calibration results within seconds. This end-to-end solution would simplify the calibration process even further, though its complexity outweighs the benefits at this time.

## Chapter 6: Conclusions

The radar receiver calibration toolkit streamlines the calibration process, enabling immediate feedback for the operator on the performance of the receiver. To ensure it is ready for use in the field, the tool was tested using data from a real receiver. The testing showed that the calibration tool results differ from measurements taken using instrumentation by less than 0.2 dB, which is an acceptable margin. The calibration tool's power calculations can be obscured by the presence of strong broadband noise, but this limitation can easily be fixed using bandpass filtering to isolate the desired signal. Group 108 specified that such bandpass filtering was not necessarily a desired feature of the tool, and that they would instead prefer to use a matched filter implemented in digital signal processing within the radar to reduce noise. Overall, the calibration tool meets the initial goal of providing automated receiver gain calibration for varying radar systems.

In the months following the project, the toolkit will be installed and used by radar analysts and operators in Group 108. They will likely modify it as needed, so the code was left as modular and well-commented as possible. Our toolkit application simplifies and supports calibration efforts, potentially improving flight test practices for Group 108 by preventing wasted flight test time and resources.

## References

- Davis, W. A. (2011). *Radio Frequency Circuit Design*, Second Edition. Hoboken, NJ: John Wiley & Sons, Inc. pp. 198, 200.
- Dazhuan, X., Shenghua, Z., Xueming, J. (2005) "ADC limitations on the dynamic range of a digital receiver", *Microwave, Antenna, Propagation and EMC Technologies for Wireless Communications*, 2005. MAPE 2005. IEEE International Symposium on. pp. 79 - 82 Vol. 1.
- Gekat, F., Mehl, J., Rühl, D., & Verstappen, C. (2003). Linearity and Calibration of Linear Radar Receivers. Neuss, Germany. AMS-Gematronik. 31<sup>st</sup> International Conference on Radar Meteorology. American Meteorological Society.
- Kalivas, G. (2009). *Digital Radio System Design*. West Sussex, United Kingdom: John Wiley & Sons Ltd. pp 221-222.
- Knott, E. F. (2006). *Radar Cross Section Measurements*. Raleigh, NC: SciTech Publishing. pp. 1, 12-15, 122, 125.
- Lundberg, K. H. (2002). *Analog-To-Digital Converter Testing*. Massachusetts Institute of Technology. [web.mit.edu/klund/www/papers/UNP\\_A2Dtest.pdf](http://web.mit.edu/klund/www/papers/UNP_A2Dtest.pdf)
- Martinez, D.R., Bond, R.A., Vai, M.M. (2008). *High Performance Embedded Computing Handbook: A Systems Perspective*. Boca Raton, FL: Taylor and Francis Group. Pg. 151-154.
- National Instruments. (2006). Performing I-Q Measurements Using the PXI-5660. <http://www.ni.com/white-paper/2867/en/>
- O'Donnell, R. RES.II-001 Introduction to Radar Systems, Spring 2007. (MIT OpenCourseWare: Massachusetts Institute of Technology). <http://ocw.mit.edu/resources/res-ii-001-introduction-to-radar-systems-spring-2007> (Accessed 23 Sep, 2013). License: Creative Commons BY-NC-SA.

Razavi, B. (2011). *RF Microelectronics*, Second Edition. Upper Saddle River, NJ: Prentice Hall. pp. 17, 157-158, 162, 164, 166.

Rejto, S. B. (2000). Radar Open Systems Architecture and Applications. Proceedings of IEEE International Radar Conference, pp. 654-659. MIT Lincoln Laboratory.  
<http://ieeexplore.ieee.org/xpl/articleDetails.jsp?arnumber=851911>

Skolnik, M. I. (1980). *Introduction to Radar Systems*. New York: McGraw-Hill.

Skolnik, M. I. (2008). *Radar Handbook*, Third Edition. The McGraw-Hill Companies. pp. 1.2, 6.1, 6.5, 6.7, 6.11-6.12, 6.23, 6.26.

Smith, J.O. (2007). *Mathematics of the Discrete Fourier Transform (DFT)*. Booksurge. Pg. 31-36.

## Appendix A: Simulation Datasheet Sources and Estimated Values

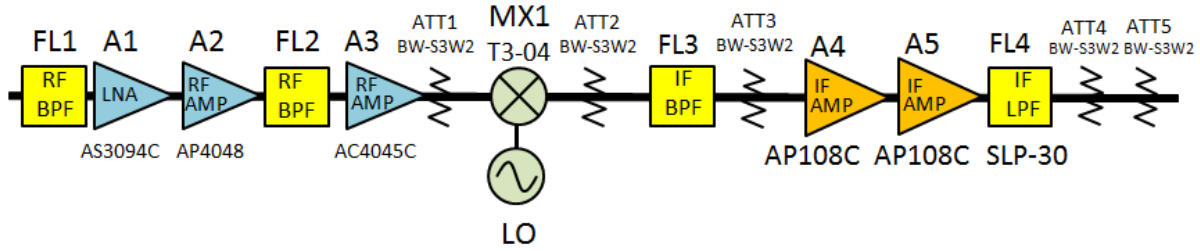


Figure 53: Simplified circuit schematic of hardware test receiver. Components not necessary to the core functionality were omitted. Components without model numbers were custom ordered. Each component displayed in this schematic was simulated in our model.

The following material describes how data were obtained in modeling each component of Figure 53. The data were used for interpolation at common frequencies and temperatures to allow for proper cascade of the component gains or losses, i.e. these values may not have been the exact ones used in the simulation but rather used to interpolate for the values that were used in simulation. Some component names shown in Figure 53 differ slightly from what is displayed on their datasheets. The amplifiers in Figure 53 were all manufactured by Teledyne-Cougar but labeled as Teledyne Microwave Solutions in their datasheets. The following descriptions use the names presented by the datasheets.

### RF Bandpass Filter FL1

The first component simulated in the model is a custom-ordered K & L Microwave RF bandpass filter. Due to a lack of available performance data for this device at Lincoln Laboratory and lead time in contacting the vendor for information, the component's insertion loss was measured directly on an Agilent Technologies N5230A PNA-L Network Analyzer. For temperatures of +25 °C and +50 °C, the filter's insertion loss was recorded at multiple frequencies. The testing process is described in detail in section 3.3. Linear extrapolation on a dB scale was used to calculate insertion loss for each tested frequency at -40 °C and +85 °C operating temperatures. Then, the filter's loss was linearly interpolated on a dB scale at fixed temperatures of -40 °C, +25 °C, and +85 °C for each point in the common system frequency

array (discussed in section 3.2.2 using the loss values at the two closest measured frequencies. Explicit interpolation across the operating temperature range for a given frequency was not performed; instead the lines connecting the loss-temperature points were drawn to graphically display the change in temperature.

*Table 3: Custom K & L Microwave RF bandpass filter (RF BPF FL1). Insertion loss across frequency was measured on a network analyzer for +25 °C and +50 °C and then extrapolated for -40 °C and +85 °C.*

Frequency (GHz)	Insertion Loss (dB)			
	-40 °C (extrapolated)	+25 °C (measured)	+50 °C (measured)	+85 °C (extrapolated)
2	71	71	71	71
2.2	50.44	50.7	50.8	50.94
2.3	36.26	36	35.9	35.76
2.4	15.222	14.52	14.25	13.872
2.442	3.286	3	2.89	2.736
2.466	0.088	0.53	0.7	0.938
2.484	0.219	0.31	0.345	0.394
2.5	0.225	0.29	0.315	0.35
2.6	0.245	0.31	0.335	0.37
2.7	0.132	0.21	0.24	0.282
2.8	0.132	0.21	0.24	0.282
2.9	0.155	0.22	0.245	0.28
3	0.157	0.235	0.265	0.307
3.01	0.129	0.22	0.255	0.304
3.1	0.149	0.24	0.275	0.324
3.2	0.232	0.31	0.34	0.382
3.3	0.356	0.46	0.5	0.556
3.34	0.623	1	1.145	1.348
3.36	2.872	3.08	3.16	3.272
3.4	11.599	12.99	13.525	14.274
3.5	36.332	35.5	35.18	34.732
3.6	49.36	50.4	50.8	51.36
3.8	71	71	71	71
3.9	77.6	75	74	72.6
4	79	79	79	79

## LNA A1

The datasheet for the AS3094 amplifier provides a graph of device gain versus frequency, shown in Figure 54 on the left, where each curve corresponds to a particular test temperature, -55 °C, +25 °C, or +85 °C. A table of “typical automatic test data”, shown in Figure 54 on the right, complements the graph, reporting vendor-measured gain values at specific frequencies without indication of temperature. Simulation data were thus determined by manually estimating the gain of each curve in the graph at the frequency points listed in the typical automatic test data table.

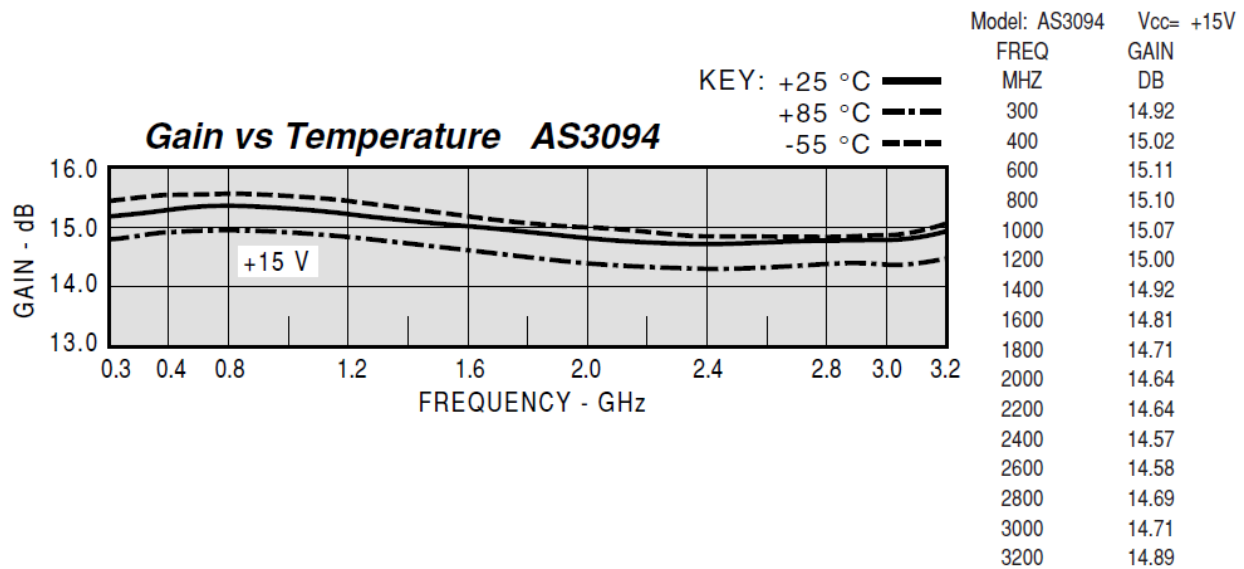


Figure 54: Teledyne Microwave Solutions AS3094 amplifier (LNA A1) gain versus frequency curves for three different operating temperatures, -55 °C, +25 °C, and +85 °C (left). Gain decreases with increasing temperature according to this graph. Vendor also provides typical automatic test data table (right).

*Table 4: AS3094 amplifier (LNA A1) gain values estimated from vendor-provided graph shown in Figure 54 on the left. Gain was estimated for each operating temperature at the frequencies specified in the typical automatic test data table shown in Figure 54 on the right.*

Frequency (MHz)	Gain (dB)		
	-55 °C	+25 °C	+85 °C
300	15.465	15.2	14.78
400	15.555	15.33	14.9
600	15.56	15.36	14.94
800	15.58	15.385	14.95
1000	15.54	15.34	14.9
1200	15.46	15.24	14.82
1400	15.345	15.115	14.71
1600	15.19	15.01	14.6
1800	15.055	14.9	14.5
2000	14.99	14.8	14.39
2200	14.91	14.73	14.34
2400	14.845	14.69	14.3
2600	14.835	14.745	14.335
2800	14.82	14.76	14.39
3000	14.85	14.765	14.375
3200	15.08	14.935	14.475

## **RF Amp A2**

The datasheet for the AR4048 amplifier provides a graph of device gain versus frequency, shown in Figure 55 on the left, where each curve corresponds to a particular test temperature, -55 °C, +25 °C, or +85 °C. A table of “typical automatic test data”, shown in Figure 55 on the right, complements the graph, reporting vendor-measured gain values at specific frequencies without indication of temperature. Simulation data were thus determined by manually estimating the gain of each curve in the graph at the frequency points listed in the typical automatic test data table.



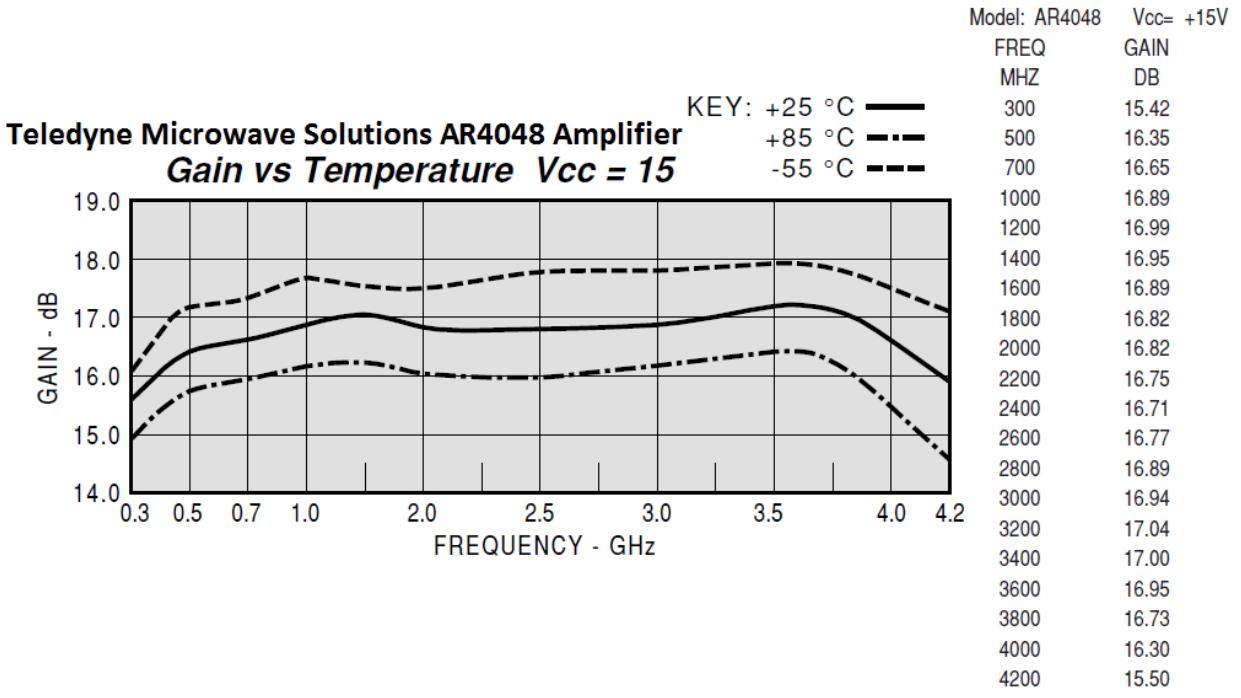


Figure 55: Teledyne Microwave Solutions AR4048 amplifier (RF Amp A2) gain versus frequency curves for three different operating temperatures, -55 °C, +25 °C, and +85 °C (left). Gain decreases with increasing temperature according to this graph. Vendor also provides typical automatic test data table (right).

*Table 5: AR4048 amplifier (RF Amp A2) gain values estimated from vendor-provided graph shown in Figure 55 on the left. Gain was estimated for each operating temperature at the frequencies specified in the typical automatic test data table shown in Figure 55 on the right.*

Frequency (MHz)	Gain (dB)		
	-55 °C	+25 °C	+85 °C
300	16.057	15.61	14.95
500	17.2	16.415	15.75
700	17.343	16.64	15.957
1000	17.686	16.9	16.157
1200	17.629	16.99	16.214
1400	17.543	17.028	16.243
1600	17.529	17.01	16.2
1800	17.5	16.94	16.142
2000	17.514	16.856	16.03
2200	17.614	16.8	15.99
2400	17.743	16.814	15.968
2600	17.814	16.828	16
2800	17.814	16.857	16.143
3000	17.814	16.9	16.171
3200	17.866	16.988	16.271
3400	17.907	17.133	16.357
3600	17.931	17.225	16.415
3800	17.8	17.057	16.11
4000	17.507	16.629	15.471
4200	17.093	15.914	14.55

## **RF Bandpass Filter FL2**

The RF cavity bandpass filter FL2, seen in Figure 53, is a custom-ordered part manufactured by Reactel, Incorporated. The filter’s insertion loss (or attenuation) performance was estimated from the graph shown in Figure 56, provided directly through correspondence with the vendor.

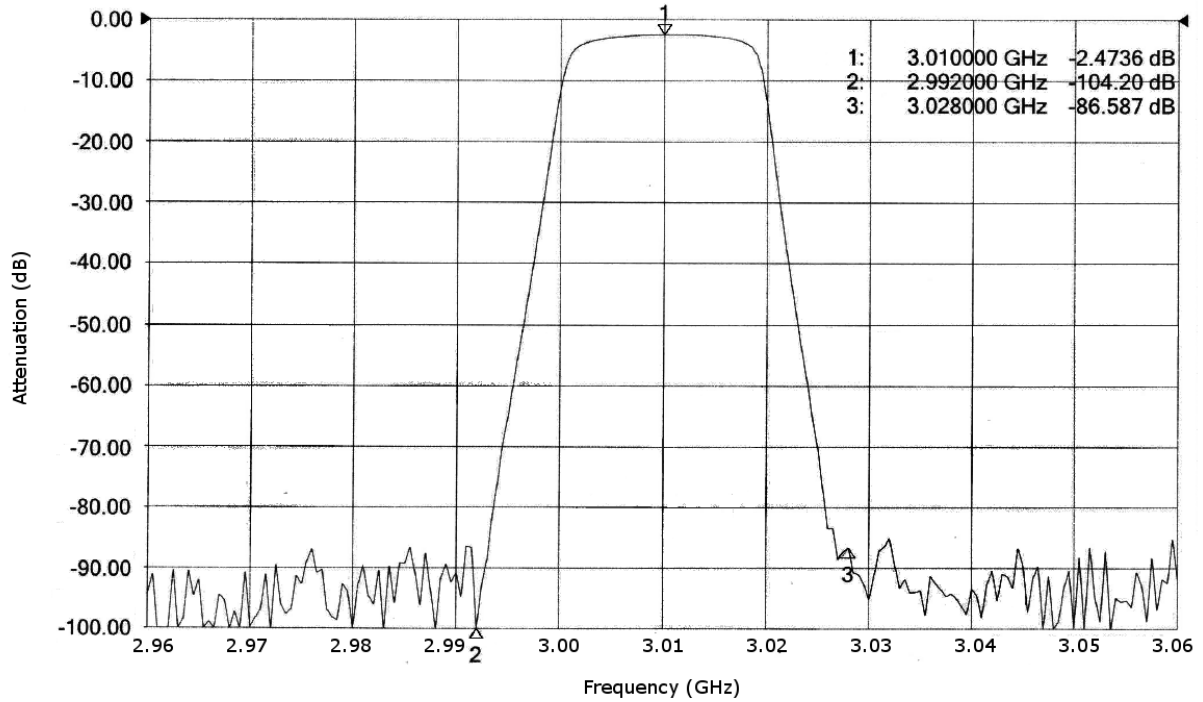


Figure 56: Custom Reactel, Inc. RF cavity bandpass filter (RF BPF FL2) attenuation (dB) versus frequency (GHz).

Though no numerical data for the filter's insertion loss with temperature variation were available from the vendor, a representative from Reactel informed us that their filters are considered very stable over the range from -40 °C to +85 °C and further stated that the vendor felt their devices would remain within their specification across this temperature range. Therefore, the values estimated from the graph were assumed constant across temperature in our model.

Table 6: Custom Reactel, Inc. RF cavity bandpass filter (RF BPF FL2) insertion loss values versus frequency, estimated from graph in Figure 56.

Frequency (GHz)	Insertion Loss (dB)	Frequency (GHz)	Insertion Loss (dB)	Frequency (GHz)	Insertion Loss (dB)	Frequency (GHz)	Insertion Loss (dB)
2.96	93.7	2.993	87.5	3.026	83.35	3.059	92.4
2.961	100	2.994	74.75	3.027	88.1	3.06	91.75
2.962	98.5	2.995	64.75	3.028	86.587		
2.963	100	2.996	54	3.029	90.8		
2.964	91	2.997	44	3.03	94.9		
2.965	92	2.998	33.75	3.031	87		
2.966	98.8	2.999	21.3	3.032	84.9		
2.967	94.3	3	11.1	3.033	93		
2.968	99.5	3.001	5.5	3.034	94		
2.969	98	3.002	4	3.035	93.75		
2.97	99.1	3.003	3.35	3.036	91.15		
2.971	97	3.004	3	3.037	93.45		
2.972	99	3.005	2.85	3.038	94.15		
2.973	95.9	3.006	2.7	3.039	96.35		
2.974	96	3.007	2.6	3.04	93.6		
2.975	92.3	3.008	2.5	3.041	97.65		
2.976	87	3.009	2.475	3.042	90.48		
2.977	91.65	3.01	2.4736	3.043	91		
2.978	98	3.011	2.4736	3.044	92.85		
2.979	92.85	3.012	2.475	3.045	89		
2.98	98.3	3.013	2.5	3.046	91.5		
2.981	90	3.014	2.55	3.047	98.45		
2.982	95.65	3.015	2.65	3.048	99.9		
2.983	99.4	3.016	2.99	3.049	93		
2.984	95	3.017	3.25	3.05	98		
2.985	89	3.018	4	3.051	98		
2.986	90	3.019	6.4	3.052	94.55		
2.987	88	3.02	13.5	3.053	88.2		
2.988	99	3.021	25	3.054	95.1		
2.989	89.3	3.022	38.5	3.055	95.2		
2.99	90.9	3.023	49.4	3.056	91.5		
2.991	86.15	3.024	59.5	3.057	97.9		
2.992	104.2	3.025	70	3.058	95.9		

## RF Amp A3

The datasheet for the AC4045 amplifier provides a graph of device gain versus frequency, shown in Figure 57 on the left, where each curve corresponds to a particular test temperature, -55 °C, +25 °C, or +85 °C. A table of “typical automatic test data”, shown in Figure 57 on the right, complements the graph, reporting vendor-measured gain values at specific frequencies without indication of temperature. Simulation data were thus determined by manually estimating the gain of each curve in the graph at the frequency points listed in the typical automatic test data table. Two extra points were estimated from the graph for greater resolution of gain data across frequency at each operating temperature. The last frequency of the typical automatic test data table was omitted from simulation data because it was outside the graph’s frequency range.

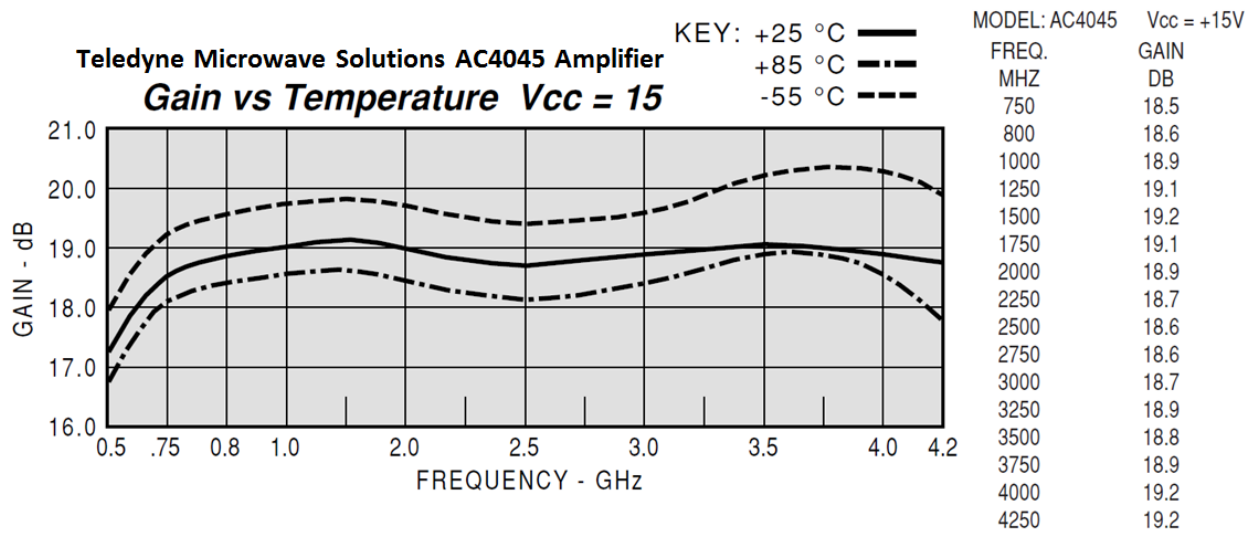


Figure 57: Teledyne Microwave Solutions AC4045 amplifier (RF Amp A3) gain versus frequency curves for three different operating temperatures, -55 °C, +25 °C, and +85 °C (left). Gain decreases with increasing temperature according to this graph. Vendor also provides typical automatic test data table (right).

*Table 7: AC4045 amplifier (RF Amp A3) gain values estimated from vendor-provided graph shown in Figure 57 on the left. Gain was estimated for each operating temperature at the frequencies specified in the typical automatic test data table shown in Figure 57 on the right. Gains at 500 MHz and 4200 MHz were also estimated. The frequency 4250 MHz is outside the graph's range and thus gain was not estimated for this frequency.*

Frequency (MHz)	Gain (dB)		
	-55 °C	+25 °C	+85 °C
500	17.96	17.25	16.75
750	19.235	18.53	18.1
800	19.59	18.875	18.414
1000	19.76	19.01	18.568
1250	19.8	19.085	18.625
1500	19.84	19.135	18.632
1750	19.8	19.08	18.564
2000	19.74	19	18.45
2250	19.53	18.825	18.245
2500	19.41	18.715	18.13
2750	19.48	18.815	18.218
3000	19.605	18.909	18.409
3250	19.9	18.99	18.664
3500	20.225	19.05	18.913
3750	20.355	19	18.9
4000	20.29	18.913	18.555
4200	19.9	18.768	17.791

### **Attenuators ATT1, ATT2, ATT3, ATT4, and ATT5**

In modeling Mini-Circuits' BW-S3W2+ attenuator, there were no temperatures specified for the unit's typical performance data, displayed in Figure 58. However, the electrical specifications listed a nominal attenuation of 3 dB at +25 °C, as well as provide the component's typical temperature coefficient of attenuation (TCA), 0.0004dB/dB/°C. Since the typical performance data closely matched the nominal attenuation value specified, these data were assumed to be taken at +25 °C. To find attenuation at a certain temperature, the TCA is

multiplied by the known attenuation and the temperature difference, and then added to the known attenuation. This process is shown in Equation 10, where  $Att_{T_1}$  represents the known attenuation of the component at temperature  $T_1$  and  $Att_{T_2}$  is the desired attenuation at temperature  $T_2$ :

$$Att_{T_2} = (Att_{T_1})(T_1 - T_2)(TCA) + Att_{T_1}$$

*Equation 10: Component's attenuation at a particular temperature is the sum of the known component attenuation at a given temperature with the product of this attenuation, difference between the given temperature and desired temperature, and temperature coefficient of attenuation. Attenuations are in dB, temperature in °C, and TCA in dB/dB/°C.*

### Typical Performance Data

Frequency (MHz)	Attenuation (dB)
1.00	2.72
100.00	2.74
1000.00	2.78
1999.90	2.82
5000.00	2.86
7999.90	2.95
9999.90	2.98
12400.10	3.02
15000.00	3.01
18000.00	3.23

*Figure 58: Attenuation across frequency for Mini-Circuits BW-S3W2 attenuator, (ATT1, ATT2, ATT3, ATT4, ATT5).*

Table 8: Attenuation values across frequency for Mini-Circuits BW-S3W2 attenuator, (ATT1, ATT2, ATT3, ATT4, ATT5). Values at +25 °C were taken directly from the vendor-provided data shown in Figure 58. Values at -55 °C and +85 °C were calculated using Equation 10 and the temperature coefficient of attenuation provided on the component datasheet.

Frequency (MHz)	Attenuation (dB)		
	-55 °C (calculated)	+25 °C (datasheet)	+85 °C (calculated)
1	2.63296	2.72	2.78528
100	2.65232	2.74	2.80576
1000	2.69104	2.78	2.84672
1999.9	2.72976	2.82	2.88768
5000	2.76848	2.86	2.92864
7999.9	2.8556	2.95	3.0208
9999.9	2.88464	2.98	3.05152
12400.1	2.92336	3.02	3.09248
15000	2.91368	3.01	3.08224
18000	3.12664	3.23	3.30752

## Mixer MX1 and LO

After speaking with one of our Lincoln Laboratory mentors regarding the conversion loss (attenuation) of the hardware receiver’s mixer across frequency, we determined that the mixer’s frequency response was sufficiently flat to be modeled as simply one attenuation value across the entire frequency range analyzed by the receiver simulation. The value used, an attenuation of 7 dB, was the average conversion loss calculated from the typical values in the electrical specifications for the particular mixer modeled, the Marki Microwave T3-04. These specifications are shown in Figure 59. As noted on the datasheet, the conversion loss of the mixer typically degrades at its high (+100 °C) temperature extreme and improves at its low (-55 °C) temperature extreme by less than 0.5 dB, thus a constant loss across temperature could also be reasonably assumed.



**Electrical Specifications** - Specifications guaranteed from -55 to +100°C, measured in a 50Ω system.

Parameter	LO (GHz)	RF (GHz)	IF (GHz)	Min	Typ	Max
Conversion Loss (dB)	.001-4	.001-4	.001-0.5 .001-4.0		6.5 7.5	8.5 10.0

Figure 59: Electrical specifications of Marki Microwave T3-04 mixer, (MX1).

### IF Bandpass Filter FL3

The IF bandpass filter FL3, shown in Figure 53, is a custom-ordered part manufactured by Reactel, Incorporated. The filter’s insertion loss performance was estimated from the graph shown in Figure 60, provided directly through correspondence with the vendor.

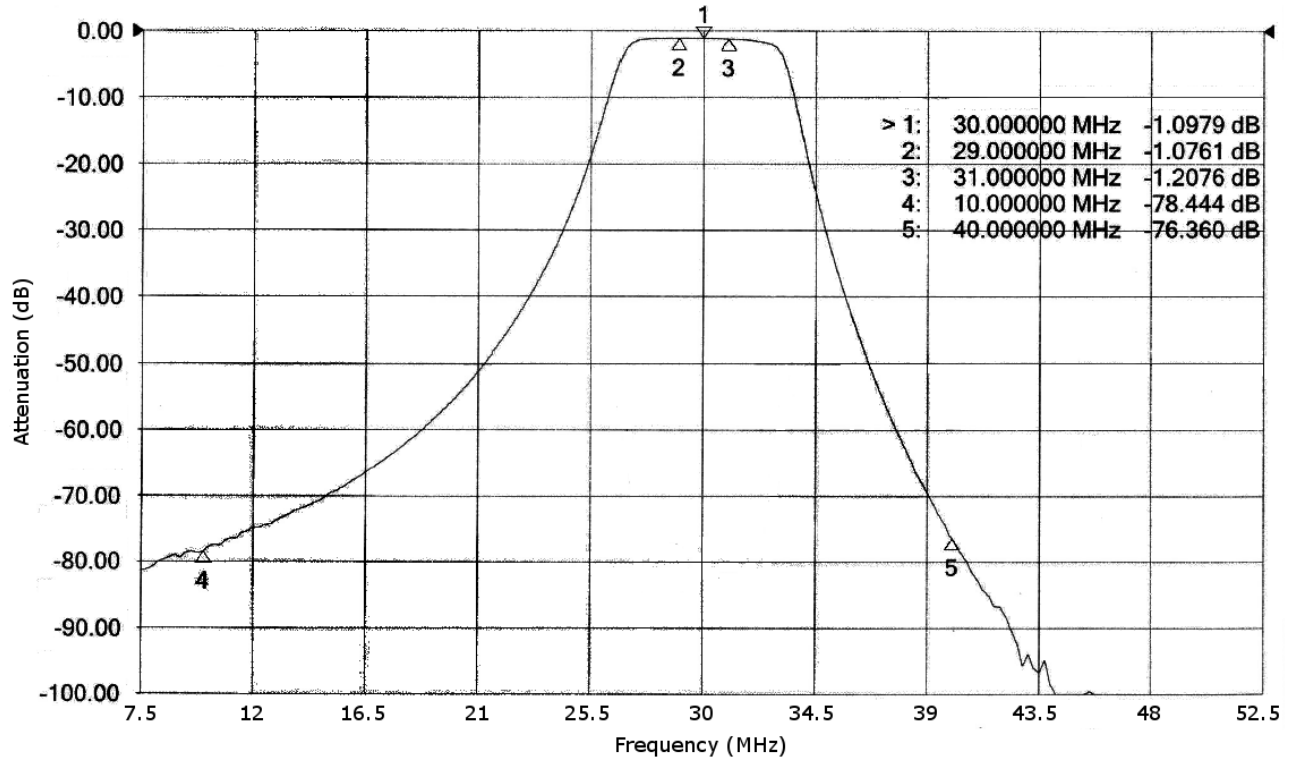


Figure 60: Custom Reactel, Inc. IF bandpass filter (IF BPF FL3) insertion loss (dB) versus frequency (MHz).

Though no numerical data for the filter’s insertion loss with temperature variation were available from the vendor, a representative from Reactel, Inc. informed us that their filters are

considered very stable over the range from -40 °C to +85 °C and further stated that the vendor felt their devices would remain within their specification across this temperature range. Therefore, the values estimated from the graph were assumed constant across temperature in our model.

Table 9: Custom Reactel, Inc. IF bandpass filter (IF BPF FL3) insertion loss values versus frequency, estimated from graph in Figure 60.

Frequency (MHz)	Insertion Loss (dB)	Frequency (MHz)	Insertion Loss (dB)	Frequency (MHz)	Insertion Loss (dB)	Frequency (MHz)	Insertion Loss (dB)
7.5	81.333	21.9	47.222	35.85	40.121	50.25	100
7.95	80.778	22.35	44.778	36.3	46.098	50.7	100
8.4	79.65	22.8	42.222	36.75	50.875	51.15	100
8.85	78.778	23.25	39.35	37.2	54.75	51.6	100
9.3	78.444	23.7	36.333	37.65	58.639	52.05	100
9.75	78.444	24.15	33	38.1	62.347	52.5	100
10	78.444	24.6	29	38.55	66.127		
10.2	77.778	25.05	25	39	69.183		
10.65	77.333	25.5	19	39.45	72.35		
11.1	76.333	25.95	14.889	39.9	75.461		
11.55	75.667	26.4	8.778	40	76.36		
12	74.778	26.85	3.6539	40.35	78.239		
12.45	74.444	27.3	1.5429	40.8	81.239		
12.9	73.778	27.75	1.2089	41.25	84.016		
13.35	73	28.2	1.0979	41.7	86.35		
13.8	72.111	28.65	1.0979	42.15	87.905		
14.25	71.444	29	1.0761	42.6	91.683		
14.7	70.75	29.1	1.0979	43.05	94.016		
15.15	69.5	29.55	1.0979	43.5	96.35		
15.6	68.778	30	1.0979	43.95	98.127		
16.05	67.667	30.45	1.2089	44.4	100		
16.5	66.333	30.9	1.2089	44.85	100		
16.95	65.444	31	1.2076	45.3	100		
17.4	64.222	31.35	1.3209	45.75	100		
17.85	63	31.8	1.4319	46.2	100		
18.3	61.556	32.25	1.5429	46.65	100		
18.75	60.125	32.7	1.8759	47.1	100		
19.2	58.444	33.15	3.2089	47.55	100		
19.65	56.889	33.6	7.6539	48	100		
20.1	55.222	34.05	15.321	48.45	100		
20.55	53.556	34.5	23.987	48.9	100		
21	51.333	34.95	29.674	49.35	100		
21.45	49.4	35.4	35.665	49.8	100		

## IF Amps A4 and A5

The datasheet for the AP108 amplifier provides a graph of device gain versus frequency, shown in Figure 61 on the left, where each curve corresponds to a particular test temperature, -55 °C, +25 °C, or +85 °C. A table of “typical automatic test data”, shown in Figure 61 on the right, complements the graph, reporting vendor-measured gain values at specific frequencies without indication of temperature. Simulation data were thus determined by manually estimating the gain of each curve in the graph at the frequency points listed in the typical automatic test data table. Extra points were estimated from the graph for greater resolution of gain data across frequency at each operating temperature.

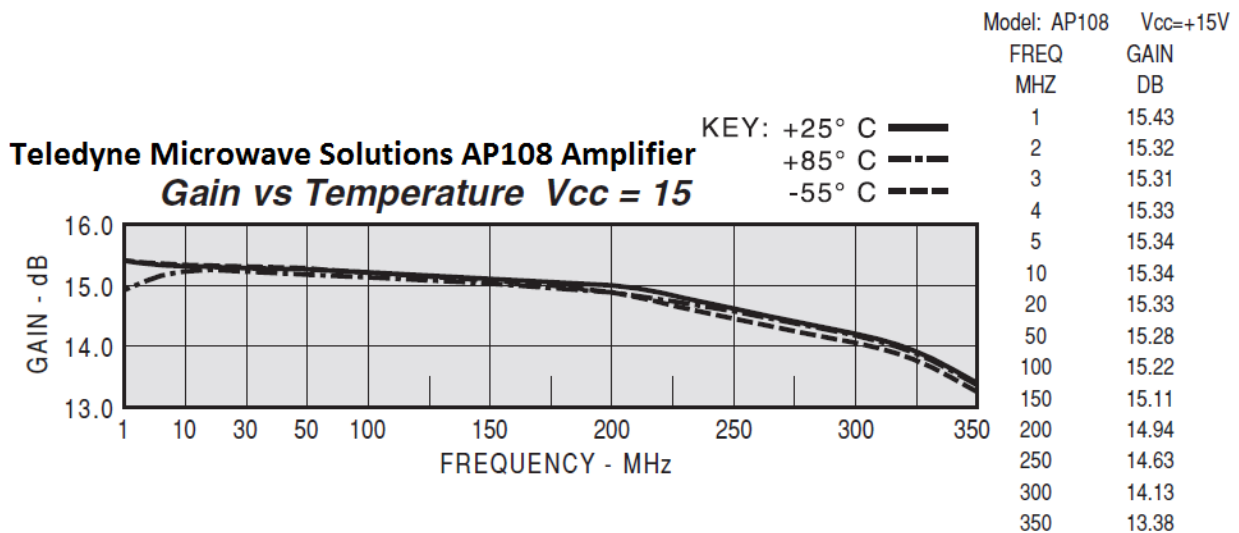


Figure 61: Teledyne Microwave Solutions AP108 amplifier (IF Amps A4 and A5) gain versus frequency curves for three different operating temperatures, -55 °C, +25 °C, and +85 °C (left). Gain remains relatively constant across temperature for any given frequency according to this graph, though after 200 MHz gain appears to decrease as the temperature moves away from +25 °C in either direction. Vendor also provides typical automatic test data table (right).

Table 10: AP108 amplifier (IF AMP A4 and A5) gain values estimated from vendor-provided graph shown in Figure 61 on the left. Gain was estimated for each listed operating temperature at the frequencies specified in the typical automatic test data table, shown in Figure 61 on the right, as well as for additional frequencies selected from the graph for greater resolution.

Frequency (MHz)	Gain (dB)		
	-55 °C	+25 °C	+85 °C
1	15.421	15.421	14.946
2	15.4	15.4	14.996
3	15.391	15.373	15.018
4	15.382	15.364	15.064
5	15.373	15.355	15.109
6	15.355	15.345	15.155
7	15.355	15.336	15.177
8	15.355	15.327	15.2
9	15.345	15.318	15.223
10	15.338	15.318	15.223
12	15.338	15.318	15.236
14	15.338	15.318	15.241
16	15.327	15.309	15.25
18	15.327	15.309	15.264
20	15.327	15.3	15.255
22	15.318	15.3	15.255
24	15.318	15.3	15.245

Frequency (MHz)	Gain (dB)		
	-55 °C	+25 °C	+85 °C
26	15.318	15.295	15.245
28	15.318	15.291	15.236
30	15.309	15.282	15.227
40	15.3	15.273	15.2
50	15.273	15.264	15.173
75	15.245	15.236	15.15
100	15.209	15.209	15.127
125	15.136	15.155	15.073
150	15.064	15.1	15.027
175	14.999	15.036	14.977
200	14.908	15	14.904
225	14.673	14.855	14.755
250	14.454	14.627	14.582
275	14.255	14.415	14.391
300	14.045	14.2	14.182
325	13.782	13.931	13.9
350	13.255	13.408	13.364

### IF Lowpass Filter FL4

The Mini-Circuits SLP-30+, used as the IF lowpass filter FL4, gave the typical performance data shown in Figure 62 on the left, but without any indication of temperature. This lack of temperature information was resolved through a discussion with an applications engineer at Mini-Circuits, who explained that the temperature parameter is omitted from the datasheet of a device whose electrical specifications (shown at the bottom of Figure 62) are consistent across its entire range of operating temperatures. The engineer further expounded that typical performance test data are not guaranteed by the vendor as are the electrical specifications.

Despite this caveat, the typical insertion loss data provided for the SLP-30+ lowpass filter were still assumed across temperature in the simulation since they were within the passband and stopband electrical specifications.

## Typical Performance Data

Frequency (MHz)	Insertion Loss (dB)	
	$\bar{x}$	$\sigma$
1.00	0.07	0.1
10.00	0.21	0.1
19.00	0.29	0.1
28.00	0.37	0.1
31.00	0.48	0.1
32.00	0.55	0.1
33.50	0.62	0.1
34.00	0.76	0.1
35.00	1.30	0.3
38.00	6.09	0.9
40.00	10.78	0.9
43.00	17.56	0.8
45.00	21.65	0.7
46.00	23.56	0.7
47.00	25.39	0.7
48.00	27.19	0.7
50.00	30.58	0.6
55.00	38.32	0.6
59.00	43.69	0.7
60.00	45.01	0.7
61.00	46.27	0.5
91.50	76.88	4.1
109.50	80.77	5.3
127.50	79.89	2.8
145.50	77.20	3.0
164.00	74.52	3.4
173.00	74.92	3.8
182.00	78.05	5.9
191.00	79.62	6.8
200.00	80.65	6.9

## SLP-30+ Low Pass Filter Electrical Specifications

PASSBAND (MHz)	fco (MHz) Nom.	STOPBAND (MHz)	
		(loss > 20 dB)	(loss > 40 dB)
(loss < 1 dB)	(loss 3 dB)		
DC-32	35	47-61	61-200

*Figure 62: Insertion loss for Mini-Circuits SLP-30+ lowpass filter (IF LPF FL4) over frequency sweep (top) and electrical specifications (bottom). Mean insertion loss values only were used for model.*

## Appendix B: Hardware Test Measurements

Table 11: Test measurements of hardware receiver gain for LNA temperatures of 0 °C, +25 °C, and +50 °C with a constant overall hardware temperature of +25 °C. Gain measurements were taken for 11 frequencies at a constant input power of -70 dBm, which is within the receiver's linear region. Due to test environment limitations, receiver gain for a LNA temperature of 0 °C was measured only for one frequency.

Frequency (GHz)	Input Power (dBm)	LNA temperature: 0 °C ± 5 °C		LNA temperature: +25 °C ± 5 °C		LNA temperature: +50 °C ± 5 °C	
		Output Power (dBm)	Gain (dB)	Output Power (dBm)	Gain (dB)	Output Power (dBm)	Gain (dB)
3.005	-70	-	-	-36.7	33.3	-37.15	32.85
3.006	-70	-	-	-26.54	43.46	-27.08	42.92
3.007	-70	-	-	-15.63	54.37	-16.1	53.9
3.008	-70	-	-	-13.73	56.27	-14.22	55.78
3.009	-70	-	-	-13.59	56.41	-14.12	55.88
3.01	-70	-13.22	56.78	-13.57	56.43	-14.13	55.87
3.011	-70	-	-	-14.01	55.99	-14.53	55.47
3.012	-70	-	-	-14.25	55.75	-14.78	55.22
3.013	-70	-	-	-15.7	54.3	-16.23	53.77
3.014	-70	-	-	-30.57	39.43	-31.16	38.84
3.015	-70	-	-	-46.85	23.15	-47.35	22.65



## Appendix C: Calibration Tool Performance Data

Table 12: Comparison of manual calibration and calibration tool results for CW calibration of test receiver set to 0 dB IF attenuation.

Input Power (dBm)	Manual Measurement		Calibration Tool Results		Error (dB)
	Output Power (dBm)	Gain (dB)	Output Power (dBm)	Gain (dB)	
-130	-69.8	60.2	-46.7232	83.2768	-23.0768
-120	-63.1	56.9	-46.6687	73.3313	-16.4313
-110	-53.5	56.5	-46.0915	63.9085	-7.4085
-100	-43.65	56.35	-42.3093	57.6907	-1.3407
-90	-33.69	56.31	-33.6261	56.3739	-0.0639
-80	-23.64	56.36	-23.702	56.298	0.062
-70	-13.69	56.31	-13.8756	56.1244	0.1856
-60	-3.64	56.36	-3.84086	56.15914	0.20086
-50	5.9	55.9	5.85702	55.85702	0.04298
-40	8.62	48.62	Not measurable	N/A	N/A
-30	9.09	39.09	Not measurable	N/A	N/A
-20	9.31	29.31	Not measurable	N/A	N/A
-10	9.31	19.31	Not measurable	N/A	N/A

Table 13: Comparison of manual calibration and calibration tool results for CW calibration of test receiver set to 31 dB IF attenuation.

Input Power (dBm)	Manual Measurement		Calibration Tool Results		Error (dB)
	Output Power (dBm)	Gain (dB)	Output Power (dBm)	Gain (dB)	
-130	-103.1	26.9	-75.8493	54.1507	-27.2507
-120	-94.2	25.8	-75.8404	44.1596	-18.3596
-110	-84.7	25.3	-75.4671	34.5329	-9.2329
-100	-74.61	25.39	-72.6154	27.3846	-1.9946
-90	-64.65	25.35	-64.4595	25.5405	-0.1905
-80	-54.614	25.386	-54.5984	25.4016	-0.0156
-70	-44.788	25.212	-44.7343	25.2657	-0.0537
-60	-34.752	25.248	-34.7343	25.2657	-0.0177
-50	-24.787	25.213	-24.7565	25.2435	-0.0305
-40	-14.752	25.248	-14.7391	25.2609	-0.0129
-30	-5.035	24.965	-5.01648	24.98352	-0.01852
-20	1.957	21.957	2.0166	22.0166	-0.0596
-10	3.35	13.35	3.44432	13.44432	-0.09432

*Table 14: Comparison of continuous and pulsed waveform calibration tool results with test receiver set to 0 dB IF attenuation.*

Input Power (dBm)	CW Calibration Tool Results		Pulsed Calibration Tool Results		Error (dB)
	Output Power (dBm)	Gain (dB)	Output Power (dBm)	Gain (dB)	
-130	-46.7232	83.2768	-46.3258	83.6742	-0.3974
-120	-46.6687	73.3313	-46.4684	73.5316	-0.2003
-110	-46.0915	63.9085	-45.5237	64.4763	-0.5678
-100	-42.3093	57.6907	-42.2866	57.7134	-0.0227
-90	-33.6261	56.3739	-33.6194	56.3806	-0.0067
-80	-23.702	56.298	-23.7041	56.2959	0.0021
-70	-13.8756	56.1244	-13.8775	56.1225	0.0019
-60	-3.84086	56.15914	-3.84092	56.15908	6E-05
-50	5.85702	55.85702	5.86219	55.86219	-0.00517

*Table 15: Comparison of continuous and pulsed waveform calibration tool results with test receiver set to 31 dB IF attenuation.*

Input Power (dBm)	CW Calibration Tool Results		Pulsed Calibration Tool Results		Error (dB)
	Output Power (dBm)	Gain (dB)	Output Power (dBm)	Gain (dB)	
-130	-75.8493	54.1507	-68.9385	61.0615	-6.9108
-120	-75.8404	44.1596	-68.7512	51.2488	-7.0892
-110	-75.4671	34.5329	-68.9294	41.0706	-6.5377
-100	-72.6154	27.3846	-72.2325	27.7675	-0.3829
-90	-64.4595	25.5405	-64.3922	25.6078	-0.0673
-80	-54.5984	25.4016	-54.622	25.378	0.0236
-70	-44.7343	25.2657	-44.7519	25.2481	0.0176
-60	-34.7343	25.2657	-34.7541	25.2459	0.0198
-50	-24.7565	25.2435	-24.7748	25.2252	0.0183
-40	-14.7391	25.2609	-14.7423	25.2577	0.0032
-30	-5.01648	24.98352	-5.0302	24.9698	0.01372
-20	2.0166	22.0166	2.09293	22.09293	-0.07633
-10	3.44432	13.44432	3.58905	13.58905	-0.14473

Table 16: Calibration tool results without a receiver connected; signal generator input connected directly to the ADC.

Input Power (dBm)	Computed Output Power (dBm)	Computed Gain (dB)	Expected Gain (dB)	Error (dB)
-130	-81.0747	48.9253	0	48.9253
-120	-81.073	38.927	0	38.927
-110	-81.0653	28.9347	0	28.9347
-100	-81.0222	18.9778	0	18.9778
-90	-80.6205	9.3795	0	9.3795
-80	-77.5239	2.4761	0	2.4761
-70	-69.766	0.234	0	0.234
-60	-59.8213	0.1787	0	0.1787
-50	-49.8034	0.1966	0	0.1966
-40	-39.8364	0.1636	0	0.1636
-30	-29.9902	0.0098	0	0.0098
-20	-19.9578	0.0422	0	0.0422
-10	-9.97759	0.02241	0	0.02241
0	0.0570714	0.0570714	0	0.0570714

## Appendix D: Time Test

*Table 17: Hardware receiver gain measured across dynamic range immediately after, 30 minutes after, and two hours and 30 minutes after powering on. Measurements taken for a constant signal frequency.*

Input Power (dBm)	Output Power (dBm)		
	Initial	30 Min	2 Hours 30 Min
-130	-61.8413	-62.3197	-62.3647
-120	-61.8251	-62.2646	-62.3045
-110	-61.284	-62.2704	-61.7307
-100	-57.6636	-58.0424	-58.0125
-90	-49.0243	-49.3741	-49.309
-80	-39.1898	-39.5251	-39.4543
-70	-29.4049	-29.7189	-29.6409
-60	-19.3759	-19.6785	-19.601
-50	-9.41978	-9.70275	-9.6295
-40	0.506523	0.334269	0.399636
-30	8.05457	7.93817	7.95045
-20	9.1504	9.08608	9.08811
-10	9.22403	9.18232	9.17636
<b>Calibration Factor</b>	40.5998	40.3177	40.3897

## Appendix E: LO Power Test

Table 18: Hardware receiver gain measured across dynamic range for two different LO powers below minimum LO power required by the mixer.

Input Power (dBm)	Receiver with 21.75 dBm LO Power		Receiver with 0 dBm LO Power	
	Output Power (dBm)	Gain (dB)	Output Power (dBm)	Gain (dB)
-130	-75.8493	54.1507	-76.8344	53.1656
-120	-75.8404	44.1596	-76.7705	43.2295
-110	-75.4671	34.5329	-76.5154	33.4846
-100	-72.6154	27.3846	-74.1355	25.8645
-90	-64.4595	25.5405	-66.4757	23.5243
-80	-54.5984	25.4016	-56.6678	23.3322
-70	-44.7343	25.2657	-46.7959	23.2041
-60	-34.7343	25.2657	-36.8108	23.1892
-50	-24.7565	25.2435	-26.8193	23.1807
-40	-14.7391	25.2609	-16.6733	23.3267
-30	-5.01648	24.9835	-8.69975	21.3003
-20	2.0166	22.0166	-6.85638	13.1436
-10	3.44432	13.4443	-6.82476	3.17524
<b>1 dB Compression Pt</b>	-27.55 dBm		-34.4 dBm	

## Appendix F: MATLAB Implementation Performance

Table 19: Comparison of hardware receiver gain measurements made with a signal analyzer against calculations of gain made by the calibration tool and a MATLAB implementation of bandpass filtering applied to the output signal. Gain values measured or calculated across receiver's dynamic range.

Input Power (dBm)	Output Power (dBm)		
	Signal Analyzer Measurements	Cal Tool Calculations	MATLAB Calculations (Bandpass filter applied)
-150	-85.9	--	-81.1
-145	-84.1	--	-80.55
-140	-81.2	--	-79.05
-135	-79.3	--	-77.59
-130	-73.6	-46.7232	-73.6
-120	-63.1	-46.6687	-63.7
-110	-53.5	-46.0915	-53.72
-100	-43.65	-42.3093	-43.71
-90	-33.69	-33.6261	-33.76
-80	-23.64	-23.702	-23.71
-70	-13.69	-13.8756	-13.88
-60	-3.64	-3.84086	-3.84
-50	5.9	5.85702	5.589
-40	8.62	--	--
-30	9.09	--	--
-20	9.31	--	--
-10	9.31	--	--